Unsnarling Excitation, Relaxation and Scattering Dynamics in Multi-Chiral Distributions of Carbon Nanotubes

by

Jessica Nicole Ames

A dissertation submitted in partial fulfillment
of the requirements for the degree of
Doctor of Philosophy
(Applied Physics)
in the University of Michigan
2017

Doctoral Committee:

Professor Theodore B. Norris, Chair
Professor Çağlıyan Kurdak
Professor Roberto D. Merlin
Associate Professor Jennifer P. Ogilvie
Professor Bradford G. Orr

Believe me, my young friend,

there is nothing - absolutely nothing -

half so much worth doing as

simply messing about in boats.

– Ratty, *The Wind in the Willows*

2017

Dedicated with love to my mom, dad and sister and everyone else in my fantastic, irreplaceable, sometimes unfathomable and absolutely incomparable family. I will always enjoy sharing my very best wine with you, settled on a river's bank, somewhere far off the beaten path.

Thanks for the many adventures.

ACKNOWLEDGMENTS

Many moons ago I traveled with family to Chile to run a river named the Bio-Bio. Cut into the Andes on the flank of Volcán Callaqui the river had attained a measure of international renown for its challenging rapids as well as its stunning beauty. It had also been condemned, through the approval of a World Bank loan, to disappear behind Pangue damn and never be seen again. We had to go. If you are a kayaker you know this.

Getting to put-in (the launch point on any river excursion) is often a challenge for a remote river and this was no exception. As memory serves the trip was a six, or even eight, hour drive over dirt roads through beautiful, sparsely populated Andean foothills. This particular route had a special feature — an eight-mile long tunnel used by a mining operation a century earlier. The tunnel was no longer in commercial use, or any use really, and had not been maintained for decades. Signs of its rapidly approaching demise were everywhere. Water streamed out of fissures in the tunnel arch. Large rocks and boulders that had fallen from the ceiling were littered all over the narrow path. I don't think our minibus ever cracked five miles per hour as it swerved and dodged boulders and unrelenting potholes. Not far in we lost site of the light from the entrance. Ahead, between the rapid swipes of the windshield wipers that could not keep up, we saw nothing...

For those of us who actually read this dissertation (no judgement) we have Heather Ferguson and Libby Maret to thank for thoughtfully reviewing my work. This document is certainly better for it and I am very grateful for all of their insights.

During my extended adventure here at the University of Michigan I have been extremely privileged to work with not one, not two, but three research groups. I am indebted to Professor Jennifer Ogilvie and her research group for taking me in before I had even

begun my graduate toil and for allowing me to remain a quasi-member of the family to the very end. Likewise, Professor Roberto Merlin and his group were extremely generous in providing me not only with valuable lab space and time, but more importantly, with the opportunity to work with colleagues whose expertise and friendship I will always value greatly. Who wouldn't bond over hours of realigning an OPA or cleaning up from one flood after another? And, of course, Professor Theodore Norris and his research group — the one group I actually belonged to officially. How does anyone get through grad school with just one group?

Despite the fact that Ted declined my repeated suggestions that we put a Jacuzzi in the lab I consider myself lucky to have had the chance to work with him. Throughout this slog he has been unwaveringly supportive and encouraging. As my research results have repeatedly defied any simple explanation he has guided me through the process of finding deeper insights into the data. Whether he intended to or not he showed me that, while the underlying physics was always amazing, the challenge of understanding it was the real adventure. The Jacuzzi would have helped, though.

I would also like to thank two groups of collaborators without whom this dissertation would be little more than a title. Celia Cunningham and Jeramy Zimmerman of the Forrest group here at Michigan generously provided all of the polymer/nanotube films studied and also measured the photoluminescence properties of the blends. And Matthias Florian of the Jahnke group at the University of Bremen generated and managed the code used to model coherent interaction with the samples. It should also be noted that Celia's research and mine were primarily sponsored by the Center for Solar & Thermal Energy Conversion (CSTEC).

Of all my co-conspirators a few need special mention. I owe many, many thanks to Chuck Divin for his willingness to help and to share his knowledge in the lab. I have tried ever since to repay his generosity by helping others in the lab as he helped us all. I'll be lucky if I've been even half as helpful. Chuck set the bar very high. Andrea Bianchini

meanwhile was there to walk that awkward path with me of setting up an experiment in a lab just as all of the folks with the institutional knowledge graduated or moved on. We figured it out, mostly. And despite knowing that my coffee would never be safe in his presence it was always a great pleasure to work with him. Andrea has likely inspired all of us to be true to our hearts. I'm certain that he will continue to inspire me. Then there is Prashant Padmanabhan whom I appreciate more than anything else just for being Prashant. The world is a different place with him in it and that is a great thing. I also owe Libby Maret my heartfelt thanks for cleverly pulling me away from the computer and back outside where I belong. Yes, of course we ended up talking about physics all the time anyway, but anyone who doubts the significance of a little kayaking should reread the quote above from Ratty.

Of course I blame Diana for helping graduate school seduce me back into the classroom and laboratory. Never mind that I was already on that slippery slope, our decision to come to Michigan for medical school sealed my fate. Good on you Doc. And to the rest of my family, last but not least, I will always be indebted to you just for being there, and maybe occasionally wondering out loud 'why on earth are you doing this?' Thank goodness every one of you has been a part of my family. I love you all.

TABLE OF CONTENTS

LIST OF FIGURES

LIST OF TABLES

LIST OF APPENDICES

LIST OF ABBREVIATIONS

CNT carbon nanotube

CoMoCAT cobalt-molybdenum catalyst

DA differential absorption

DFT density functional theory

DOS density of states

DT differential transmission

EEA exciton-exciton annihilation

FWHM full width at half maximum

HiPCO high pressure carbon monoxide

MDMO-PPV poly[2-methoxy-5-(3′,7′-dimethyloctyloxy)-1,4-phenylene vinylene]

MEH-PPV poly[2-methoxy-5-(2′-ethyl-hexyloxy)-1,4-phenylene vinylene]

OPA optical parametric amplifier

P3HT poly(3-hexylthiophene)

P3OT poly(3-octylthiophene)

PA photo-induced absorption

PFH poly[9,9-dihexylfluorenyl-2,7-diyl]

PFO poly(9,9′-dioctylfluorene)

PLE photoluminescence excitation

PVP poly(vinylpyrrolidone)

RBM radial breathing mode

SDS sodium dodecyl sulfate

TPA two-photon absorption

ABSTRACT

This research begins the process of studying a polymer/carbon nanotube prototype solar cell. Inclusion of nanotubes in a photoactive polymer simultaneously overcomes the limited diffusion length of charge carriers and vastly extends the spectral sensitivity. Further improvements in these hybrid designs will now require a comprehensive understanding of the diverse contributions from, and limitations of, each component of these new solar cells. Research described in this dissertation focuses on the light harvesting component, a heterogenous distribution of individual carbon nanotubes in a photoactive polymer, with the goal of quantifying the contributions from each of the individual nanotubes to the harvested photocurrent.

Absorption of light by photoactive polymers and nanotubes generates strongly bound excitons. To transform these short lived excitons into a harvestable photocurrent they must be efficiently dissociated and transported through the device, with minimal losses, before coupling to external leads. Designing an efficient solar cell then is aided by understanding every step in the evolution of charge carriers from excitation to harvested photocurrent. This research focuses on simultaneously measuring the excited states of a carbon nanotube distribution in comparison with the literature.

The heterogenous distribution of carbon nanotubes provides a series of parallel detectors collectively contributing extended spectral sensitivity to the cell. Selectively observing carrier evolution from each nanotube species is accomplished through non-degenerate pump-probe measurements. The broadband measurements in spectrally congested neighborhoods of nanotubes limits selectivity needed to follow a single species. The challenge of simultaneously measuring the response of multiple nanotube species is addressed in two

ways. First, a set of rate equations is assumed representing our current understanding of nanotube dynamics as a discrete set of energy levels for each relevant nanotube species. These dynamical equations are fit to multiple data sets for a range of excitation intensities. Second, additional relaxation measurements are taken for an atypical strong probe. The strong probe provides access to the dependence of nanotube dynamics on their excited state transitions. With this additional information the contributions from various nanotubes can be distinguished and quantified. Across all data sets we found, within 20% error, lowest energy bright exciton lifetimes of ~175fs, exciton-exciton annihilation rates of ~0.19ps^{-1} and that 80% of second excited state excitons decayed non-radiatively into the first bright exciton. Fitting results, however, showed wide, unexpected variation in one bright state lifetime and the coupling between one of the second excitons to the first. This hot probe technique has, therefore, uncovered additional physics not fully described by a discrete-level rate equation model.

Variations in rate equation solutions are partly attributed to coherent interaction of both pump and probe fields with the nanotubes. To test the coherence hypothesis an alternative density matrix approach is proposed that accounts for strong pump and probe as well as decay and dephasing. Results of this model are highly sensitive to both pump and probe intensities and can only generally reproduce the expected population behavior and differential absorption signatures seen in the data. The coherent model, however, predicts non-linear pump-probe interaction just beyond the measured power ranges providing for testable verification in the future.

Both models therefore lead to the conclusion that the existing discrete-level models for carbon nanotube dynamics are incomplete, and a full microscopic theory of optical interaction will be required.

CHAPTER 1

Carbon Nanotubes, Light Harvesting and What Happens Next

Over the past twenty years or so carbon nanotubes (CNTs) have been the focus of a tremendous amount of attention. Researchers have seen the potential in nanotubes from their mechanical properties [1] to their use in medicine [2] and for advances in nearly every component of nano- and opto-electronics [3, 4]. At roughly a nanometer in diameter but without restriction on their length, carbon nanotubes are also quasi- one-dimensional. As model quantum wires they have motivated the study of 1D quantum mechanical effects in a real material [5, 6], moving well beyond the theoretical framework of idealized thought experiments (and homework problems).

In 1991 Sumio Iijima was the first to observe the generation of "helical microtubules," now known as CNTs, in a laboratory[7]. Curiously, even though single sheets of graphite (graphene) were not isolated in a laboratory until 2004 [8], much of the basic band theory of CNTs derives from a tight binding approximation for graphene developed by Wallace back in 1947 [9]. And, while considerable research has been carried out on CNTs since, it took another decade after learning to manufacture them before techniques were developed to sufficiently isolate individual nanotubes [10] allowing for measurements of their specific, unperturbed optical properties to proceed. This was a significant step for research into the dynamics of CNTs since theoretical investigation of the narrow confinement of charge carriers in nanotubes led to an expectation that excited states should be excitonic [11, 12].

Now measurable, these excitonic states have been found to dominate the optical properties of carbon nanotubes.

In terms of electronics, CNTs are prized for their high carrier mobility [13] and nanoscale, critical properties for advances in electronic circuitry [6, 14]. They are also tunable [15] and, as we'll see below, they are direct bandgap materials making them ideal for many opto-electronics applications. In fact Avouris, et al. pointed out that one can build "a CNT device that can operate either as a transistor, a light emitter or a light detector simply by changing the applied voltage" [15].

It is within this context that Arnold, et al., developed a polymer based prototype photodetector that takes advantage of the high mobility and spectral response of a broad distribution of carbon nanotubes [16]. The authors determined that blending nanotubes into a photoconductive polymer could overcome spectral bandwidth limitations seen in earlier attempts at organic photodetectors. They also took advantage of the strong optical response of CNTs to improve on the weak photoresponses encountered when blending inorganic nanocrystals into the polymers. The result was a hybrid organic/inorganic photodetector with a broad spectral responsivity extending from 400 nm out to 1450 nm, with much of that range attributed to the incorporation of carbon nanotubes.

A schematic of the prototype photodetector can be seen in Figure 1.1 including several design variations studied in their paper along with a graph of the broad spectral responsivity. Illumination generates excitons in both the polymer and carbon nanotubes. The short diffusion length of excitons in photoactive polymers is overcome by dispersing the nanotubes throughout the matrix where they can act as electron acceptors and charge carrying adducts to transport dissociated electrons. Excitons generated in the CNTs travel to heterojunctions of C60 or simultaneous heterojunctions of C60|SnPc where they efficiently dissociate contributing to the overall photocurrent. Arnold found that these devices could result in a peak internal efficiency of 44% but ultimately translated to a peak external efficiency of only 2.3%. One of the more significant roadblocks to higher efficiency is due to

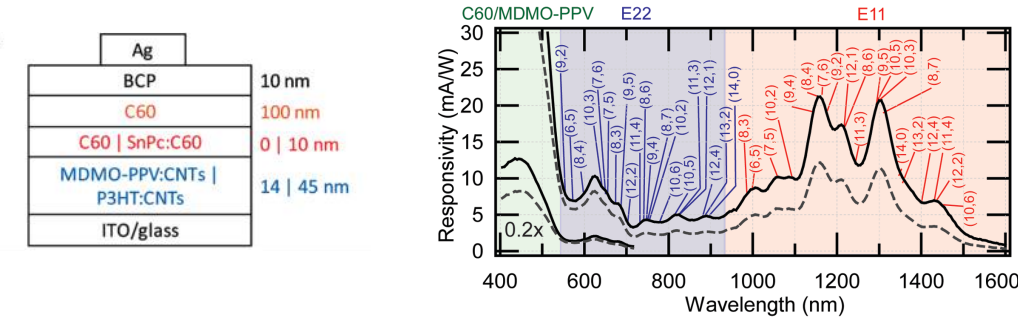

Figure 1.1: Hybrid organic/inorganic photodetector. Design schematics from Arnold, et al., [16]. (Left, from Figure 1) Carbon nanotubes were dispersed in photoactive polymers MDMO-PPV or P3HT and capped with C60 or a blend of C60 and SnPc. Vertical lines indicate design variations studied by the authors. (Right, from Figure 2) The spectral responsivity of the carbon nanotubes dispersed in MDMO-PPV. Contributions from many of the individual chiralities (n,m) are indicated.

the CNTs themselves. Despite vastly extending the spectral range of the detector most of the absorbed light is lost to short lived excitons undergoing non-radiative relaxation.

Harvesting the energy absorbed by the polymer and nanotubes requires a multistep process in which tightly bound excitons must undergo diffusion and dissociation involving multiple layers and heterojunctions. Parasitic effects including trap and dark states, limited diffusion, mismatched heterojunctions that block rather than facilitate dissociation, exciton quenching metallic nanotubes and more all lead to recombination that can seriously limit the energy harvesting efficiency of a device. Ultimately we would like to avoid each and every one of these pitfalls but to do so requires understanding the paths that excitons and free carriers follow throughout the device.

We can learn a lot about a photosensitive prototype by varying design parameters, biases and exposure to different light sources. But we can get a comprehensive view of the rapid carrier evolution from excitation to photocurrent by incorporating the device directly into an ultrafast pump-probe experiment using it as both the sample and detector. In doing so our measurements would be sensitive to each and every component contributing to the final photocurrent. Where a traditional pump-probe measurement in transmission depends

on every optically active element in a sample, the device as detector scheme would ignore any aspect of the device that does not contribute to the photocurrent. In addition to quantifying efficiencies for various structural changes, measuring the differential photocurrent would allow us to selectively evaluate the contributions and femtosecond dynamics of each nanotube species.

The overall goal of this research is to use ultrafast pump-probe measurements on a prototype solar cell design based on the photodetector described above. Samples designed and fabricated by the Forrest group here at the University of Michigan (contributors to the original photodetector studies with Arnold) would be incorporated as their own detectors as just described. Ultimately we would like to investigate device designs that incorporate all of the above: The contributions from the carbon nanotubes; the contribution from the photoactive host polymer; and the incorporation of CNT's as efficient molecular wires within the polymer matrix. Before introducing the solar cell prototype as the detector the first step is to systematically investigate the excited state electronics of polymer/nanotube films. This dissertation is, therefore, focused on measuring the relaxation dynamics in these films and relating the dynamics back to the literature on individual carbon nanotubes.

1.1 Dissertation Outline

In the following chapter I will introduce carbon nanotubes as a material that can be conceptually derived from graphene. I'll describe how the basic bandstructure and density of states of nanotubes can be distilled from the dispersion relation of graphene. Nanotubes and graphene are different, however, and I will show how confinement to a nanometer scale diameter tube modifies the bandstructure significantly. A more detailed bandstructure will also emerge from the spin and valley degeneracy nanotubes inherit from graphene within the context of a carbon nanotube. In addition the strong Coulomb interactions that result from this confinement will motivate the necessity of treating the energy levels of a CNT

as a many body problem and conclude that excitons dominate the excited states and corresponding optical properties of these nanotubes.

In terms of the strongly bound excitonic states the full bandstructure can be thought of as a discrete ladder of energy levels. Given this picture of the nanotube energy levels I will describe our current understanding of the excited state dynamics of a CNT from excitation through relaxation back to the ground state.

Chapter 3 describes the blended CNT/polymer films studied in my research. Several processes have been developed to create the nanotubes we use, each resulting in a different chiral distribution. Similarly the separation and dispersing methods that have been investigated can have a significant impact on the resulting nanotube distribution, their purity and the quality of the CNTs. Often nanotubes are dispersed and studied in a surfactant solution, but for the purposes of light harvesting it is far more interesting and relevant to consider CNTs dispersed in a photoactive polymer as in the prototype device described by Arnold. I will show that blending nanotubes in a polymer not only enhances the absorption and extends the overall range it also vastly improves the mobility of the polymer's charge carriers, an additional motivating factor. Once the nanotubes have been dispersed in a surfactant or polymer it helps to know what we've ended up with and several optical methods are described for characterizing these blends. These combined observations should give the reader a general understanding of the steps needed to prepare and characterize the nanotube films studied here.

In Chapter 4 I will describe the ultrafast pump-probe methods used in this research. The underlying idea of using ultrashort pulse trains to both excite and probe the resulting changes in a material will be illustrated. The probe in particular will be seen to measure changes in the electronic states of the material by interacting directly with the electronic system. Dynamical changes in the excited states will translate into variations in the absorption of the probe which can be described as a differential transmission (DT) spectrum.

Measurements of this sort will, however, rely on pulse widths on the order of 100 fs

resulting in high energy densities that can induce non-linear responses in both the polymer and CNTs. This high optical fluence can even alter the materials themselves. As a result some effort will be made to identify the ranges within which linear and non-linear behavior is be expected as well as attempts that were made to reduce the sample susceptibility to photo-damage.

The pump-probe measurements will also depend critically on characterization of the specific polymer/nanotube films investigated. Ground state transitions will be determined from linear absorption measurements and validated by comparison to a photoluminescence excitation (PLE) map. Corresponding excited state transitions will be estimated from theoretical approximations. With this framework femtosecond pump-probe measurements will then be described that can follow the evolution of these excited states.

In Chapter 5 I will finally introduce a series of non-degenerate pump-probe experiments on a heterogenous blend of CNTs in a polymer with some unusual relaxation behavior. Despite the complexity of a heterogenous blend of nanotubes I would like to be able to quantify the dynamics in multiple nanotube species. To achieve this a rate equation model will be introduced that describes the excited states of carbon nanotubes as discrete excitonic states. For accuracy and completeness, and in order to make things even more difficult, the model also assumes a non-linear Auger-like exciton-exciton annihilation (EEA) process contributes to the relaxation. The multi-chiral nature of the broadband solar cell design adds yet another challenge, with overlapping resonances limiting the ability to selectively measure specific nanotube species. To overcome this an atypical strong probe will be included in the measurements providing a more detailed picture of the excited state relaxation paths the CNTs follow. We will find that modeling the ultrafast relaxation of multiple nanotubes in this way is mostly successful but gives an incomplete picture of all the dynamics involved.

An alternative interpretation of the excited state dynamics as a coherent interaction between the nanotubes and pump and probe fields will also be considered. For a system

with sufficiently long dephasing times the interaction with the driving fields may be better understood as a coherent response. Evidence for this is seen in both the excited populations and the effective pulse areas relative to the nanotube Rabi frequencies. A density matrix approach describing the carbon nanotubes in the coherent regime will be proposed and computational results will be compared to the ultrafast relaxation data. Results from this modeling will give us some additional insight into the unexpected relaxation behavior seen in my data.

CHAPTER 2

Optical & Electronic Properties of Carbon Nanotubes

The carbon nanotubes that provided the extended optical range to the polymer based photodetector are members of an increasingly diverse collection of nanoscale materials: Semiconducting quantum dots, gold and silver nanorods, boron-nitride nanotubes, and single layer molybdenum disulfide sheets make up just a few of these emerging materials. These materials are fascinating in their own right, but their size, unique electronic properties and susceptibility to the local environment also make them highly tunable. As a result they are often candidate components for newly designed metamaterials and devices [6]. They have also received attention as natural models for testing quantum mechanics at low dimensions [17] and for their ability to exhibit quantum behavior [18] on a macroscopic scale where classical behavior would be expected. Carbon nanotubes in particular are intriguing both as optically active and quasi- one-dimensional materials.

For my research, and for the photodetector described above, we are interested in the tightly bound excitons that form in carbon nanotubes (CNTs) when optically excited. These optical excitations have resonant energies that can be selected according to their chiralities and tuned through changes in the surrounding dielectric environment. From an applications point of view the energy from these excitons may then be harvested as a photocurrent — if the excitons can be efficiently dissociated before they recombine. In addition, the nanotubes are very promising simply as passive components of organic solar cells due to their

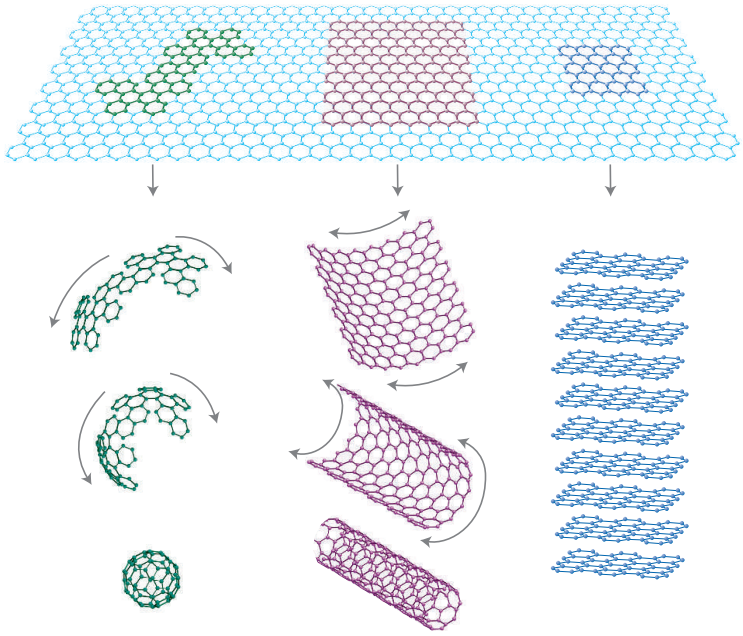

Figure 2.1: From graphene to carbon nanotubes. Figure 1 from Geim & Novoselov's 2007 review of research on graphene [23]. The figure demonstrates how graphene can be thought of as the building block (building sheet, really) for buckyballs, carbon nanotubes, nanoribbons and even graphite.

exceptional conductivity [19], mechanical strength [20, 21], and chemical stability [22].

2.1 Carbon Nanotubes Derived from Graphene

One of the advantages of studying carbon nanotubes is the degree to which they can be accurately and more-or-less accessibly modeled from first principles. Much of this advantage comes from the fact that single-walled carbon nanotubes can be thought of as rolled up graphene sheets. And the bandstructure of graphene itself, one that CNTs inherit, can be approximated analytically with only minimal simplifications.

Graphene can be thought of as the fundamental unit of graphite since the latter is composed of many graphene sheets stacked one upon another. By itself graphene is a single-atom-thick sheet of hexagonally arranged carbon atoms. Figure 2.1 from A. K. Geim and K. S. Novoselov shows a piece of one of these sheets and the way in which nanotubes and buckyballs can be thought of conceptually as products of graphene [23]. In practice

buckyballs, nanotubes and graphene are all generated through different chemical and material processes rather than deriving everything from graphene (although some research, going in the other direction, has shown that one can generate graphene quantum dots from buckyballs [24] and carbon fibers [25]). Geim, while famous for magnetically levitating a frog [26], also managed to gain some notoriety with Novoselov when they successfully parlayed an adept use of wrapping tape and a little science into isolating and characterizing these single sheets of graphene from their multi-sheet graphite parent [8].[1]

The nanotube that appears as if cut from the graphene in Figure 2.1 is only one of many, many possible configurations that can be derived from this ideal monolayer. To quantify all of these configurations we have to take careful note of how the tube might be cut from the graphene sheet. This more general description is demonstrated in Figure 2.2 where the allowable tube configurations can be defined in terms of regions with self-consistent boundaries. In the diagram the vector $\vec{C}_h$ represents the end or circumference of an uncapped nanotube meeting this boundary condition. Defining $\vec{C}_h$ as the vector sum of the graphene basis vectors $\vec{a}_1$ and $\vec{a}_2$ we get

$$\vec{C}_h = n \cdot \vec{a}_1 + m \cdot \vec{a}_2 \tag{2.1}$$

As we will see this simple roll-up definition for $\vec{C}_h$ dominates the electronic properties of CNTs to the extent that we refer to each of these tubes in terms of their chiral indices (n,m). The transverse vector $\vec{T}$ (i.e., perpendicular to the chiral vector) corresponds to the direction of the tube axis. The length of $\vec{T}$ is often chosen so that the area defined by $\vec{C}_h$ and $\vec{T}$, given by $\left|\vec{C}_h \times \vec{T}\right|$, represents the CNT unit cell [27]. Note, however, that real tube lengths can easily be thousands of times longer than $\vec{T}$. An important related index that crops up on occasion is the number of hexagons per unit cell. Since we can describe the elementary cell for graphene as $|\vec{a}_1 \times \vec{a}_2|$ the hexagons per unit cell can be written as

[1] In 2010 Geim and Novoselov were awarded the Nobel prize in physics for their work on graphene and ended up traveling to Stockholm because of it. I have no idea if the frog got to travel to Boston when he won the Ig Nobel prize in 2000.

$$N = \frac{\left|\vec{C}_h \times \vec{T}\right|}{|\vec{a}_1 \times \vec{a}_2|} = \frac{2\left(n^2 + nm + m^2\right)}{R} \tag{2.2}$$

where R is defined as the least common denominator of $2n + m$ and $2m + n$ [28].

Figure 2.2 shows the chiral vector $\vec{C}_h$ for (5, 1) nanotubes and its corresponding transverse vector projected over an ideal graphene sheet. The dashed, light gray lines represent two special cases: zigzag nanotubes with chiral indices (n, 0) and armchair nanotubes with indices (n,n). Any chiral vector representing the translation from one hexagon to another along or between these chiral vectors will correspond to a unique set of chiral indices (n,m). Beyond the limiting cases of the zigzag or armchair roll-up vectors the pattern simply repeats itself resulting in a six-fold rotational symmetry within the graphene plane while the inverted pattern also spans the plane through reflection.

Graphene Bandstructure

Given the description above of carbon nanotubes as an extension of graphene my earlier statement that we can describe the band structure of nanotubes from the graphene band structure may come as little surprise. In fact a rich qualitative understanding of the electronic properties of nanotubes can be inferred almost directly from graphene's calculated band structure as soon as we impose the self-consistency constraint of the chiral vector (Eq. 2.1).

Graphene itself consists of a single atom thick sheet of carbon atoms each bound to three coplanar atoms through its three hybrid $2sp^2$ orbitals. It is these three strong, coplanar σ-bonds that dictate the hexagonal lattice structure of graphene. Ignoring the two $1s$ electrons which do not contribute to the relevant electronic structure, each atom has one remaining $2p$ electron which results in unsaturated π orbitals perpendicular to the graphene plane. In graphene as well as its fullerene derivatives these electrons form a delocalized π network through π-π bonding that extends along the material surface and gives rise to its

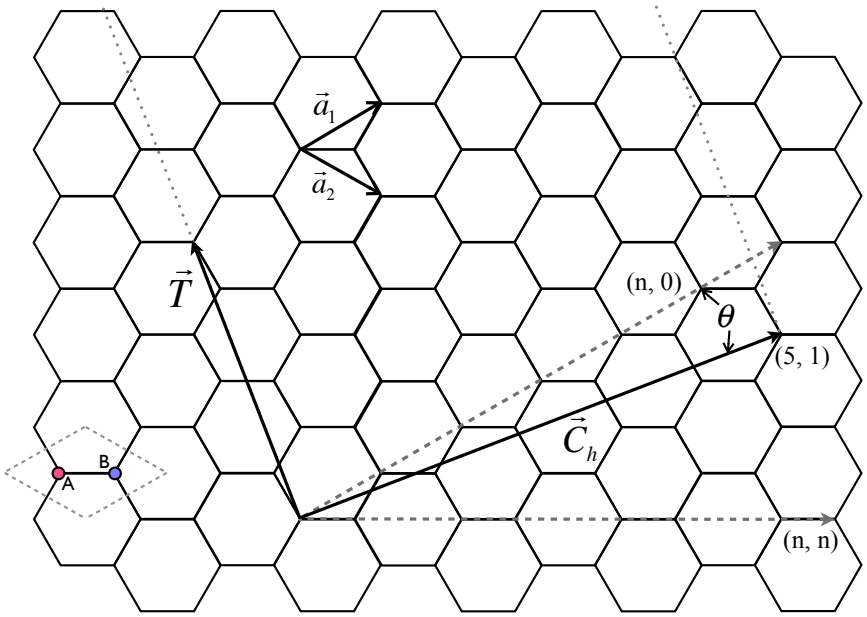

Figure 2.2: Carbon nanotubes "cut" from a graphene sheet. The chiral vector $\vec{C}_h$ (solid black) is shown for $(5, 1)$ nanotubes. Roll-up vectors (dashed dark gray) for zigzag, $(n, 0)$, and armchair, (n,n), nanotubes are the limiting cases. The transverse (axial) vector $\vec{T}$ is shown with arbitrary length. The nanotube cutout would correspond to the light gray dotted lines. The chiral angle $0 \leq \theta \leq 30^\circ$ is measured from the zigzag orientation. Graphene basis vectors $\vec{a}_1$ and $\vec{a}_2$ are shown for reference while the diamond containing *A* and *B* represents a typical choice for the primitive cell of graphene with its two atom basis. Figure inspired by Odom, et al. [27].

electronic properties.

In calculating the dispersion relation for graphene the crystal-like periodicity can be defined in terms of a two atom unit cell with the basis vectors $\vec{a}_1$ and $\vec{a}_2$ (See Fig. 2.2). The calculations can then be simplified by assuming a Bloch expansion of the wave functions for each sub-lattice corresponding to the two atoms in the unit cell and, without loss of generality, that the z direction is perpendicular to the graphene sheet so that these unbound orbitals can be realistically approximated as $2p_z$ Hydrogen wavefunctions. The calculation is also greatly simplified by the use of a tight binding approximation in which only the three nearest neighbors interact with the central atom. With these approximations a single particle eigenvalue equation $H_o\Psi = \varepsilon\Psi$ with the free-carrier hamiltonian H_o and eigenfunctions Ψ can be analytically solved for the dispersion equation ε.

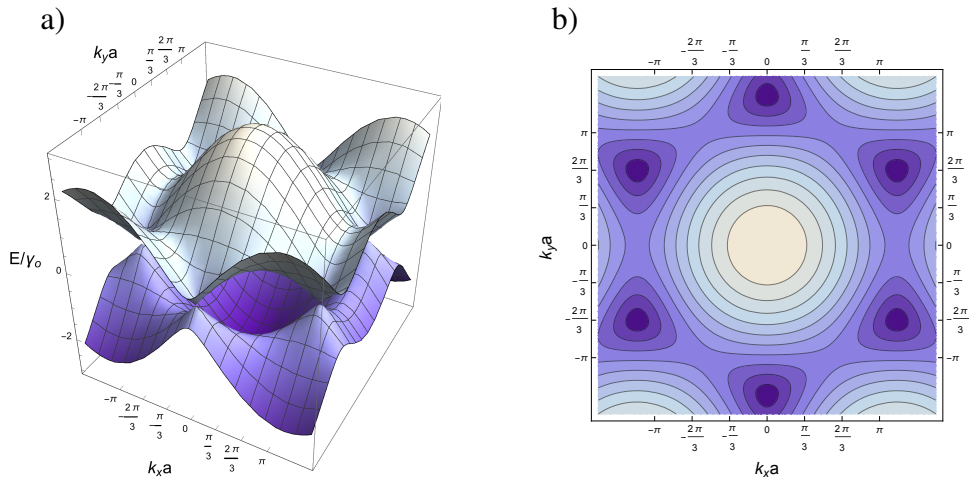

Figure 2.3: Graphene band structure. a) π (valance) and π* (conduction) bands joining at the zero bandgap Dirac points *K* and *K′*. Some of the symmetry between the upper and lower branches of this graph is lost when higher order corrections are included. b) Contour plot of one branch with the Γ point at the center while the *K*, *K′* points are alternately at the center of the darkest regions. Diagrams inspired by a) Castro Neto, et al., [32] and b) Odom, et al., [27].

The explicit quantum mechanical derivation of graphene's single particle dispersion relation, first carried out by Wallace in 1947 [9], can be found in many papers and texts [6, 29, 30, 31] and will just be assumed here. The result for both bands $E(k) = \left|\varepsilon_k^{\pm}\right|$ can be expanded as

$$E/\gamma = \pm\sqrt{1 + 4cos\left(\frac{3}{2}k_y a\right)cos\left(\frac{\sqrt{3}}{2}k_x a\right) + 4cos^2\left(\frac{\sqrt{3}}{2}k_x a\right)} \tag{2.3}$$

where $\gamma \approx -2.7\,\text{eV}$ is the carbon-carbon interaction energy [6], the variable $a = \sqrt{3}a_{C-C} = \|\vec{a}_i\|$ is the length of the lattice vector and a_{C-C} is the nearest neighbor separation variably given as $a_{C-C} = 1.44\text{Å}$ [31] or $a_{C-C} = 1.42\text{Å}$ [6, 32]. A number of refinements can be made to this result including a correction to $\gamma = -2.97\,\text{eV}$ [33] to account for the curvature of the tube [31] and the inclusion of next nearest-neighbor terms [32] but the general form of the dispersion remains the same for the purpose of our discussion.

Figure 2.3 shows a three dimensional graph and contour representation of the graphene band structure. The six high symmetry points where the valance and conduction bands

meet are referred to successively as K and K'. The regions immediately surrounding these points have a conical shape giving a linear dispersion analogous to massless relativistic particles. As a result the electrons and holes can be modeled in quantum mechanics using the massless Dirac equation [32]. With this analogy K and K' are often referred to as Dirac points and the region surrounding them as a Dirac cone.

Carbon Nanotube Bandstructure

While anyone studying graphene would understandably concentrate on the Dirac cones and the zero bandgap at the K, K' points, these corners of the hexagonal Brillouin zone may and may not play a role in the electronic structure of a given carbon nanotube. The full 2D Brillouin zone of graphene is not really accessible to CNTs since the conceptual roll-up of graphene imposes an additional chirality dependent confinement in the circumferential orientation of the nanotubes. This limits its band structure to a series of 1D slices through the 2D band structure. Mathematically this just means that we apply the cyclic constraint [30] of the circumferential vector $\vec{C}_h$ on the wavefunction so that $\Psi\left(\vec{r}+\vec{C}_h\right) = \Psi\left(\vec{r}\right)$, i.e., $\Psi\left(\vec{r}+\vec{C}_h\right) = \Psi\left(\vec{r}\right) e^{i\vec{k}\cdot\vec{C}_h}$ which imposes the quantization

$$\vec{k}\cdot\vec{C}_h = 2\pi j \text{ where } j \in \left\{\left[N/2-1, N/2\right] | N/2 \in \mathbb{Z}\right\}. \tag{2.4}$$

The only unconstrained degree of freedom left is in the axial direction. The axial component of the wave vector, $\vec{k}_T$ (perpendicular to the circumferential component), becomes the defining free parameter in the dispersion relation for a given cut j. Applying the quantization condition and the dependence of $\vec{k}_T$ on $\vec{k}$ and $\vec{C}_h = (C_x, C_y)$ to Equation 2.3 leads to the 1D dispersion relation [6]

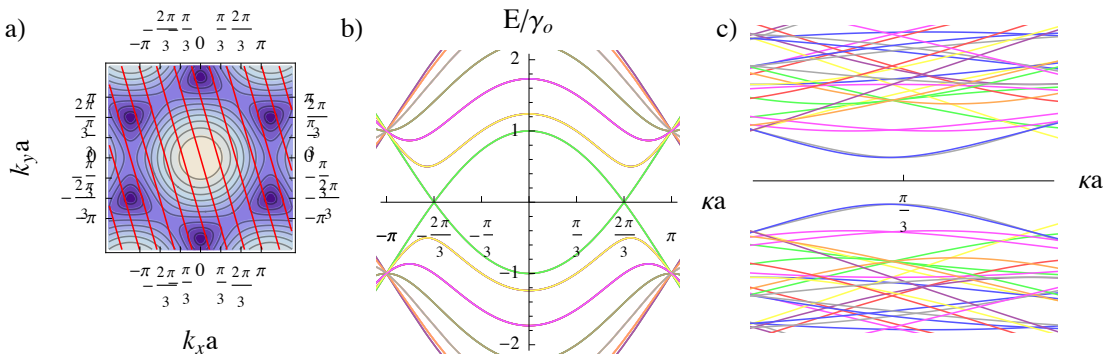

Figure 2.4: CNT bandstructures. a) Red cutting lines represent the quantization constraint $\vec{k} \cdot \vec{C}_h = 2\pi j$ for $(6, 2)$ CNTs relative to the underlying 2D dispersion of graphene. These tubes are semiconducting. Adapted from Odom, et al., [27]. b) First few bands for $(6, 6)$ tubes showing the zero bandgap at the Dirac points. These tubes are metallic. c) Zone-folding version of the bandstructure for the $(6, 2)$ tubes shown in (a). Only a few of the 52 bands are shown. The gap between upper and lower bands results in semiconducting nanotubes. Note that the semiconducting tubes have direct band gaps.

$$E/\gamma = \pm\sqrt{1 + 4cos\left(\frac{2\pi j C_y a - \mathbf{C} C_x \kappa a}{2\mathbf{C}^2}\right) cos\left(\frac{2\pi j\sqrt{3} C_x a + \sqrt{3}\mathbf{C} C_y \kappa a}{2\mathbf{C}^2}\right) \cdots + 4cos^2\left(\frac{2\pi j C_y a - \mathbf{C} C_x \kappa a}{2\mathbf{C}^2}\right)} \quad (2.5)$$

where $\mathbf{C} = \left\|\vec{C}_h\right\|$ is the measure of the nanotube circumference and $\kappa = \left\|\vec{k}_T\right\|$ is the projected length of the wave vector in the axial direction.[2] Some of the resulting 1D band structures of carbon nanotubes can be seen in Figure 2.4. The graphs demonstrate the contrast between the case where one of the slices passes through a Dirac point representing a conducting nanotube and the case where none of the slices pass through the Dirac point resulting in a semiconducting nanotube.

Figure 2.4 (a) demonstrates the relationship between the 2D graphene bandstructure and the 1D slices (red lines) corresponding to the quantization condition of Equation 2.4

[2] $\vec{k}_T$ is also often denoted $\vec{k}_\parallel$ or $\vec{k}_z$, particularly when emphasizing that light is polarized parallel to the nanotube axis.

for $(6, 2)$ nanotubes. Close inspection reveals that none of the slices pass through a K or K' point (darkest points). When the cutting lines are graphed together as in Figure 2.4 (c) we can see that they represent the energy bands of the $(6, 2)$ nanotubes. Since the valence and conduction bands never cross nanotubes of this chirality are semiconducting. In contrast the cutting lines for $(6, 6)$ tubes (Fig. 2.4 (b)) do pass through Dirac points resulting in CNTs with a metallic band structure. For semiconducting nanotubes the minima for the lowest energy bands will correspond to the points at which the bands are closest to one of the Dirac points. The two smallest bandgaps (which will correspond to the first two excited states of the nanotubes) are found on the two slices nearest to and on either side of a neighboring Dirac point. For more detail see Appendix B.

Metallic and semiconducting carbon nanotubes Despite the many possible chiralities that a carbon nanotube can have, a number of generalizations can be made that categorize nanotubes into various families. The most important may be the distinction between metallic and semiconducting nanotubes which we've seen can be distinguished by whether or not a band intersects a Dirac point. To see the origin of this mathematically consider Figure 2.4 again where one of these Dirac points is $K = \frac{2\pi}{3a}(1, 1/\sqrt{3})$. Assigning $\vec{k}$ to this Dirac point in Equation 2.4 and expanding $\vec{C}_h$ according to Equation 2.1 the constraint equation reduces to $3j = 2n + m$. In other words, whenever $2n + m$ is a multiple of 3 the nanotube will be metallic. More generally, the constraint equation can be thought of as cyclic with $(2n + m)\texttt{mod}3 = p,\ p = \{0, 1, 2\}$, breaking the result into three categories with $p = 0$ denoting metallic tubes and the other two semiconducting. In the general literature the reader will also encounter (See Appendix A) the equivalent cyclic relation $(n - m)\texttt{mod}3 = q,\ q = \{0, 1, -1\}$ where $(p)\texttt{mod}3 = -q$. This is not a strictly defined criterion in that large curvature affects (in tubes with diameters smaller than a nanometer) can result in σ-π hybridization inducing bandgaps of a few tens of meV in metallic nanotubes [6, 34] or conversely changing what would be a semiconducting nanotube into

a metallic nanotube [35]. For typical laboratory generated nanotubes of ~1 nm, however, the distinction between semiconducting and metallic tubes is a generally accepted guideline. There are several other family categorizations that can be made but they have limited relevance to this discussion (See Appendix A).

Numerically we can see that $1/3$ of the nanotubes should be metallic and in practice this is roughly true in the initial manufacturing step [36]. In Chapter 3 I'll mention some of the reasons that the distribution of both metallic and semiconducting tubes may vary and why we might (and might not) worry about their presence. For the most part, however, my research considers only semiconducting tubes.

2.2 1D Density Of States: van Hove Singularities

In Figure 2.4 (c) we can see the signature of a semiconducting nanotube where the π and π* bands are separated creating a characteristic band gap much like any bulk semiconductor. Unlike a bulk semiconductor, however, the dimensions of a CNT suggest that the density of states (DOS) for a nanotube should be more consistent with an ideal 1D material. This is directly supported by strong confinement of the charge carriers leading to distinct energy bands. Figure 2.4 (c) also suggests that it is reasonable to approximate the bandstructure as parabolic, i.e. $\varepsilon_k^\lambda = a^\lambda k^2 + \varepsilon_0^\lambda$, where a is just a parameter and $\lambda = v$ or c for the valence and conduction bands respectively. Calculating a DOS for a semiconducting nanotube then gives [30]

$$D(\varepsilon) = \frac{8}{2\pi}\sum_\lambda \int dk' \frac{1}{\left|2a^\lambda\left(k' - k_0^\lambda\right)\right|}\delta\left(k^\lambda - k'\right) = \begin{cases} \sum_\lambda \frac{2}{\pi\sqrt{a^\lambda}}\frac{1}{\sqrt{\varepsilon^\lambda - \varepsilon_0^\lambda}} & \varepsilon^\lambda > \varepsilon_0^\lambda \\ 0 & \text{otherwise} \end{cases} \tag{2.6}$$

Notice that at the band minima, as $\varepsilon^\lambda \to \varepsilon_0^\lambda$, the density of states is unbounded forming van Hove singularities in the DOS of this quasi-1D system.

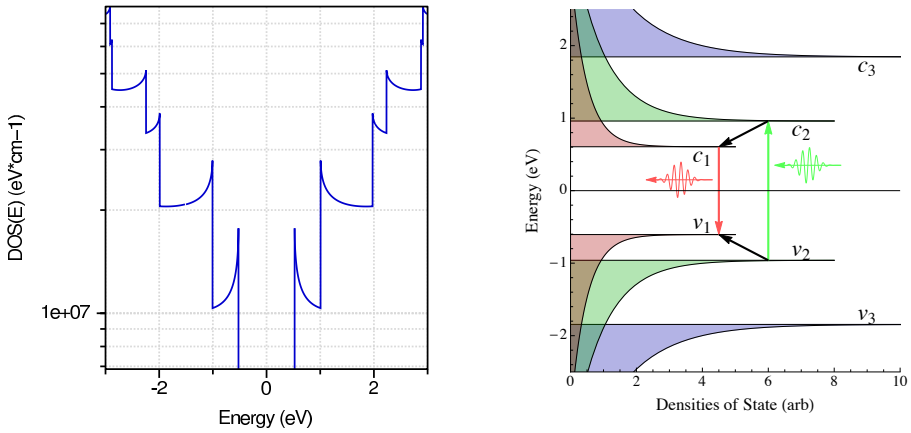

Figure 2.5: Density of states for $(7, 5)$ carbon nanotubes. Left) Calculated DOS vs Energy showing van Hove singularities [38, 39]. Since these are semiconducting tubes the DOS vanishes around the Fermi level. Right) Illustration of simplified excitation/relaxation process in semiconducting nanotubes with dipole allowed transitions assuming van Hove singularities. Transition energies are from an empirical fitting by Weisman, et al. [40].

Assuming a 1D system is not only consistent with the geometry but also the narrow resonances seen in absorption and emission measurements [10]. Experimental verification of such 1D densities of state in which the characteristic van Hove singularities can be clearly seen has been made using differential conductance measurements [37]. Figure 2.5 shows the calculated multilevel 1D density of states for $(7, 5)$ semiconducting nanotubes. An illustration of the underlying DOS for the first few energy states of $(7, 5)$ tubes exhibits the presumed excitation and relaxation steps that followed from early absorption and photoluminescence excitation (PLE) measurements (see Chapter 3).

2.3 Optical signatures of Carbon Nanotubes

If we think of CNTs as typical semiconductors then we can make some reasonable estimates of the optical bandgaps from the bandstructure demonstrated in Figure 2.4 (c) or, equivalently, the band edge transitions suggested in Figure 2.5. These $v_i \rightarrow c_i$ transitions between the corresponding *i*th valence and conduction bands are referred to as E_{ii} transi-

tions.[3] And, in fact, the values that have been calculated in this way agree reasonably well with the optically measured values [40]. Again, the analogy with bulk semiconductors is misleading. Excitation in a typical bulk semiconductor would lead to free charge carriers or excitons with binding energies of only a few meV [41]. Experimentally, however, CNT transitions appear as strong, narrow resonance peaks indicative of the strongly bound excitons that theory predicts [11] for tightly confined charges. In addition, a breakdown of this simple free carrier model was seen when the first two excited state transition energies were compared. That is, if the free-carrier description were adequate then the ratio of second to first excited state energies E_{22}/E_{11} would converge to 2 for large diameters [31]. What is seen instead is a bit more interesting (see Appendix B) with the ratio converging instead to a value between ~1.7 according to O'Connell, et al. [10] and ~1.85 as seen by Bachilo, et al. [42]. The origin of this error comes from the over simplified assumption that excited states are generated as uncorrelated electron-hole pairs with simple excitation energies equal to the band-to-band separations — the idea suggested above and in Figure 2.5. In materials with nanoscale spacial confinement, however, many body effects can have a significant impact on the electronic properties in question and carbon nanotubes are representative in this respect.

Confirmation that the unbound/weakly bound electron-hole model was, in fact, not the best description of CNTs in an excited state was finally seen in 2005 in several experiments concluding that the excited electron-hole pair states in carbon nanotubes must be tightly bound excitons with binding energies of ~ 400 meV [43, 44, 45]. This large binding energy, $>> k_BT$ at room temperature, has led to a general understanding of the energy profile of carbon nanotube as an exciton manifold in which excited states are considered in analogy to an atomic model. Further studies lent additional support to the dominant exciton manifold picture in finding no signature of free electrons and holes [46, 47, 48].

[3] On occasion they are denoted as S_{ii} or M_{ii} to distinguish between transitions in semiconducting or metallic nanotubes respectively. They may also be denoted as E_{ii}^{S} or E_{ii}^{M} respectively. Some authors have even adopted the notation S_i or M_i to be more consistent with the excitonic nature of these states and move away from the independent electron picture that motivates the double indices.

Since the excited states are separated by energies of ~1 eV [35] it is more realistic to think of these nanotubes as having only one degree of freedom (the axial direction). For this reason nanotubes are often referred to as quasi-one dimensional materials.

The Exciton Picture — Many Body Refinement

The entire description above, from the graphene band structure to the van Hove singularities of the 1D DOS and the expected $v_i \rightarrow c_i$ excitations is based on the single-particle Hamiltonian that describes graphene. It has been incredibly successful in qualitatively describing the transition energies of carbon nanotubes [42], especially when extended to include additional neighbors [33] and nanotube curvature effects [34]. And from these transition energies we can generally infer the optical excitations and excited state relaxation that takes place after excitation. In the pronounced confinement of a quasi-1D carbon nanotube, however, this model doesn't adequately account for the many-body effects leading to correlated electron-hole pair excitations and ignores the tightly bound nature of these excitons in such an environment. In order to move beyond a qualitative understanding and realistically model the electronic properties of CNTs a many-body formalism that accounts for strong Coulomb interactions is necessary.

The general form of a Hamiltonian that takes into account the contributions of all interacting particles, assuming no external field and ignoring spin, can be written [49, 50]

$$H_{mb} = \sum_j \frac{\mathbf{P}_j^2}{2M_j} + \sum_i \frac{\mathbf{p}_i^2}{2m} + \sum_{i,j} \frac{-Z_j e^2}{|\mathbf{R}_j - \mathbf{r}_i|} + \sum_{j<j'} \frac{Z_j Z_{j'} e^2}{|\mathbf{R}_j - \mathbf{R}_{j'}|} + \sum_{i<i'} \frac{e^2}{|\mathbf{r}_i - \mathbf{r}_{i'}|} \tag{2.7}$$

where for a simple bulk crystal $\mathbf{R} = n_1\mathbf{a}_1 + n_2\mathbf{a}_2 + n_3\mathbf{a}_3$ represents the lattice positions of the Bravais lattice and the $\mathbf{r}_i$ are the electron positions. The first term in the Hamiltonian represents the kinetic energy of the nuclei. On the assumption that the ions are fixed this term vanishes. The second and third terms combined represent the single electron Hamilto-

nian for each (i^{th}) electron where the Z_j factors represent the combined effect of the nuclei and all but the valence electron. The fourth term defines the potential energy of the interacting ions (combined nuclei and subvalence electrons). This term together with the third term can be thought of as the generalized potential. The last term represents the interaction term between all the valence electrons in the many-body system. Solving for the eigenvalues and eigenfunctions of this many-body Hamiltonian is generally considered too complicated or yielding solutions that are untenable [50]. A major simplification of this problem, the Hartree-Fock approximation, results in an antisymmetrized wave function built from one-electron solutions with all the remaining electrons averaged into a single field. With the H-F approximation iterative improvements of the averaged electron field can be found but the problem remains prohibitively complex [51].

Density Functional Theory Treatment

The general approach to refining and extending this model in order to take into account the strong confinement and interaction of charge carriers in nanotubes is to retreat to an *ab initio* computational model. These models have to take into account the fundamental electronic structure of the carbon nanotubes, the many possible transitions and the dominant Coulomb interactions of the tightly confined charge carriers. This approach is theoretical and computational in nature and outside the focus of my research. To give some idea of the underlying calculations a very brief outline of this approach is distilled here from Spataru, et al. [35], with additional references when relevant.

In practice many-body problems are not realistically solvable without substantial simplifications. Mean-field theories like the Hartree-Fock approximations can lead to approximate solutions but only after a complex iterative process. Recent attempts at *ab initio* modeling of the electronic properties of CNTs have instead begun with a density functional theory (DFT) approach to determine their ground state properties [52, 53, 54, 55]. In this approach, following the treatment and notation of Louie, et al., [50] the electronic

ground state energy E_V is defined as a functional of the charge density $\rho(\boldsymbol{r})$

$$E_V[\rho] = \int V(\boldsymbol{r})\,\rho(\boldsymbol{r})\,d\boldsymbol{r} + T_s[\rho] + \frac{1}{2}\int \frac{\rho(\boldsymbol{r})\,\rho(\boldsymbol{r}')}{|\boldsymbol{r}-\boldsymbol{r}'|} d\boldsymbol{r}d\boldsymbol{r}' + E_{xc}[\rho] \tag{2.8}$$

for an external static potential $V(\boldsymbol{r})$. The kinetic energy of the non-interacting electron system is represented by T_s and an unknown exchange-correlation energy functional by E_{xc}. The advantage of this approach is that it can lead, in principle, to an exact determination of the total energy and charge distribution of a given nanotube. The calculations minimize the energy functional through the charge density determined by a set of one-electron Kohn-Sham equations of the form

$$\left[-\frac{\hbar^2\nabla^2}{2m} + V_{ion}(\boldsymbol{r}) + V_H(\boldsymbol{r}) + V_{xc}(\boldsymbol{r})\right]\phi_j(\boldsymbol{r}) = \epsilon_j\phi_j(\boldsymbol{r}) \tag{2.9}$$

where V_H is the repulsive electrostatic field (Hartree field) due to the electron charge distribution while the exchange-correlation potential, V_{xc}, accounts for the quantum electron-electron interactions. Solutions to these eigenvalue equations lead to the charge density $\rho(\boldsymbol{r}) = \sum |\varphi_i(\boldsymbol{r})|^2$ needed to minimize the energy functional. These solutions rely, however, on the description of the exchange-correlation potential as the variation of E_{xc} with respect to the electron charge density, $V_{xc} = {}^{\delta E_{xc}}/_{\delta\rho(\boldsymbol{r})}$. According to Louie the most common description of E_{xc} takes the form [50]

$$E_{xc} = \int \rho(\boldsymbol{r})\,\varepsilon_{xc}(\boldsymbol{r})\,d\boldsymbol{r} \tag{2.10}$$

with the local exchange correlation energy density $\varepsilon_{xc}(\boldsymbol{r})$. Since E_{xc} is unknown this equation describes it in terms of an approximation of $\varepsilon_{xc}(\boldsymbol{r})$. According to Louie both the local density approximation (LDA) and generalized gradient approximation (GGA) have been successful in describing E_{xc} [50]. These calculations are further simplified by assuming pseudo-potentials combining the tightly bound core electrons with the binding potential of the nuclei.

Since DFT calculations by themselves can only determine the electronic ground state for a single particle this method is not able to model the dynamics of nanotube excited states. In order to model optical excitations — at least two particles — perturbations are applied first in the form of a one-particle Green's function providing the band energies and wavefunctions for the addition or removal of an electron or hole. In practice this perturbation calculation may be carried out using the "GW" approximation ("G" for Green's function, "W" for Coulomb interaction) to account for screening in the self energy. In functional form this means solving for the quasiparticle (electron or hole band) energies ϵ_j and wavefunctions $\psi_j(\mathbf{r})$ in the Dyson equation,

$$\left[-\frac{\hbar^2\nabla^2}{2m} + V_{ion}(\boldsymbol{r}) + V_H(\boldsymbol{r})\right]\psi_j(\boldsymbol{r}) + \int d\boldsymbol{r}' \sum{}_{XC}\left(\boldsymbol{r}, \boldsymbol{r}', \epsilon_j\right)\psi_j\left(\boldsymbol{r}'\right) = \epsilon_j\psi_j(\boldsymbol{r}) \quad (2.11)$$

Here $\sum_{XC}(\mathbf{r}, \mathbf{r}', \epsilon_j)$ represents the self-energy so that the integral accounts for the exchange-correlation potential an excited quasiparticle sees from the surrounding environment.

Since solving the Dyson equation only gets us the energies and amplitudes for adding or removing uncorrelated quasi-particles an additional step is required to account for a two-particle state. A second perturbation is needed in the form of a two-particle Green's function giving us the quantum amplitude χ_S and energy Ω_S for each exciton. The amplitude is given by the Tamm-Dancoff approximation

$$\chi_S\left(\boldsymbol{r}_e, \boldsymbol{r}_h\right) = \left\langle 0 \left| \hat{\Psi}\left(\boldsymbol{r}_e\right), \hat{\Psi}^\dagger\left(\boldsymbol{r}_h\right) \right| S \right\rangle = \sum_{cv} A^S_{cv}\psi_c(\boldsymbol{r}_e)\psi_v(\boldsymbol{r}_h)^* \quad (2.12)$$

where the ψ were found from the Dyson equation above and the $\hat{\Psi}^\dagger$ and $\hat{\Psi}$ are creation and annihilation operators. The coefficients A^S_{cv} account for the correlation and entanglement of the electron and hole comprising the exciton. They can be found along with the formation energies Ω_S from the Bethe-Salpeter equation

$$(\epsilon_c - \epsilon_v) A^S_{cv} + \sum_{c'v'} K(\Omega_S)_{cv,c'v'} A^S_{c'v'} = \Omega_S A^S_{cv} \tag{2.13}$$

The $K(\Omega_S)$ terms represent the interaction between the electron and hole by incorporating the long-range screened Coulomb interaction and the short-range repulsive exchange interaction.

These approximations and models underlie the application of time-dependent density functional theory calculations to the fundamental electronic structure of carbon nanotubes. The calculations have been seen to be sensitive to the choice of model Hamiltonians, degree of long-range Hartree-Fock exchange and basis sets [53] reflecting the intrinsic sensitivity of nanomaterials to the energy profiles, many-body interactions and underlying geometry at the nanometer scale.

Observations from DFT Calculations

Calculations employing either model conclude that the optical properties of CNTs are dominated by tightly bound excitons [56, 35] as expected. In addition they explain why the transition energies of these excitons are remarkably similar to what the excitation energies would be in the single-particle case. Figure 2.6 (a) demonstrates the difference in the absorption properties for three different computational scenarios. The lowest energy absorption line represents the case for single, non-interacting quasi-particles and reproduces the asymmetry of the van Hove singularities of the density-of-states. The highest energy absorption line represents the case where the self-energy of electron repulsion is included due to the tight confinement within nearly-1D nanotubes. Inclusion of the previously neglected self-energy renormalizes the band gap. The result is a >1 eV blue shift in the excitation energy. For the third absorption band we can see that inclusion of the electron-hole Coulomb attraction significantly reduces the excitation energy. Weak screening in the one-dimensional geometry of nanotubes means that the binding energy of an exciton can

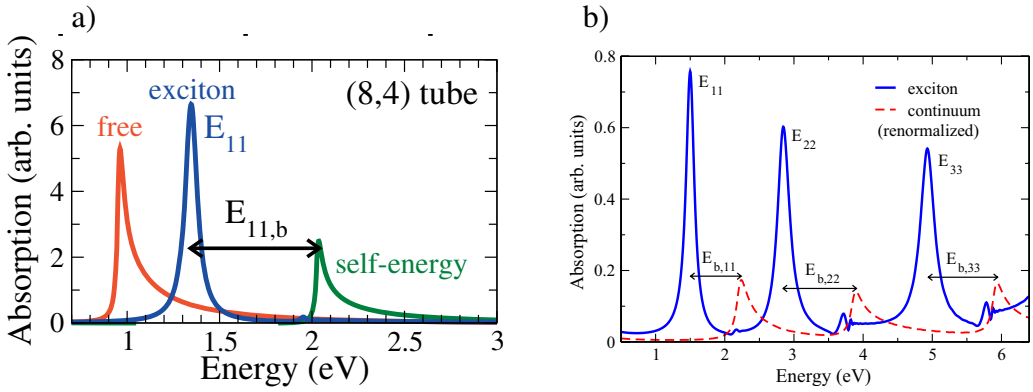

Figure 2.6: Many-body effects and absorption. a) Inset to Figure 1 from Malic, et al. [56]. Absorption spectra for $(8,4)$ nanotubes versus Coulomb interaction. Free-particle case (red) is the lowest energy transition and exhibits a van Hove singularity line-shape. Bandgap renormalization (green) due to electron-electron repulsion causes the absorption to blueshift >1 eV. Including Coulomb attraction (blue) between electron-hole pairs redshifts the absorption by the exciton binding energy and transforms the lineshape from van Hove singularity to Lorentzian. b) Figure 1 from Malic, et al., [57]. Renormalized and excitonic absorption spectra for first three excitons. Evidence of excited state excitons seen in the small peaks near the band edges of the continuum energies.

be a large percentage of the transition energy. In addition to the large binding energy an indication of exciton formation can be seen in the transformation of the line-shape into a symmetric Lorentzian [30].

The continuum state, which we now know to be 300–500 meV above the bound exciton state, does not cease to exist. However, with the emergence of strongly bound excitons due to nanoscale confinement Malic, et al., found that the excitons capture most of the oscillator strength — ~ 6 times that of the renormalized continuum [30]. PLE maps discussed in both Chapters 3 and 4, which should be sensitive to absorption by the continuum states, do not even indicate their presence which is likely drowning out in the noise floor.

Influence of the Local Environment

The large, roughly 1 eV, binding energy suggested in Figure 2.6 (a) is twice what is reported in the literature [44, 45]. This is not surprising since the calculations assumed only a vacuum for the surrounding environment. In the real world, however, the surrounding

environment has a significant effect on transition energies, binding energies and more [58].

The influence of the local environment is partly a result of screening due to the local dielectric. Coulomb induced screening due to this dielectric environment modifies the optical absorption spectrum through both the renormalization and the electron-hole interaction. In contrast to the significantly reduced screening provided by the one-dimensional nanotubes themselves the dielectric of the surrounding medium significantly influences the exciton binding energies, electron-hole correlation lengths, optical transition energies as well as relaxation dynamics of CNTs [57]. There is evidence, as well, that modulation of the dielectric screening of a polymer surrounding CNTs will modulate the exciton resonances of the nanotubes [59].

In the ab initio models sensitivity to the local dielectric environment is accomplished by introducing a momentum-dependent screened Coulomb interaction. In terms of the transfer of momentum $\mathbf{q} = |\mathbf{k} - \mathbf{k}'|$ the screened Coulomb interaction becomes $W(\mathbf{q}) = V(\mathbf{q}) / \varepsilon_{bkg} \varepsilon(\mathbf{q})$ where $V(\mathbf{q})$ is the traditional Coulomb interaction, ε_{bkg} represents the dielectric background constant and $\varepsilon(\mathbf{q})$ introduces the momentum-dependent dielectric function. Calculations incorporating this modified Coulomb potential found reductions in the binding energies to values consistent with those observed in the literature [30].

The computational analyses with the screened Coulomb interaction also validate a more direct expression for the influence of the effective dielectric environment on the binding energies of CNTs. Using a variational method Perebeinos, et. al., found that the lowest exciton binding energies follow the effective dielectric as $E_b \propto \varepsilon^{-\beta}$ where comparison to measured values determined that $\beta \approx 1.4$ [60]. More recent work by Malic, et al., found $\beta \approx 1.3$ [57]. Here the effective dielectric represents not only the polymer matrix but also the conformational relationship it has with the nanotubes.

2.4 The Exciton Manifold

Everything discussed to this point has assumed that each E_{ii} transition represents a unique, non-degenerate state. Forgive me if I have misled you, but this is physics and it's never that simple. Not only do the excitons themselves have excited states but the presence of strongly interacting charged particles with spin as well as the degeneracy in the K valleys of the graphene Brillouin zone lead to a number of subbands worth considering.

Hydrogenic Exciton States

Each excitonic state, E_{ii}, represents the lowest energy exciton corresponding to the free particle $v_i \rightarrow c_i$ transition. And each of these excitons can be thought of as the ground state of an hydrogenic system with its own set of excited states. As a result, each E_{ii} exciton has a series of excited states analogous to the Rydberg ladder of states leading to ionization which, in this context, is the free carrier or continuum state [30]. The ground and excited state excitons are denoted E_{ii}^{1u}, E_{ii}^{2g}, E_{ii}^{2u}, E_{ii}^{3g}, E_{ii}^{3u}, ... where u ("ungerade") denotes a state with odd symmetry and g ("gerade") denotes a state with even symmetry [61, 44]. The study by Wang, et al., often credited with demonstrating that optical excitations of CNTs are excitons, exploited the existence of these higher energy states to determine exciton binding energies [45]. In their work they used single photon excitation to access the odd E_{11}^{1u} ground state and two-photon excitation for the E_{11}^{2g} state. In calculations by Malic, et al., only the first excited state of the E_{11} exciton could be distinguished from the continuum [30]. It can be seen emerging near the band edges of the continuum states in Figure 2.6 (b).

Spin

The strong electron-electron and electron-hole Coulomb interactions that drive the band renormalization and exciton formation discussed above also act to couple the electron and hole spins of these excitons [62]. The exciton wavefunctions must therefore account for

these coupled spins. Four possible symmetric and antisymmetric configurations are possible:

$$|\psi_s\rangle = \frac{1}{\sqrt{2}}\left(|\uparrow\downarrow\rangle - |\downarrow\uparrow\rangle\right) \text{ and } |\psi_t\rangle = |\uparrow\uparrow\rangle\,,\ \frac{1}{\sqrt{2}}\left(|\uparrow\downarrow\rangle + |\downarrow\uparrow\rangle\right),\ |\downarrow\downarrow\rangle \tag{2.14}$$

where ψ_s is the spin singlet (antisymmetric with respect to spin exchange with total spin S = 0) and ψ_t represents the three possible spin triplet states (symmetric with total spin S = 1). The even parity triplet states are optically dark since their generation would require the creation of spin. In fact they are sufficiently independent of the singlet state due to weak spin-orbit coupling, [63, 64, 65], that they can be completely neglected from consideration when describing the excited states of a CNT.[4] Measurements, for example, by Seferyan, et al., noted that the 3 ps transfer time they observed from the bright exciton to a lower energy state was much too fast to represent transfer to a triplet state given the weak coupling [67].

Valley Degeneracy — Singlet State Splitting

Each spin state also represents multiple sublevels owing to the time reversal symmetry of the graphene reciprocal lattice [32]. As a result of this symmetry the energy eigenvalues are degenerate (see Eq. 2.3) for the two valleys nearest the inequivalent K and K' (Dirac) points. For chiral nanotubes this leads to a two-fold degeneracy in both the valence and conduction bands depicted in Figure 2.4 (c). Electron-hole pair excitations formed from these transitions therefore carry a four-fold degeneracy. The zone folding representa-

[4] Spin-orbit coupling has been found in a few nanotubes to induce splitting as high as 3.4 meV and attributed this to the curvature of the nanotube [66]. The authors note that this is an order of magnitude larger than previously seen, however, and its origin "... is not explained by existing theories." Since this coupling is typically an order of magnitude smaller than 3.4 meV and assumes the smallest diameter nanotubes, and since all of the experiments I will discuss were carried out at room temperature (where $k_B T \sim 25$ meV) any linewidth broadening due to such coupling is expected to be well below the resolution of my measurements and the other results discussed.

tion, however, hides the fact that the single-particle momenta of these bands are different owing to their proximity to the inequivalent K and K' points in the underlying graphene bandstructure. In the left-hand graph of Figure 2.7 the degenerate valleys are shown separated by their crystal momenta (aka the "quasi-angular" momenta of the CNTs [68]). The electron-hole pair transitions in this scenario can then be identified with these valleys as $|K, K\rangle$, $|K', K'\rangle$, $|K, K'\rangle$, and $|K', K\rangle$.

The four-fold degeneracy is lifted slightly by the Coulombic interaction between the electron and hole [15, 53], though one study attributes this to the weak spin-orbit coupling instead [69]. The tightly bound excitons that are generated by these transitions are then comprised of a doublet of opposite valley states, $|K, K'\rangle$, and $|K', K\rangle$, as well as two coupled bonding, $\frac{1}{\sqrt{2}}(|K, K\rangle + |K', K'\rangle)$, and anti-bonding, $\frac{1}{\sqrt{2}}(|K, K\rangle - |K', K'\rangle)$, states [62]. The right-hand graph of Figure 2.7 roughly approximates the resulting exciton dispersion for each of these states. Three of these states are optically forbidden. The two cross-valley states carry non-zero quasi-angular momenta ($k = \pm 2k_o$). As a result these states cannot be generated by optical excitation without an additional phonon contribution. The anti-bonding case, which is antisymmetric, leads to an overall even symmetry for the singlet state that cannot couple to light. The spin singlet bonding state, however, has overall odd symmetry and is therefore the only state that is accessible to a dipole transition. Not surprisingly this optically allowed singlet state is referred to as the bright state and is the assumed state whenever "E_{ii}" is written.

Bright vs Dark Excitons

The three remaining dipole forbidden states cannot be ignored as in the case of the triplet states. Instead, they play an important role in the relaxation process of optically excited nanotubes described below. Mixing of the singlet states follows from the many tube variations including defects, distribution of lengths and interactions with the environment [70]. The combined effect can result in both weakly active states and dark states with vanishing

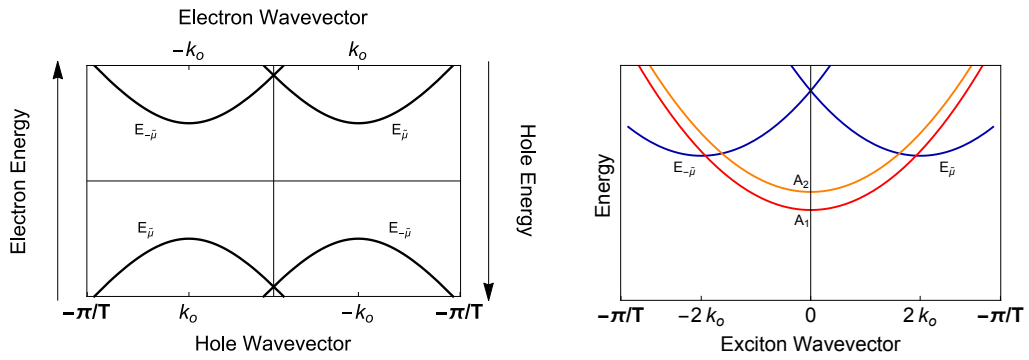

Figure 2.7: Valley degeneracy. Four-fold exciton degeneracy from inequivalent K and K' valleys. Left) The lowest energy electron and hole bands for chiral nanotubes. Right) The corresponding excitonic bands for chiral nanotubes. The anti-bonding (A_1) dark state, bonding (A_2) bright state, and cross-valley ($E_{\tilde{\mu}}$) non-zero momentum states. Reproduced from Figure 1, Barros, et al. [68]. For a treatment of all tube types see Appendix C.

momenta [54, 71]. Theoretical [72] and experimental [67] results have both shown that the mixing results in a ladder of states with the bright state having the highest energy and the anti-bonding dark state having the lowest while one or two weakly active or dark states may exist with intermediate energies.

Calculations by Spataru, et al., [73], using the DFT model described earlier concluded that the lowest energy exciton would be dark, or optically inactive, followed by a single bright exciton and then a degenerate pair of dark excitons of higher energy consistent with the exciton manifold presented in Figure 2.7. Alternative semi-empirical calculations, however, have found the ordering of the excitons to differ with the lowest energy exciton still dark, followed by a degenerate set of dark excitons as well as a weakly allowed state, all below the highest and bright exciton [74, 75]. *Common to all of these results is the observation that the lowest energy exciton is dark*, a result that has been confirmed by experiment through magnetic brightening [71].

More recent studies have refined the earlier calculations with careful attention to the representative Hamiltonians and density functionals chosen to represent the physical system of a nanotube. One extensive time-domain DFT study by Kilina, et al., determined that the lowest energy exciton was dark, consistent with all of the earlier calculations, but that the highest energy exciton would be the bright exciton and two dark or semi-dark exci-

tons would lie in between, all within ~0.1 eV of the bright exciton [53, 54] consistent with measured results from Zhao, et al., [75].

It is important to note that these exciton manifold models still suffer from an inability to account for the many perturbations found in the real world. Variations in tube lengths, local dielectric, defects and impurities can all cause deviations from these models and do. Kilina calculated, for example, that the distribution of tube lengths alone in a practical sample can result in variations in exciton band mixing between the bright and dark states — the origin of the semi-dark states. And time resolved photoluminescence measurements noted an order of magnitude variation in lifetimes for different, isolated tubes of the same chirality [76]. It would seem that an entire book could be written simply focusing on these and many other variations. Despite the multitude of possible structural and environmental perturbations, however, *ab initio* calculations and measurements such as the magnetic brightening experiment noted above have shown that at least one dark exciton will lie below the bright exciton. In addition, ultrafast relaxation measurements have generally shown behavior consistent with Kilina's observation of two semi-dark excitonic states between the light and dark states [67].

2.5 Excitation and Relaxation from an Excited State

The exciton manifold described above provides a platform for understanding how an optically excited carbon nanotube will relax back to the ground state. The multi-level diagram in Figure 2.8 ties the various levels together in the generally understood relaxation cascade that can take place after excitation of the bright E_{22} excitonic state. Note that the nanotube could just as easily be excited into the E_{11} state in a degenerate pump-probe measurement. I will not consider this case since an E_{22} excitation and the subsequent relaxation paths are representative of typical non-degenerate (two-color) pump-probe experiments on CNTs including those of my research. Exciting a CNT into the E_{22} state instead of the E_{11} state also

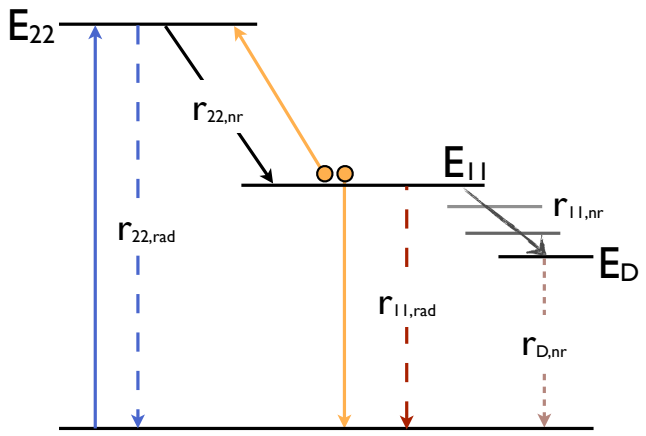

Figure 2.8: Excitation-relaxation in a carbon nanotube. Illustration of band edge excitation/relaxation transitions for E_{ii} excitons with r_{ii} relaxation rates. Initial excitation generates E_{22} excitons (blue) which primarily relax into E_{11} bright states (black). For high E_{11} densities exciton-exciton annihilation modifies the population distribution (orange). The E_{11} excitons may also either radiatively decay to the ground state (red) or further relax into long lived dark excitons (dark gray) at the bottom of the E_{11} ladder of singlet sub-states. Continuum states for E_{11} and E_{22} not shown.

makes it possible to selectively monitor nanotubes of a specific chirality in a polymer/CNT blend as will be discussed in more detail in later chapters (See Sections 3.4 and 4.1).

Figure 2.8 presents a simplified series of dispersionless band edge levels. From Figure 2.4 one could expect that such an energy level diagram for CNTs should be made up of approximately parabolic bands. However, given that the joint density of states of an exciton is significantly weighted to the band edge and that optical excitation does not contribute momentum to the system, focusing on the bandedge transitions should not lead to any confusion.

Populating the E_{11} State

In the initial step light resonant with the E_{22} transition (blue arrow) generates tightly bound excitons ~300–500 meV below the continuum state (not shown). Relaxation from the E_{22} state then progresses rapidly with a lifetime of only ~40–50 fs [77, 78, 67, 79] due to strong electron-phonon coupling (black arrow). The rapid relaxation is dominated by the

$E_{22} \rightarrow E_{11}$ (bright states) path at $\geq 80\%$ while some of the remaining population decays radiatively or directly into dark excitonic states below the bright E_{11} state [80, 81]. Additional weak pathways have been seen in phonon satellites [77, 82, 54] and transverse excitations [83]. While Manzoni, et al., attributed the rapid and dominant relaxation path to the narrow E_{22} excitonic state coupling with the E_{11} continuum (not shown) as a Fano resonance [78], a number of studies noted the lack of an optical signature necessary to indicate the presence of the free electron-hole pairs that would be generated by this relaxation process [84, 47, 48, 85]. An early [86], as well as a more recent [87] study, however, was able to electronically observe spontaneous dissociation of optically generated excitons into free electron-hole pairs confirming that at least some of the E_{22} excitons couple into the E_{11} continuum before re-condensing into the corresponding exciton. Despite evidence for dissociation the vast majority of E_{22} excitons will not follow this path and instead relax directly into excitonic states at a ratio of 10:1 [80].

Figure 2.8 also deliberately assumes that the top E_{11} state is the bright $1u$ singlet state. Transient grating measurements, however, have identified the primary relaxation pathway as coupling through at least one of the excited states of the E_{11} bright state [67]. The authors assume without argument that this is the $2g$ state presumably because this is the only excited state that can even be distinguished from the continuum in dynamical modeling [30]. With or without this intermediate step the bright $1u$ singlet state is rapidly populated by the relaxation of the E_{22} state.

Auger-like Exciton – Exciton Annihilation

The relaxation rate of the E_{22} state is rapid enough that it can outpace a relatively short excitation pulse. If the E_{22} lifetime is ~ 40 fs and the pump pulse is 100 fs then the relaxation will populate the E_{11} state almost as if it is being pumped directly — any delay due to the relaxation step would be shorter than the pump pulse. The direct result of this rapid population build-up can be the generation of a high density of excitons in the same state, in

this case the E_{11} state. In Figure 2.8 the orange arrows depict the consequences of this high exciton density. Confined to the quasi-one dimensional nanotube, the excitons will likely interact with each other. This can lead to an "Auger-like" exciton-exciton annihilation (EEA) process where one exciton decays transferring its energy to the other exciton.[5]

Several studies have observed that relaxation of the E_{11} state depends non-linearly on the intensity of the excitation [47, 89], determining that this non-linear behavior can be accounted for by the EEA depicted in Figure 2.8. For excitation intensities above $\sim 3\times10^{14}$ photons/cm^2 it was found that the Auger-like annihilation process may even dominate the relaxation kinetics at early times [47]. Below some threshold, however, the process can shut down [75]. This is intuitively due to a low density of excitons but the density may be lower than expected. Xiao, et al., found that EEA can still be efficient for as few as 2–6 excitons in a CNT only a few microns long [90]. At only 8.20×10^{12} photons/cm^2 Ma, et al., found that EEA finally becomes "minor" [91].

Populating the $E_{11,\text{Dark}}$ State

For those bright E_{11} excitons that do not transform through exciton-exciton annihilation, many undergo radiative decay from the E_{11} bright state (see, for example, the resulting PLE data described in Section 3.4). The vast majority of E_{11} excitons, however, will decay non-radiatively by cascading through the dark or weakly dark, even parity E_{11} states described above [76, 10, 67]. This cascading decay path takes place on the order of a few picoseconds and results in populating the long lived lowest energy singlet dark exciton [67, 74].

Dipole-Forbidden Relaxation The significance of the lowest exciton being dark should not be understated in the context of relaxation measurements and particularly for ultrafast relaxation studies in this case. Once an exciton is in this dipole forbidden state it is unlikely

[5] Strictly speaking the Auger recombination process in a semiconductor involves three unbound quasi-particle charge carriers, say two electrons and a hole (or vice-versa). Under collision one electron recombines with the hole transferring its energy to the other electron [88].

that it will obtain enough energy from the environment (where k_BT is only ~ 25 meV at room temperature) to overcome the ~ 100 meV needed to climb back into the radiatively allowed state. The exciton then finds itself in an effective trap state with a very slow decay rate compared to the radiative rate of the optically allowed bright state. Lifetimes of these dark states are on the order of ~ 100–300 ps [92, 67]. As a result the dark state acts as a population sink causing the radiative efficiency of the CNT to be quite low. Estimates of the quantum yield for photoluminescence are on the order of 10^{-3} [10] to 10^{-4} [76] — though Lefebvre, et al., was able to measure quantum efficiencies as high as 7% for suspended tubes essentially isolated from the environment [93].

References to the lowest energy dark state as a trap state, while common in the literature, may be misleading. Calling the dark state a trap is descriptive in the sense that it is tightly bound well below the radiative state. But the lowest energy dark state should not be thought of as a trap state in the sense of being bound to a defect site or unsaturated bond. It remains a free, highly mobile, exciton. As a result it may be more descriptive to think of the dark exciton as a metastable state instead. The fact that the excitons can be so mobile leads to yet another decay process. Zhu, et al., [94] found that the ground state recovery of nanotubes in an excited state followed a $t^{-0.45}$ recovery. The authors attributed this to sub-diffusive trapping of the dark excitons in a 1D system.

Non-Resonant Excitation

Excitations above the exciton resonances are still possible and can extend an absorption linewidth considerably. Chou, et al., observed strong absorption in a broad range more than 20 meV above the E_{11} resonance for (6, 5) nanotubes with additional absorption extending as far as 400 meV above [95]. The authors attributed a variety of multi-phonon processes to this extended absorption and the subsequent rapid relaxation to the radiative E_{11} state. Similar observations were also made by Htoon, et al., for a distribution of nanotubes where they found evidence for strong electron-phonon coupling when exciting the E_{22} resonance

leading to estimates of extremely rapid inter-exciton relaxation, as fast as ~ 20 fs, with correspondingly larger linewidths [77]. Excitation well above either resonance is also possible as can be seen in most fluorescence measurements. Nonetheless, the bright excitonic states described earlier capture almost all of the oscillator strength and excitations on resonance with an excitonic state dominate the absorption spectrum by orders of magnitude [46, 56].

Excited State Absorption

The relaxation steps suggested in Figure 2.8 all proceeded after an initial excitation tuned to the E_{22} resonance. As soon as a nanotube's excited state is populated, however, the exciton(s) in question can be promoted through any allowed transition. Such excited state absorption signatures were spotted in the earliest ultrafast excited state relaxation measurements taken on carbon nanotubes [96]. Since that first observation a number of instances of excited state absorption have been measured with almost as many different transitions to account for their occurrences. An important early study showed that the induced absorption tracked the resonant excitations of the nanotubes and were therefore a component of their excited state dynamics [97]. In this particular study the authors saw three absorption bands that they identified as excited state absorption within the exciton manifold: $E_{11} \rightarrow E_{22}$, $E_{11} \rightarrow E_{33}$, and $E_{22} \rightarrow E_{33}$. Support for this interpretation was seen shortly afterwards in two studies that observed induced absorption in the visible after pumping nanotubes to the first excited state, absorption consistent with the $E_{11} \rightarrow E_{33}$ transition [98, 78]. Excited state absorption has now been associated with transitions from the E_{11} or E_{22} state to higher states as just noted [98, 84, 97, 78]; from E_{11} states into the E_{22} continuum [67]; as signatures of bi-exciton formation [89, 85, 94]; and as intra-exciton transitions within an E_{ii} manifold, i. e. from the dark E_{11} state to the bright E_{11} state [46, 99, 100, 75]. Since these excited state transitions are mostly seen as an emerging differential absorption signature they are often referred to in the literature and below as photo-induced absorption (PA).

2.6 Summary

The electronic structure of carbon nanotubes can be largely defined in terms of the band-structure of graphene. By including the natural zone folding that occurs when graphene is conceptually rolled-up into a nanotube a series of free carrier transitions emerge that roughly track the optical resonances measured in the lab. The single carrier model, however, cannot account for the tightly bound excitons that dominate the optical spectra of CNTs. To accurately model the optical properties of these nanotubes we need a many-body treatment. In this way we can account for the strong Coulomb interactions that occur when charge carriers are confined to a nanotube. Calculations based on density functional theory confirm that the excited states of a CNT are made up of a series of tightly bound excitons associated with the $v_i \rightarrow c_i$ free carrier transitions. In addition to excited hydrogenic states of the individual excitons the spin and valley degeneracies lead to level splitting with a ladder of bright and dark states. As a result a carbon nanotube that is optically excited can be described in terms of the relaxation of an exciton as it radiatively decays or non-radiatively relaxes through a series of inter- and intra-band band transitions.

CHAPTER 3

Carbon Nanotubes in Organic Polymers

The initial motivation for my research had been the characterization of hybrid devices exploiting the different properties of polymers, nanotubes, C_{60} (Buckminsterfullerene), SnPc (Tin-phthalocyanine) and more, combined to form a carefully designed set of heterojunctions. The goal, as noted, was to maximize the potential energy harvested in a photovoltaic device by characterizing the evolution — from absorption to exciton dissociation — necessary for harvesting a photocurrent from sunlight. And the initial measurements, the same measurements that are the foundation of this study, were intended to characterize the relaxation of photoexcited states in a thin, carbon nanotube/polymer blend film. This chapter is focused on describing the steps taken to make and characterize the CNT/polymer films that were used in my research.

3.1 Nanotube Production and Separation

Carbon nanotubes can be produced in a number of processes. The nanotubes used in the experiments I will describe below were produced by the commercial company Unidym using the high pressure carbon monoxide (HiPCO) method [101]. Unidym describes the current version of this process as one in which a carbon monoxide gas in a high-pressure chamber at high temperature is blended with a gaseous catalyst precursor such as iron carbonyl. The catalyst precursor decomposes, and nanometer-sized metal particles form

from the decomposition. These tiny metal particles, serving as a catalyst, drive the decomposition of the carbon monoxide into carbon and carbon dioxide and facilitate the nucleation of the remaining dissociated carbon into carbon nanotubes [102].[1] The HiPCO method is not the only method for growing the carbon nanotubes (CNTs) used in ultrafast measurements. The cobalt-molybdenum catalyst (CoMoCAT) method in which CO is exposed to a cobalt-molybdenum catalyst on a silica support [104, 105] is also quite common. And pulsed laser ablation in which powerful ($\sim 500\,\mathrm{mJ}/27\,\mathrm{mm}^2$) pulses alternating between 532 nm and 1064 nm ablate a carbon/nickel/cobalt target in an inert Argon atmosphere [106, 107] has been used often. There has been a focus on HiPCO and CoMoCAT growth in part due to the method's ability to selectively enhance the growth of larger (CoMoCAT) or smaller (HiPCO) diameter nanotubes primarily through control of the catalyst particle sizes [104, 105], a control parameter that is not available using laser ablation.

Unfortunately, these nanotube generating processes are a bit chaotic. All of these methods produce a jumble of carbon nanotubes, both single- and multi-walled. And the single-walled nanotubes are distributed across varying (n,m) chiralities comprising $\sim 1/3$ metallic and $\sim 2/3$ semiconducting tubes [36]. In addition to nanotubes all these methods generate miscellaneous carbonaceous junk as well as residual particles from catalysts including iron (HiPCO) [10], cobalt and nickel (laser ablation) [106, 107], or cobalt and molybdenum (CoMoCAT) [104, 105]. Most of these nanotubes aggregate into tightly bound ropes with some of the residual junk swept along for the ride. This is a manifestation of the enormous surface-to-volume ratio of nanotubes and nanomaterials in general. By representing CNTs as smooth sided tubes Girifalco, et al., found that nanotubes around 1 nm in diameter had a cohesive energy of $\sim 0.5\,\mathrm{eV}/\text{Å}$ leading to the tendency to form parallel bundles (aka ropes) that are not easily separated and dispersed [108].

[1] As of 2/15/15 the website for Unidym has gone missing, reappeared and now appears to have been usurped. The interested reader may find information of value at the SouthWest NanoTechnologies website. SouthWest NanoTechnologies is an alternative commercial source for carbon nanotubes generated by the CoMoCAT method [103].

Both the bundling and contamination have a significant impact on optical measurements of CNTs. The presence of metallic tubes and residual metallic contaminants tightly bundled with the semiconducting nanotubes can lead to the rapid loss of excited states through quenching [109]. In addition, the close proximity of bundled nanotubes enables redshifting of the fluorescence as energy is transferred from higher to lower bandgap tubes [110, 111] and broadening [112].

In early research on carbon nanotubes one of the biggest challenges was to measure the intrinsic properties of individual tubes without the contaminant and bundling perturbations. In 2002 O'Connell, et al. described a complete process in which bundled nanotubes could be effectively separated into individual tubes [10, 113]. Employing their separation process they observed "dramatically reduced" photoluminescence for samples containing bundled nanotubes relative to dispersed tubes consistent with the expected quenching in bundles. They also observed that the absorption spectra of unprocessed CNTs showed considerable broadening around individual nanotube resonances. After separating the nanotubes using a process described below they saw strong photoluminescence from narrow peaks ($\sim 200\,\mathrm{cm^{-1}}$) with minimal ($\sim 45\,\mathrm{cm^{-1}}$) redshift relative to the absorption spectrum indicating that energy had not been lost through quenching or transferred to lower bandgap tubes. The presence of mostly individual nanotubes can be confirmed, then, by a strong, highly structured photoluminescence signal.

The separation process described by O'Connell first took the raw CNT material with all its bundles, extra carbonaceous junk and residual catalyst and sonicated it in a solution of sodium dodecyl sulfate (SDS). The SDS acted as a surfactant that would coat individual nanotubes while they were briefly separated from the other tubes by the pressure of the sonicator. They then further processed the solution by ultracentrifugation to separate the individual nanotubes from the remaining (heavier) bundles and miscellaneous junk. An additional step was to add the polymer poly(vinylpyrrolidone) (PVP) which competed with the SDS surfactant to wrap the individual nanotubes. This general process is now the

standard technique for producing polymer wrapped individual nanotubes. Variations on this process can involve the use of nanotubes generated by different processes as noted above, the use of various surfactants (even including DNA [114]) and their solvents, processing times, polymers, etc. but the basic idea remains the same. The results, however, can be surprisingly and deliberately different. In O'Connell's 2002 work, for example, they found that by varying the reactor pressure between 30 and 50 atm they could selectively enhance the populations of larger and smaller diameter tubes respectively [10]. And Fantini, et al., was able to exploit the DNA surfactant method to dramatically reduce the presence of metallic nanotubes [115].[2]

3.2 Host Polymers and Photoactivity

The polymers incorporated in the CNT separation processes described above were initially chosen for their chain-like conformations and ability to wrap along and around the extended lengths of these nanotubes [116]. And further research determined that modifications to the dispersing process can have a significant effect on the final nanotube populations. Nish, for example, showed that by dispersing carbon nanotubes in different polymers - poly(9,9′-dioctylfluorene) (PFO) and functionalized derivatives as well as poly[9,9-dihexylfluorenyl-2,7-diyl] (PFH) and poly[2-methoxy-5-(2′-ethyl-hexyloxy)-1,4-phenylene vinylene] (MEH-PPV) - the final nanotube distribution could be altered dramatically [116, 117]. Another study by the same group showed dramatic variation in both the selective dispersion and photoluminescence intensity with changes in the dispersing solvent [118].

If all one wanted to do was to select and disperse nanotubes then that would be pretty much the end of our polymer story. For devices like photo-detectors and solar cells, how-

[2] A slightly different purification method described by Kymakis, et al. has been shown to reduce the presence of metallic tubes. The authors measured a distribution of 90% semiconducting tubes before dispersing them in a polymer [19].

ever, there is the additional consideration of photosensitivity. In fact the nanotubes in such devices have come late to the game. Considerable and ongoing research is being carried out on photoactive polymers themselves and their incorporation into multi-junction organic solar cells.[3] Photo-excitation of these polymers results in strongly bound excitons. If these excitons can be dissociated into free charge carriers they can be harvested as a photocurrent. In typical photoactive organic polymers such as PVP and its derivatives, however, these excitons may have binding energies of over 400 meV [120]. With such high binding energies an exciton cannot dissociate until it finds an energetically favorable interface [121]. Unfortunately the exciton diffusion length in these polymers — the distance over which excitons can migrate before being lost to decay — is limited to only 5 – 10 nm [122, 123]. This severely limits the functional thickness of polymer layers in organic solar cells significantly reducing their total absorption. And this is despite considerable attention being given to optimizing the nanoscale morphology of these polymers [119]. Enter semiconducting carbon nanotubes with their exceptional electron mobility in excess of 100,000 $cm^2/V{\cdot}s$ [13].

Carbon Nanotubes — Mobility for Organic Polymers

As early as 2001 Kymakis and Amaratunga blended carbon nanotubes in poly(3-octylthiophene) (P3OT) to increase the short circuit current in the polymer layer of a potential new composite photovoltaic device [121]. If the nanotubes are defect-free they can act as molecular wires in the photoactive polymer host and efficiently transport charge carriers through the material [124]. They can also play an important role here as electron [121, 125, 126] or hole [127] acceptors where excitons in the polymer can efficiently dissociate at the nanotube interface. In the device investigated by Arnold that motivated this research the nanotubes certainly played the role of high mobility molecular wires. In their device the CNTs accepted electrons from the excitons generated in the polymer matrix

[3] See for example the recent second edition of Organic Photovoltaics by Brabec, Scherf and Dyakonov [119].

as well as aided in the transfer of un-dissociated excitons. But they also played a role as light harvesters themselves where the excited states were neutral excitons. Mobility in this scenario is also important but transport is diffusive rather than driven by a potential gradient. An analysis of exciton diffusion in a one-dimensional system leads to the descriptive relation $L = 2\sqrt{D\,\tau}$ where L is the effective exciton diffusion length, τ is the exciton lifetime and D is the diffusion coefficient [128]. The exciton length, L, can be interpreted here as the length an exciton can travel during its lifetime. The longer the ideal diffusion length, however, the more likely the exciton will encounter a process dependent quenching site. Conversely, the more prevalent the quenching sites, the shorter the effective diffusion length will be. As a result measurements of this length have been seen to vary significantly with Luer, et al., finding a diffusion length of only 6 nm [129], Cognet, et al., finding 90 nm [130], and Siitonen, et al., achieving a range of 190 – 370 nm [131] where the latter took pains to minimize all possible defects that could facilitate quenching of the exciton (for a diffusion length of ~ 100 nm they observed that the exciton would be exposed to upwards of 104 carbon atoms — and possible defect sites — along the nanotube). Thus while the diffusional mobility of the excitons may facilitate transport to a desired dissociation site it is just as efficient at facilitating transport to a quenching site.

If there is a consistent message in the results of the previous paragraph, it is that the diffusion length is highly process dependent and will vary with every sample. In a recent study by Ishii, et al. nanotubes were suspended over empty troughs in order to minimize such environmental effects. As expected they found even longer diffusion lengths (~ 470 nm – 1.1 μm) but, despite careful isolation, defects and end quenching could not be ignored [132].

Host Polymer Selection (Polymer/CNT Blends of Interest)

Three photoactive polymers being studied are of interest to us: poly[2-methoxy-5-(3′,7′-dimethyloctyloxy)-1,4-phenylene vinylene] (MDMO-PPV), poly(3-hexylthiophene)

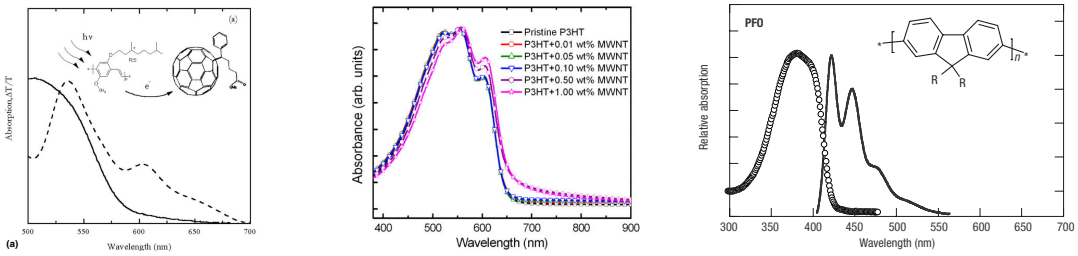

Figure 3.1: Absorption spectra for MDMO, P3HT and PFO. Left) MDMO absorption spectrum (solid line), from Brabec, et al., [133]. Center) P3HT absorption (black line — difficult to distinguish from blue line), from Wu, et al., [127]. Right) PFO absorption spectra (circles) from Chapell, et al., [134].

(P3HT) and poly(9,9′-dioctylfluorene) (PFO). The MDMO-PPV and P3HT were of particular interest in my earliest measurements as they were key components in the nanotube/organic heterojunction photodetector developed by Arnold, et al., [16]. The data of interest, however, was almost all taken on samples based on the polymer PFO. Absorption spectra for all three can be seen in Figure 3.1.

When we measure the absorption spectra of these polymers blended with carbon nanotubes we find that all three polymers absorb to the blue end of the typical CNT absorption lines of the first two excited states. Unfortunately, in the cases of the MDMO-PPV and P3HT polymers their absorption spectra also extend far enough into the red that they overlap with many of the E_{22} nanotube resonances in the visible. The absorption spectrum of P3HT blended with nanotubes can be seen in Figure 3.2. The inset shows the general range of the E_{11} resonances but the E_{22} resonances are indistinguishable from the P3HT absorption shoulder in the visible. As a result of this overlap, pumping one of these blends in the visible can simultaneously excite both the polymer and the nanotubes. In addition, excitation of these polymers can result in the transfer of energy to the embedded nanotubes [117].

The original motivation for this research was to improve the performance of hybrid CNT/polymer devices. In order to investigate the interaction, dissociation and diffusion of free charge carriers and excitons within both the host polymer and dispersed carbon nanotubes some baselines were needed. In particular, in order to distinguish between any con-

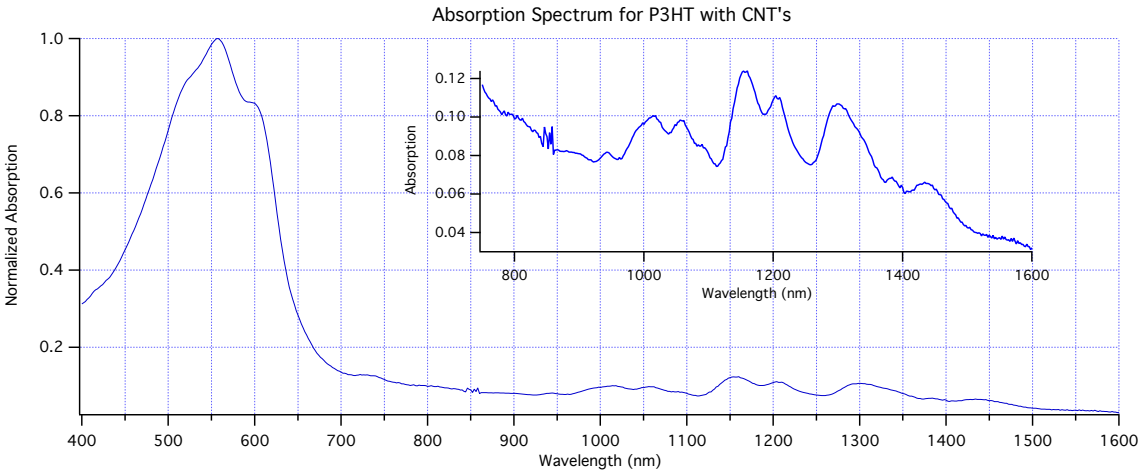

Figure 3.2: Absorption spectrum of P3HT/carbon nanotube blend. Dominant P3HT peak with 1000 nm tail attributed to the CNT ensemble. Contributions from the CNTs in the visible range are obscured by the P3HT absorption. Inset: Near IR region of the same spectrum with enhanced vertical scale. The structure results from the complex underlying contributions from many different nanotube chiralities. The squiggles near 850 nm are an artifact from the spectrometer switching visible and NIR gratings. Spectrum measured by Celia Cunningham.

tributions from the polymer or carbon nanotubes I needed to establish a baseline contribution from the nanotubes themselves. For reasons related to the expected nanotube distribution the pump pulse was tuned to ~ 650 nm. Around this wavelength neither MDMO-PPV nor P3HT could be used since the tails of their absorption spectra extend past 650 nm. In order to excite only the CNTs and avoid exciting the host polymer the PFO polymer was used instead. From Figure 3.1 it can be seen that the higher bandgap of this polymer puts the absorption peak out below 400nm and more importantly the red limit of the absorption is weak or nonexistent above 500 nm. By exciting CNTs in PFO then I could accurately measure the photo-response of the nanotubes themselves in a similar polymer that would not be excited by the pump beam.

The surprise was that all the interesting results appeared in the measurements taken using PFO/CNT blends. As a result, most of the research discussed in the following chapters will focus on samples made with PFO instead of the polymers used in the original device designs.

3.3 Sample Preparation

The samples used in all of my measurements were created by Celia Cunningham and Jeramy Zimmerman as part of a collaboration with the University of Michigan research group led by Professor Stephen Forrest. The processing generally followed the earlier description of O'Connell's research (see Section 3.1) and the published version of the sample production provided by Dr. Zimmerman is included in Appendix D. After processing, the dispersed nanotube/polymer solution was spread with a film casting knife to a roughly 100 nm thick film on quartz slides. The film was then dried before the slides were unceremoniously broken into small slivers that could be placed in the narrow confines of a cryostat (See Section 4.3).

3.4 Characterization

The sensitivity of any distribution of carbon nanotubes to every step in the process – from creation to dispersion in a polymer – necessitates that the final samples are characterized. The resulting samples will contain a distinct distribution of nanotubes together with variations in their densities.

Absorption

Characterization of a polymer/carbon nanotube blend begins with an absorption spectrum. In Figure 3.2 we can see the advantage of adding a broad distribution of carbon nanotubes to the P3HT polymer. Comparing this figure with the earlier figures (Fig. 3.1) of MDMO-PPV, P3HT and PFO without nanotubes the absorption range has been extended from 650 nm to almost 1600 nm. The manner in which the carbon nanotubes contribute to the broad absorption shoulder can be inferred from the inset of Figure 3.2 showing only the near-IR region. The narrower amplitude range in the inset hints at a complex underlying structure. The individual absorption linewidth of a single CNT has been measured

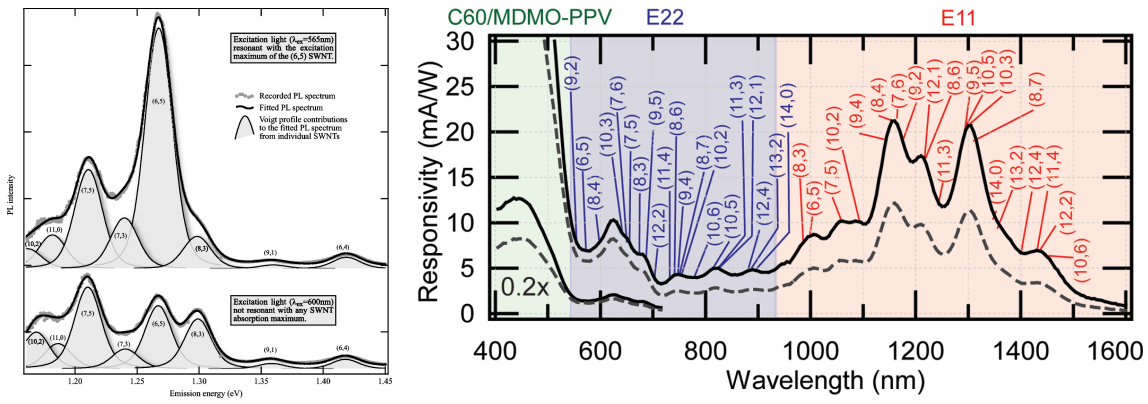

Figure 3.3: Assigning (n,m) chiralities. Left) Photoluminescence spectra showing underlying Voigt profiles of contributing chiral species from Figure 2 of Jones, et al. [135]. Right) Visible-NIR focus on photoresponsivity of prototype device from Figure 2(B) of Arnold, et al., [16]. A qualitative assignment is made of the many chiralities that collectively contribute to the 1000 nm extension.

in several studies to an average of ~25 meV (ranging from ~10-40 meV) [10, 112, 77] though sample heterogeneities can easily broaden these to 100meV [112]. The result then is a broad distribution of nanotubes of widely varying linewidths combining to form this roughly 1000 nm extension to the host polymer's absorption range. An example of the underlying contributions can be seen in the results from Jones, et al., [135] shown in the left hand diagram of Figure 3.3. The right hand diagram qualitatively identifies the nanotube chiralities underlying the absorption spectrum from the photodetector described in Chapter 1 [16]. Such a qualitative assignment of the contributing nanotubes can be carried- out directly by comparing the various peaks in the absorption spectrum to predicted values. By referring to the published empirically derived values determined by Bachilo, et al., the presence and relative positions of both the E_{11} and E_{22} resonances can be unraveled and the chiralities contributing to the extended absorption shoulder can generally be identified [42].

Appendix E contains a similar tabulation of E_{11} and E_{22} resonances determined by fitting the shoulder of the absorption profile from my samples with a series of absorption lines after the fits by Jones (Fig 3.3) and Hertel, et al., [80]. I'll describe this fitting in more detail in Section 4.1.

Beyond the intrinsic homogeneous and inhomogeneous broadening of the exciton

linewidths, several issues can influence the nanotube absorption spectrum. Nanotubes in undispersed bundles show significant broadening due to tube-tube interactions [112] consistent with inter-tube electronic dispersion [33]. While in a follow-up to their experiment determining absorption linewidths for dispersed nanotubes Hagen, et al. found that the linewidth for a particular chirality could vary from tube to tube due to sample dependent variations (Perhaps not surprisingly they also found that the relaxation time also varied). In addition to residual bundling these "extrinsic" perturbations were attributed to structural heterogeneities and length dispersions [76]. Other studies have shown that local variations in the structural and chemical environments of a nanotube [136, 84] as well as a susceptibility to unintentional doping [137] can influence the optical response of individual nanotubes.

Bundling was already discussed (Sec 3.1) as the reason ultra-sonication is needed to disperse the nanotubes. The importance of this step can be seen indirectly in Figure 3.4 from a study by Arnold, et al., that observed a significant sharpening of the absorption lines after centrifugation due to the removal of heavier bundles and contaminants [138]. Ironically sonicating to reduce bundling can also result in damaging and shortening the nanotubes. As a result, complete dispersion of the nanotubes can actually increase the heterogeneous broadening of the absorption linewidths.

Taken together the impact of process variations and sample heterogeneities suggests that the characteristics of each nanotube absorption line may vary from sample to sample and can only be compared qualitatively to the literature. Despite the potential for variation a sample of dispersed nanotubes with many different absorption resonances can combine to extend the absorption range of the host polymer by hundreds of nanometers.

Photoluminescence Excitation

There are at least two drawbacks to characterizing a polymer-CNT blend through its absorption spectrum. We can see, for example, from Figure 3.3 above that there is significant overlap in the exciton resonances making it difficult to identify the amplitude and mean

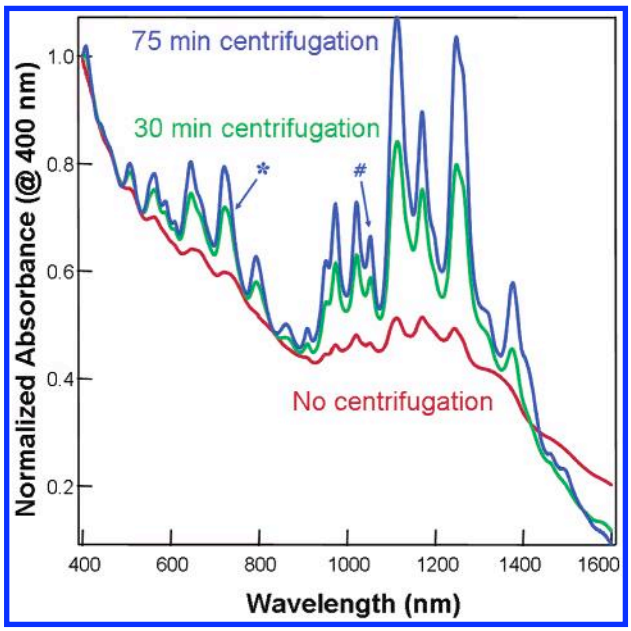

Figure 3.4: Effect of ultra-centrifugation on CNT/surfactant blends. Dispersed CNT/surfactant blends from Arnold, et al., [138]. Normalized traces show improved optical differentiation of nanotubes with longer ultra-centrifugation times. Longer times result in more complete removal of bundles and contaminants reducing background and overlap.

of the various absorption lines. Another drawback involves bundling. An absorption measurement can only confirm the presence of a given nanotube chirality. But we know from the discussion above that the presence of undispersed bundles can lead to quenching. If the nanotube is bound to other nanotubes any absorption is likely to be almost immediately quenched. In the context of harvesting light to generate photocurrent this would be a complete loss and highlights the need to know if residual bundling is present. The ease of measuring the absorption spectrum, then, is offset by the absence of this additional information. Figure 3.5 exhibits two, high-resolution photoluminescence excitation (PLE) maps from Hwang, et al., [118] that address these limitations. Conveniently, these PLE maps are for nanotubes dispersed in PFO, samples comparable to those used in my research. The excitation and fluorescence ranges in Figure 3.5 are also representative of the nanotube resonances we typically encounter. The graphs represent excitation along the vertical axis and photoluminescence along the horizontal axis. A PLE map is really just a series of fluores-

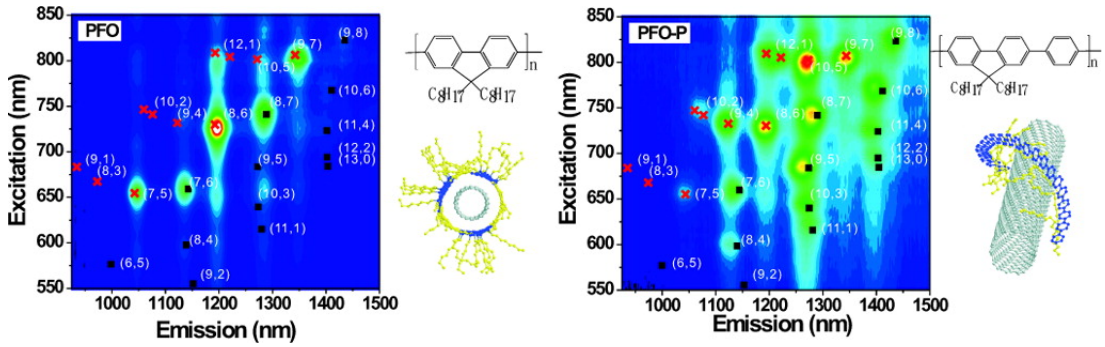

Figure 3.5: PLE maps of CNTs in PFO. Photoluminescence excitation maps showing selectivity of different nanotubes when dispersed in the polymers PFO (left) and closely related PFO-P (right) from Hwang, et al., [118]. Excitation wavelengths are recorded along the vertical axis. The resulting luminescence (dipole allowed fluorescence) at each excitation wavelength is recorded along the horizontal axis. Chiral species, (n,m) can be identified by comparing results to theory and further validated using Raman data [42]. Figure only available online.

cence scans as the excitation is stepped through a range of wavelengths. The spectral ranges for both excitation and fluorescence are chosen to overlap the E_{22} and E_{11} resonances respectively of the CNTs in a given sample. The localized blobs dotted across the PLE maps represent resonant absorption by a set of nanotubes followed by their radiative decay at lower energy. A nanotube is resonantly excited whenever the excitation wavelength overlaps the absorption line of its E_{22} excitonic state. From Section 2.5 we know that a majority of the E_{22} excitons then rapidly and non-radiatively relax into the E_{11} state. For each excitation wavelength a spectrometer then sweeps through the emission range in question measuring the resulting fluorescence from the radiative decay of these E_{11} excitons. This process repeats across the entire excitation range of interest and the combined scans are our PLE maps. One advantage to such a PLE measurement over absorption is immediately apparent if we consider the $(7,5)$ and $(7,6)$ nanotubes in the left-hand graph (The right hand graph will show the same thing, just not as clearly). Both of these nanotube chiralities have E_{22} resonances – corresponding to ~ 650 nm for this sample – that would be difficult to distinguish in an absorption measurement. When the resulting fluorescence is measured, however, the two chiralities emit at distinct wavelengths. In the resulting PLE map the

(7, 5) and (7, 6) nanotubes no longer overlap and can be clearly distinguished. Similarly, if somewhat conversely, the right hand graph makes it clear that the (8, 4), (7, 6) and (9, 4) nanotubes will all fluoresce at around 1130 nm but that we can distinguish between them since each chirality has a distinct E_{22} excitation resonance. The 2D characteristic of PLE measurements like this allows us to distinguish between most of the contributing chiralities. Another advantage of PLE measurements is their sensitivity to bundling. If a nanotube is still bound to other tubes we can expect a significant reduction in the photoluminescent signal due to quenching [118, 135]. Thus PLE measurements with a strong signal-to-background ratio can be an indication of effectively dispersed individual nanotubes. In the absence of any metallic tubes or residual metallic particles, however, absorption by bundled nanotubes can still lead to significant changes in the PLE maps. Bundling has been found to facilitate efficient energy transfer from tube to tube resulting in excitons moving to and decaying in lower bandgap CNTs [139, 140, 141, 142]. This transfer-relaxation process is likely to be the source of the unassigned faint blobs at around 650 nm excitation and 1200 nm emission in both of the PLE maps of Figure 3.5. There are no nanotube chiralities that correspond to this excitation/emission pair. We can speculate[4] that one or more of the nanotubes with higher energy E_{22} states is contributing indirectly to this fluorescence. Let's assume for illustration purposes that these are the (7, 6) tubes excited at 650 nm. The E_{22} excitons of the (7, 6) nanotubes may then take any number of alternative paths to the lower E_{22} and/or E_{11} states in any neighborly (8, 6) tubes. The resulting E_{11} fluorescence would be consistent with emission from the (8, 6) nanotubes but appears to have been excited at 650 nm, well above the E_{22} resonance of these CNTs. While PLE measurements might be ideal in comparison to a simple absorption spectrum they are not necessarily the measurement of choice. In practice such a measurement requires a triple-monochromator for adequate resolution and an actively cooled photodetector to capture weak fluorescence in the near-IR. In addition, since the entire emission spectrum must be measured for each

[4]The authors did not address this.

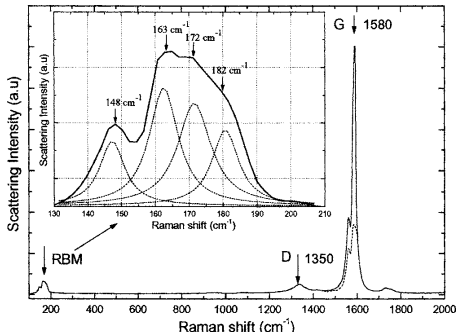

Figure 3.6: Raman spectra of CNTs. "Figure 1 Raman spectrum of the surface of a spin-casted purified (solid line) SWNT film and (dashed line) ASWNT film." From Kymakis, et al., [19]. The G′ mode at $2\omega_D$ is outside the range of the graph.

excitation wavelength, these measurements can take days to complete.

Raman Spectroscopy

Raman spectroscopy has also been used to characterize carbon nanotubes. Before methods for dispersing nanotubes were developed PLE could not be used for characterization due to quenching within the tightly packed bundles. Since Raman scattering isn't as sensitive to quenching much of the early characterization of CNTs is due to Raman spectroscopy. While it does not have the intuitive advantage of distinguishing between multiple chiralities that PLE does, it can bring additional tools to the table (or lab bench in this case). Figure 3.6 from Kymakis, et al., shows a representative Raman spectrum exhibiting three characteristic modes – the radial breathing mode (RBM), disorder or defect (D) band and graphite like (G) bands [19]. Since I did not carry out any Raman measurements this subject is outside the scope of my research. However, it is at least worth mentioning these modes as typical results are relevant to any sample with a blend of tubes.

Radial Breathing Mode The bumpy little band seen just below 200 cm^{-1} represents the radial breathing modes (RBMs) of the nanotubes. The frequencies of these modes are inversely proportional to the tube diameter and as such can be used to distinguish between different chirality tubes [143]. Just as with an absorption measurement, however, we can

see from the inset that the linewidths and proximity of these resonances conspire to produce a broad structured peak that requires careful fitting to extract the contributing chiralities. Some of this overlap ambiguity can be eliminated by varying the excitation energy in the process known as resonance Raman spectroscopy generating data that closely resembles PLE data. If the excitation corresponds to an exciton resonance the RBM is enhanced. Of course this can mean exciting multiple chiralities with overlapping resonances but, taken together with theoretical predictions, differences in tube diameter and variations in population distributions the resonant excitation has been used to distinguish between many of the exciton resonance energies [42, 143, 144]. Unlike PLE measurements this method has the advantage (or disadvantage if you like) of being able to identify resonant excitation of metallic carbon nanotubes since there is no quenching mechanism.

Nanotubes of a single chirality would exhibit a comparatively sharp peak for the RBM band – an observation that has been used recently to verify the purity of specially fabricated nanotubes. In one experiment nanotubes were generated using tungsten-based bimetallic alloy nanocrystals as catalysts to generate $(12, 6)$ CNTs [145]. In a second experiment nanotubes were generated from designer graphene precursors resulting in $(6, 6)$ CNTs [146]. In both experiments the Raman spectrum showed a very narrow RBM peak from which the authors could verify that their experiment yielded nanotubes of a unique or predominant chirality.

G Band The G band is a function of the highest-frequency optical phonon modes in a nanotube, modes also associated with the G band of graphene. For both materials these modes originate from vibrations in the carbon-carbon bond of the two-atom graphene basis. Following Saito, et al., the G band is really two bands, the G^+ and G^- bands corresponding to the LO phonons (vibrations in the axial direction) and TO phonons (vibrations in the circumferential direction) respectively for semiconducting tubes [147]. Variations in the frequency and lineshape of the G^- band have been particularly helpful in understanding

CNTs. They have been found to shift with structural variations in the tubes; metallic vs semiconducting cases; and a number of studies have focused on the G^- band as a way of measuring electron-phonon coupling observing evidence of a Kohn anomaly leading to a "softening" of the LO phonon and a reversal of the LO and TO roles with respect to the G^+ and G^- bands [148, 149].

D Band The D band is useful for a very different reason. This band results from a double resonance process incorporating scattering by both a phonon and a defect. It can be facilitated by residual carbonaceous junk, molecular bonding between the nanotube and the surrounding dielectric or other symmetry breaking defects [147]. As a result it can be used as a qualitative measure of the final nanotube blend. Observation of a D band in the Raman spectrum can be an indication of an insufficiently processed sample. But a lack of a D band does not guarantee a quality sample. There is a catch that comes with "adequately" dispersing the nanotubes with high power sonication. Under-sonication results in considerable residual bundling and the correspondingly limited nanotube dispersion will produce a stronger D band. Sonication in general, however, often causes tube cutting resulting in a better quality distribution but one containing many shortened nanotube lengths [10]. Kilina, et al. showed theoretically that this has a direct impact on the effective absorption cross-section and by extension the signal strength from samples containing heavily sonicated CNTs. Shorter tubes result in reduced, blue-shifted absorption spectra [53]. As a result there is a trade-off during the sonication process between separation yield and excessive shortening of the tubes that the D band does not account for. On the positive side, Raman measurements of ultra-sonicated carbon nanotubes showed strong radial breathing modes with a D band that was nearly absent indicating little or no damage to the tube surfaces [10].

G′ mode One additional band, out of range in Fig. 3.6, is referred to as the G′ mode. It is a second-order Raman process like the D band and, at $2\omega_D$, is the D band overtone. This band differs from the D band in that it represents the double resonance process of scattering

by two phonons [147].

3.5 Summary

Despite the chaotic processes used to generate carbon nanotubes and all the carbonaceous and metallic junk that comes with it a reasonably straight-forward methodology for dispersing and filtering nanotubes has been developed. The use of various solvents and host polymers that selectively influence the chiral distribution of nanotubes in the final blend also contributes to a degree of control over generating nanotube/polymer films. The resulting films can be comprised of various polymers with a highly enhanced chirality or a broad distribution of nanotube species all having unique optical properties that can be tailored to an experiment or device. Absorption and photoluminescence excitation spectra of CNT/polymer blends can give us qualitative descriptions of each concoction. And the quality of the blends can also be observed through Raman scattering if needed.

CHAPTER 4

Characterization and Ultrafast Spectroscopy of Carbon Nanotubes

This chapter focuses on describing the general pump-probe methods used to measure the ultrafast relaxation of excited states in carbon nanotubes (CNTs). Exciton and free carrier dynamics in carbon nanotubes predominantly take place within a few picoseconds after excitation while many relaxation steps following the initial excitation can have lifetimes of only a few tens of femtoseconds. In order to observe the dynamics of a system that evolves on such a short time scale this research incorporated ultrafast pump-probe spectroscopy. Time domain spectroscopy in this case exploits the high temporal resolution of near transform limited broadband pulses and femtosecond scale time steps to follow these extremely rapid dynamics.

In order to target nanotubes of a single chirality the method requires an accurate characterization of the polymer/nanotube films we want to study. Before exciting or measuring a resonant transition we need to know where it is. And since the bandstructure of isolated nanotubes is particularly susceptible to process variations and the local environment each new blended film should be characterized.

Reliable pump-probe data also requires an understanding of the limitations of any given sample. Issues like exposure to the environment, the potential for optical damage, and others are discussed here since they all have to be taken into account in order to ensure accurate results.

4.1 Characterization of Polymer/Nanotube Films

The samples used in my measurements were the result of a collaboration with the research group lead by Stephen Forrest at the University of Michigan. Unless noted otherwise all of these samples were fabricated by Celia Cunningham as part of this collaboration. The samples were all thin polymer films of roughly ~ 100 nm thickness on quartz slides. After fabrication the films were isolated from the environment in a cryostat as described in Chapter 3. The films on some slides were limited to the basic polymer in order to identify the polymer's contribution to the total signal. For the majority of samples, however, the polymers were blended with a broad distribution of CNTs then extracted from the supernatant after ultracentrifugation (For the specific details see Appendix D). Streaking in the films was overcome by scanning across the sample and selecting regions at the low end of the total absorption. Regions with this character made up broad islands of consistent absorption and were distinct from regions where residual bundles could be visibly observed.

The blended polymer/nanotube films were also checked for any anisotropic sensitivity to the polarization of the pump or probe and none was seen. The orientations of the nanotubes throughout the polymer films could therefore be assumed random in all measurements.

Linear Absorption Spectra

The challenge in understanding any measurement on a heterogeneous distribution of CNTs is knowing which nanotubes are contributing to the overall signal. And while the previous statement may seem obvious, determining which nanotubes are contributing to a measurement and why requires some care. This care takes on added importance if the objective is to target a specific chirality. To do so an accurate knowledge of both the E_{11} and E_{22} resonances in necessary.

In a broad distribution of CNTs each chirality will contribute its own set of absorp-

tion resonances. Combined there will be frequent overlaps of the absorption lines (recall Fig. 3.3) as well as a likely interaction with the host polymer. You may have also noticed in Chapters 2 & 3 that process variations and environment contribute to substantial variations in the nanotube energy profile and dynamics as well.

In order to correctly interpret the dynamics of an ultrafast measurement then, we need a full characterization of the excitation properties of the polymer/CNT film being measured. This includes ruling out indirect excitation of the CNTs by the host polymer, fitting absorption spectra for exciton resonances and validating the chiral distribution in the pump-probe neighborhood with photoluminescence excitation (PLE).

Resonant Transitions — Identifying Chiral Distributions.

The most direct characterization of a polymer/CNT blend is given by a linear absorption spectrum. Figure 4.1 exhibits the absorption spectrum of the PFO/CNT blend film on which this dissertation is based. The dominant poly(9,9′-dioctylfluorene) (PFO) absorption can be seen in the large peak to the left covering ~ 300 nm – 450 nm. Beyond 450 nm the contribution from a broad distribution of CNTs extends as far as 1500 nm, limited here by the spectrometer's range. The inset focuses on the broad shoulder (with the background removed) in order to emphasize the underlying complexity of the CNT absorption spectrum. This spectrum is built up as demonstrated in Fig. 3.3 (a) from many individual nanotubes of varying chirality. If one is playing fast and loose and only needs to show that many chiralities are likely present a good first approximation can be made quickly from this spectrum. This was demonstrated in part (b) of the same figure. To generate a similar figure one need only compare the structure in the absorption to empirical tables[42, 40] and make some good guesses. Specific resonances and linewidths can be distilled from the absorption spectrum but require a little more effort. A quantitative fit to the spectrum must account for the background signal, nanotube distribution and substantial overlap of the many different absorption lines.

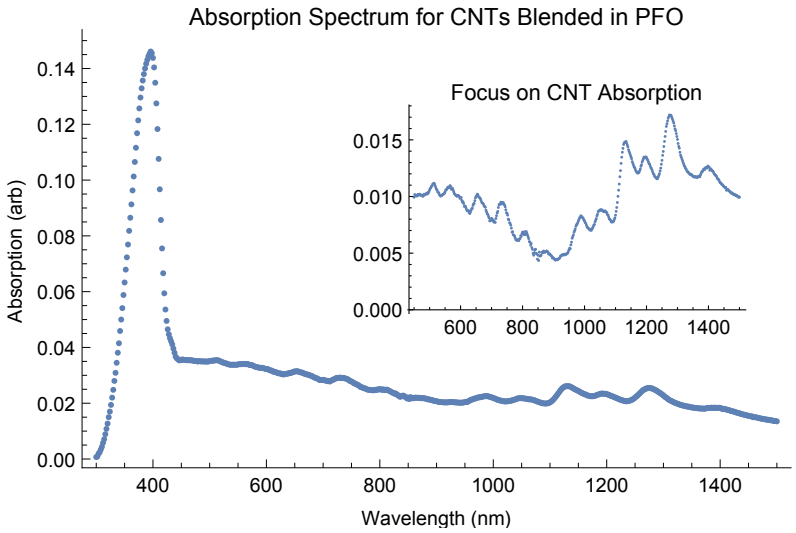

Figure 4.1: CNT/PFO absorption spectrum. Raw absorption spectrum of carbon nanotubes blended in PFO. Inset shows detailed shoulder structure after background subtraction.

Absorption Background

The spectrum we are looking for rests on a broad absorption shoulder variously ascribed to residual metallic catalyst [109], residual carbonaceous junk (plasmonic absorption [150, 96]) and residual bundling [10], all due to the generation method along with under-sonication and under-centrifugation. The shoulder will also include contributions from the long underlying absorption tail of metallic nanotubes that extends well into the near IR [151]. Ironically, this background signal can be exacerbated by over-sonicating a sample resulting in unintended chemical changes including induced chemical functionalization [130, 137] and nanotube cutting [76, 10]. Both changes can lead to inhomogeneous broadening of the individual nanotube absorption lines and augment the background. The broad range of the shoulder allows us to estimate this background fairly accurately as a simple linear offset with a well defined slope. Determining the best amplitude, or even a more representative mathematical form, of the offset would have required additional characterization of the sample during processing (see Naumov, et al., 2011 for specifics [151]). Despite this, errors in estimating the amplitude of the linear offset are likely small and will systematically effect all tubes.

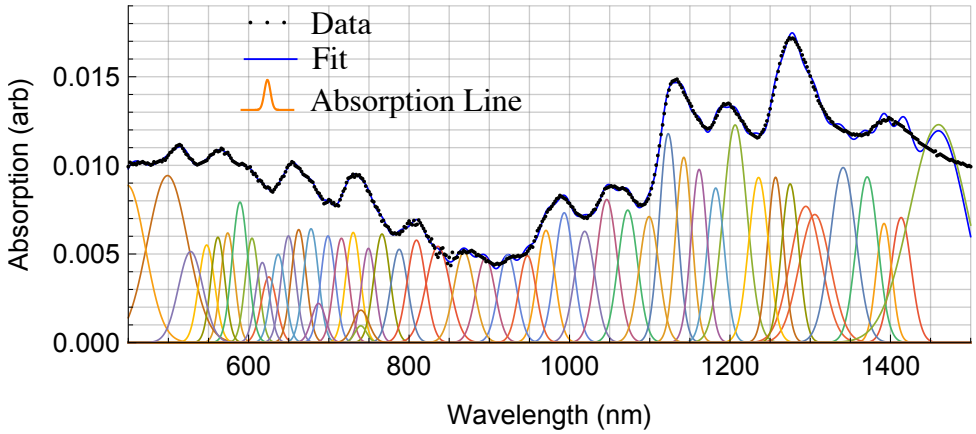

Figure 4.2: Substructure of complex absorption spectrum. Many individual nanotube absorption lines combined result in the structured variation of the absorption spectrum. Some nanotube chiralities may be missing - see text for details.

Extracting Resonant Absorption Lines

After subtracting the background the remaining absorption spectrum represents the combined contribution of many carbon nanotubes. There will be absorption lines for each of the many chiralities present. And for each such chirality this line will represent both homogeneous and inhomogeneous broadening, the later a result of the many perturbations noted above. Jones, et al., 2005 determined that the two broadening mechanisms contributed roughly equally to the linewidths so that in order to accurately fit the absorption spectrum of a specific chirality one would need to assume it has a Voigt profile combining both its Lorentzian and Gaussian characteristics [135]. In this case, due to the potential error in estimating the absorption background noted earlier and knowing in advance that residual bundling is present (See 4.1) we must assume that the lineshape leans heavily towards the inhomogeneous limit. As a result the best fit is calculated using only a simple Gaussian profile. Figure 4.2 shows the result of fitting the absorption resonances of 25 CNTs to the absorption shoulder seen in Fig. 4.1.

The collection of nanotubes chosen for fitting the absorption spectrum were selected according to several criteria: They were well represented in the photoluminescence excitation spectrum described in Section 4.1; They were typically present in similarly processed

Table 4.1: Target excitation neighborhood. Transition energies and linewidth estimates for select chiralities.

Chirality (n,m)	E_{11} Resonances			E_{22} Resonances		
	λ_c	E_{11} (eV)	ΔE_{11} (meV)	λ_c	E_{22} (eV)	ΔE_{22} (meV)
(6, 5)	993	1.25	35	574	2.16	77
(8, 4)	1123	1.10	26	604	2.05	67
(7, 5)	1046	1.18	34	650	1.91	63
(7, 6)	1142	1.09	22	662	1.87	61
(8, 3)	971	1.28	34	678	1.83	59

samples discussed in the literature [118, 116, 117]; After initial attempts to fit the spectrum there were evident gaps that indicated the presence of nanotubes not simply assumed to be in the original collection. The final collection was not meant to identify every single CNT chirality contained in the polymer film. It was only needed to capture the resonant excitation wavelengths of those tubes that might contribute to the dynamics seen in my differential transmission measurements. As a result, additional tubes were chosen if they bracketed the resonant tubes to limit lateral drift errors in the fitting. Tubes were also deliberately not included if there was no indication of their presence so that they would not compete with known tubes. A summary of the most relevant results can be found in Table 4.1. The full set of the resulting nanotube parameters can be seen in Appendix E.

Several results listed in Tables 4.1 & E.1 are worth noting. First, the absorption linewidths for both resonances are consistent with those of Bachilo, et al., finding the average linewidth for the E_{11} transition to be ~ 25 meV and for the E_{22} transition to be in the range 50 – 100 meV [42]. Second, the extracted linewidths for the E_{22} transitions are 2 – 3 times those of the E_{11} transitions consistent with the much shorter lifetimes observed for the E_{22} states [152].

In terms of the pump-probe measurements analyzed here the 650 nm pump (16 – 20 nm full width at half maximum (FWHM)) primarily drives the E_{22} transition of the (7, 5) tubes but should also weakly couple with the E_{22} transition of the (7, 6) tubes. On the other hand

the probe, with center wavelengths in the range ~ 1020 – 1060 nm (22 – 28 nm FWHM), is only resonant with the E_{11} transition of the $(7,5)$'s.

Estimating Excited State Absorption

The excited state absorption discussed in Chapter 2 and corresponding to the $E_{11} \rightarrow E_{22}$ transitions can only take place if the probe interacts with the $(7,5)$ or $(7,6)$ nanotubes. That is, since the excited state transitions depend on populating the E_{11} state by first populating the E_{22} state, only the nanotubes excited by the pump need be considered. In Table 4.2 estimates of the excited state transition energies are listed for these two nanotubes. Two possible transitions are listed for consideration. The first transition energy (E_{22} - E_{11}) is for the direct transition from bright E_{11} exciton to bright E_{22} exciton. The second (Δ_{22} - E_{11}) relaxes the assumption that the excited exciton remains in a bound state and instead allows for its excitation into the unbound continuum above the E_{22} exciton at Δ_{22}. The resonant transition energies and corresponding binding energies that comprise the transition energies are also listed in the table for completeness.

The fact that excitation into the continuum above the second excitonic state of the $(7,6)$'s corresponds almost exactly to the probe energy (1.17 eV) is encouraging but also possibly misleading. Calculations of the E_{11} exciton binding energies involved the analytical approximation

$$E_b = \frac{1}{d}\left(A + \frac{B}{d} + C\xi + D\xi^2\right) \tag{4.1}$$

of Capaz, et al. [153]. Here the nanotube diameter is d (nm) and $\xi = (-1)^{\nu}(\cos 3\theta)/d$ with $\nu = (n-m)\mathrm{mod}3$ encodes the influence of the chirality on the binding energy. Capaz determined that for the effective dielectric $\varepsilon = 1.846$ (vacuum) the binding energies can be best fit if $A = 0.6724$ eV nm, $B = -4.910 \times 10^{-2}$ eV nm^2, $C = 4.577 \times 10^{-2}$ eV nm^2, and $D = -8.325 \times 10^{-3}$ eV nm^3. To determine the E_{22} exciton binding energies the model has to be extended somewhat. Perebeinos, et al., determined that $E_{b2} = E_{b1}\left({}^{m_1}/_{m_2}\right)^{\alpha-1}$

where m_1 and m_2 are the effective masses from their respective bands and $\alpha = 1.40$ is an empirically determined parameter [60]. The effective masses in this case are derived by the authors to be

$$\begin{aligned} m_1 &= \frac{\hbar^2 \Delta_{11}}{3a^2 t^2} \left(1 + \nu \frac{\Delta_{11}}{2t}\right)^{-1} \\ m_2 &= \frac{\hbar^2 \Delta_{22}}{3a^2 t^2} \left(1 - \nu \frac{\Delta_{22}}{2t}\right)^{-1} \end{aligned} \tag{4.2}$$

where Δ_{ii} are the free-carrier band gaps, ν as given above, a the graphene lattice constant and $t = 3.0\,\text{eV}$ is inherited from Perebeinos' underlying assumption of the tight-binding Hamiltonian. In Table 4.2 the binding energies were calculated using the free-carrier band gaps derived from interband optical matrix elements developed by Malic & Knorr using a density matrix formalism applied to the tight-binding model [30]. These values then had to be modified to reflect the local dielectric environment after the dependence $E_b \propto \varepsilon^{-\beta}$ derived by Perebeinos, et al., [60] as noted in Chapter 2. For the effective dielectric I assumed only that $\varepsilon_{eff} \approx 3.049$ after observations by Capaz, et al. [154], that found this value was the best fit for a "polymeric matrix." In other words, while the overlap of the probe energy with the calculated transition energies of Table 4.2 is amazing, the calculations are just approximate. To verify the second transition energy results a two-photon excitation measurement after Wang, et al. [45], would be necessary. The importance of this overlap, however, will be revisited in Chapter 5 when excited state absorption is seen as an important component of the pump-probe signal.

Photoluminescence Excitation

An attempt was made to generate a photoluminescence excitation map from the samples studied in order to validate the assignments derived from the absorption measurements. Unfortunately, the thin films created for the differential transmission measurements also had, by design, a fairly low nanotube density. The resulting low nanotube count compounded by the low intensity of the narrow excitation bandwidth and small illumination field resulted

Table 4.2: Lowest binding and transition energies for $(7,5)$ and $(7,6)$ nanotubes. The 650 nm pump (1.91 eV) selectively excites these tubes only. E_{ii} values are from the absorption data listed in Table 4.1. Binding energies $E_{11,b}$ are approximated from Equation 4.1 and extended to $E_{22,b}$ by approximations described by Equation 4.2. The underlying interband transition energies, Δ_{ii} used in the binding energy calculations, are derived from the tight-binding dispersion relations described in Chapter 2. Note that the (1062 nm) probe energy is 1.17eV. See text for discussion.

Chirality	E_{11} Resonances		E_{22} Resonances		Transition Energies	
(n,m)	E_{11}(eV)	$E_{11,b}$ (meV)	E_{22}(eV)	$E_{22,b}$ (meV)	E_{22} - E_{11}(eV)	Δ_{22} - E_{11}(eV)
$(7,5)$	1.18	355	1.91	503	0.73	1.23
$(7,6)$	1.09	316	1.87	398	0.78	1.18

in a signal that was too weak to measure with available equipment. To generate a PLE map a new sample was cooked up by Jeramy Zimmerman using Celia Cunningham's lab notes to reproduce the sample blend as best as possible. A PLE map was then taken on this new blend in solution and can be seen in Figure 4.3. Both the excitation and photoluminescence ranges were restricted to focus on the neighborhood of interest in the differential transmission (DT) measurements and to reduce the acquisition time. The chiralities of the prominent peaks (blobs really) were easy to identify by their relative positions and by comparing their values to the empirically derived values published by Weisman, et al., [40]. The excitation wavelengths, however, differ from the expected wavelengths by a ~ 50 nm blue shift suggesting a significant underlying calibration issue. The stronger peaks against the dark blue background indicate that the sample is dominated by individual nanotubes made up of mostly $(6,5)$, $(7,5)$, $(7,6)$, and $(8,4)$ tubes. Weaker blobs indicate the presence of small populations of $(9,4)$, $(8,6)$, $(8,3)$, and $(10,2)$ tubes as well as an unknown identified only by the tag "$(?,?)$" with an E_{11} emission ~ 50 nm longer than the $(6,5)$ emission. From the absorption measurement (See Section 4.1) we also know that plenty of additional nanotube chiralities are present in the sample but do not appear in the PLE map simply because their $(E_{11}(\lambda), E_{22}(\lambda))$ coordinates are outside the measured range.

The weak peak with the "$(?,?)$" tag is an indication that the sample is not entirely

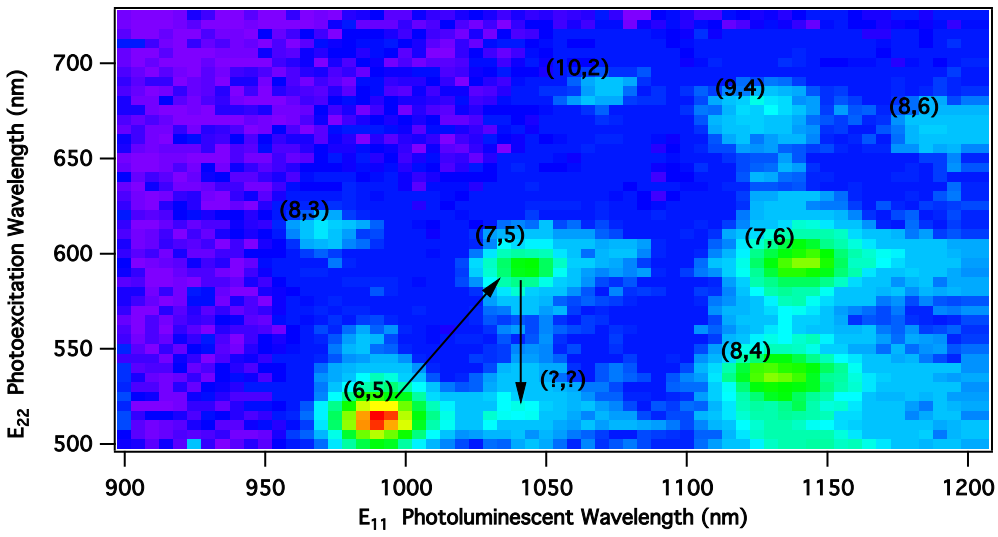

Figure 4.3: Photoluminescence excitation map of a PFO/CNT blend. PLE of polymer/nanotube blend in solution is based on the samples discussed in Chapter 5. Chiralities are assigned by relative positions and comparison with empirical data from Weisman, et al., [40]. The chirality tagged with "(?, ?)" does not exist and likely appears through indirect excitation (see text). Excitation wavelengths differ from expected values by ~50 nm. Blend and measurement provided by Jeramy Zimmerman.

bundle free. A nanotube species does not exist with this relative resonance peak (even after a 50 nm correction) but its appearance can be explained by residual bundling. The arrows indicate one likely path within an unquenched bundle beginning with the excitation of $(6, 5)$ nanotubes to the E_{22} state, followed by the transfer of excitons to lower bandgap $(7, 5)$ nanotubes, and then relaxation to bright E_{11} excitons before they radiatively decay. Charge transfer of this sort has been observed in under 10 fs though the efficiency was highly dependent on the individual bundles measured [155].

It should be noted that even without the unfortunate 50 nm mystery shift the PLE map of Figure 4.3 could not be relied upon to accurately determine the resonant energies of the nanotubes in the final sample. The transition from solution to thin films involves crystallization of the matrix polymer and evaporation of solvent both of which have a direct impact on the local dielectric environment and thus the band structure.

The reproducibility from sample to sample is a challenge in its own right. Thin poly-

mer/nanotube films are made by removing a small drop of the supernatant from the centrifuged solution requiring admirable laboratory skills to realistically reproduce a sample blend from drop to drop. Add to this local variations in the crystallization of the polymer and the finished products are more likely than not to vary from film to film. The only way to be sure one has an accurate characterization of a sample is if that specific sample has been characterized.

4.2 Ultrafast Spectroscopy

The absorption and fluorescence measurements discussed above provide us with a detailed look at a few of the fundamental energy levels that CNTs exhibit. Recalling Figure 2.8, however, the evolution from excitation to radiative relaxation leaves many other transitions and the efficiency with which they take place wholly unaccounted for. The multiple paths excitons can follow through inter- and intra-band transitions can also take place both simultaneously and very rapidly — recall that the lifetimes of many of these excited states are on the order of a few hundred femtoseconds. Observing changes in the electronic states of carbon nanotubes therefore requires femtosecond to picosecond scale, "ultrafast," measurements and a way to isolate specific relaxation paths. In the laboratory this means exciting (aka pumping) and measuring (often probing) the electronic transitions of interest using laser pulses with pulsewidths that are, whenever possible, shorter than the transition lifetimes. Figure 4.4 depicts the most general idea behind these pump-probe experiments: A pump pulse first excites the sample in question; A short time later a probe pulse passes through the sample. Any change in the transmitted probe's intensity between the unpumped and pumped cases, becomes a proxy for changes in the absorption by the sample. As the delay, Δt, between pump and probe increases the effect on the probe diminishes with the sample returning to the ground state.

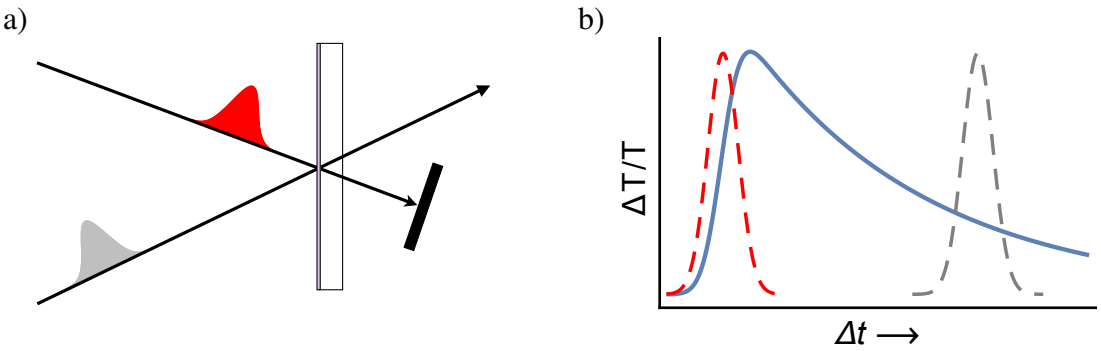

Figure 4.4: Pump – probe measurement in transmission. a) Two beams intersect passing through a thin film. The pump (red) first prepares the sample in the desired excited state. The probe (gray), arriving Δt later, is modified by its pump-dependent transmission. b) Typical differential transmission profile showing a pump-induced transmission that increases rapidly with the arrival of the pump pulse, fixed in time, then decays with increasing time as measured by the transmission of the probe pulse at progressively larger delay times.

Time Dependent Differential Transmission

The self-normalized differential transmission spectrum of Figure 4.4 is described by

$$\Delta T/T = \frac{T(\omega,t) - T_o}{T_o} \tag{4.3}$$

representing the fractional change in the transmitted intensity over time. Here $T_o = T(\omega, t^-)$ refers to the transmission of the probe through the sample in the absence of a pump, i.e. at negative times as $t^- \to -\infty$, relative to the arrival of the pump. The transmission itself is typically described in terms of the normalized intensity $T(\omega,t) = I(\omega,t)/I_o$ where I_o is the intensity incident on the material being tested.

In general we can assume the Beer-Lambert law to describe the amplitude of the intensity as it passes through a uniform material with finite thickness z and absorption coefficient α giving $I(z) = I_o e^{-\alpha z}$. For discrete absorbers like carbon nanotubes distributed in a transparent polymer film this will also be density dependent with nanotube density ρ. If the polymer/nanotube film is illuminated with spot size A and field polarized along $\hat{k}$ the transmitted intensity becomes

$$I(z) = I_o e^{-\left(A \int \vec{\rho} \cdot \hat{k}\, d\Omega\right) \alpha\, z} \tag{4.4}$$

where $\alpha = \alpha(\omega, t)$ is now a nanotube specific absorption coefficient for light oriented parallel to the tube axis. The nanotube density $\vec{\rho} = \vec{\rho}(\Omega)$ has been written as a vector to account for the random orientations of dispersed CNTs. The projection of the field polarization onto the randomly oriented nanotubes accounts for the large depolarization effect [156] this has on the net absorption. Also note that aside from the absorption all of the contributions from the sample (nanotube density, orientation, film uniformity and thickness, etc.) are constant.

For the 100 nm films with a low density of dispersed nanotubes studied in this research the exponents will be quite small. Taking advantage of a Taylor expansion of the exponent the DT is proportional to the change in absorption

$$\Delta T/T(\omega, \tau) = e^{-\left(A \int \vec{\rho} \cdot \hat{k}\, d\Omega\right)(\alpha_p - \alpha_o) z} - 1 \propto -\left(\alpha_p(\omega, \tau) - \alpha_o\right) \tag{4.5}$$

where $\alpha_p(\omega, \tau)$ is the nanotube absorption at time delay τ after the pump and $\alpha_o = \alpha(\omega, t^-)$ is the absorption seen by the probe in the absence of a pump. The key idea here being that the differential transmission relates directly to dynamical changes in the absorption of the CNTs. This relation can also be extended to state populations [30] as

$$\Delta T/T(\omega, \tau) \propto \rho_p(\tau) - \rho\left(t^-\right) \tag{4.6}$$

If the carbon nanotubes are now pumped at a resonant frequency a transient exciton population is generated that fundamentally alters the corresponding absorption through phase-space filling. As the excitons relax back to equilibrium absorption by the nanotubes will evolve concurrently.

Comparing the theoretical description of α or ρ with differential absorption or transmission measurements on CNTs allows us to confirm (or question) our understanding of

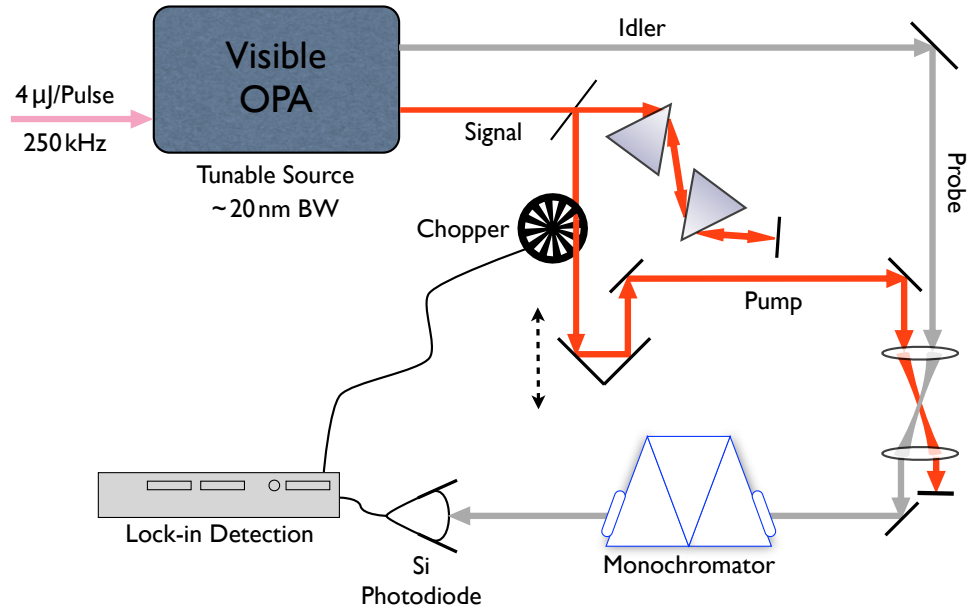

Figure 4.5: Two-color pump-probe layout. The OPA signal (red) is recompressed and acts as the pump. The signal is modulated by a chopper before passing through a delay stage. The stage determines the time delay Δt between pump and probe. The OPA idler (gray) acts as the probe. It is filtered through a monochromator before generating a photocurrent in the photodiode. Finally the DT signal is filtered from the background through lock-in detection.

the nanotube's fundamental electronic properties.

Pump – Probe Measurements

Figure 4.5 depicts the essential components of the pump-probe experimental setup used in my research. A visible optical parametric amplifier (OPA) is pumped by nearly transform limited pulses, with ~ 55 fs pulsewidths, produced by a regenerative amplifier (regen). The high fluence of the amplifier pulses are necessary for the parametric conversion in the OPA and help compensate for inevitable losses in the experimental setup. The 250 kHz pulse train is centered around 800 nm and is used to generate a white light seed and a frequency doubled pump. The parametric amplification of the white light seed then generates two ultrafast pulse trains, a tunable visible "signal" and corresponding near-IR "idler" that become the pump and probe, respectively.

After the OPA the two prisms in the signal path represent a folded prism compres-

sor [157]. The compressor compensates the material dispersion acquired by the signal passing through the OPA. With optimized compression the signal pulsewidth is typically ~ 80 fs while the uncompressed idler is estimated at ~ 120 fs — the longer idler pulsewidth puts a lower limit on the temporal resolution of the data but could be similarly recompressed if higher resolution were needed. The signal is then reflected through a delay stage that varies the optical pathlength of the beam. Varying the pathlength changes the relative time delay between the arrival of the pump and probe pulses at the sample. At a minimum of 1 μm per step the delay stage can alter the time delay by as little as 6 fs. The pump and probe are then tightly focused co-concentrically through the sample which, in this case, is one of the CNT/polymer films. As the delay between pump and probe increases the probe measures the temporal evolution of the sample state after its excitation by the pump.

The last step in Figure 4.5 is the tunable detection of the phase modulated differential transmission. At this point the transmitted probe is first spectrally filtered through a monochromator. For broadband, wavelength dependent DT scans the monochromator can be used to scan across the full spectrum of the probe or select the wavelength of a particular transition. The spectrally filtered light is then focused onto a silicon photodiode with a responsivity just far enough into the near infrared (350 – 1100 nm) to measure the idler spectra of this research.

The signal from the photodiode is then sent to a lock-in detector. By modulating the pump (in this case with a beam chopper running at a fixed frequency) the photocurrent generated by the probe will vary with the modulation frequency by a factor proportional to $\Delta\alpha$ (Equation 4.5). The phase sensitive detection of the lock-in allows us to measure minute changes in the absorption by filtering the photocurrent signal at the chopping frequency.

Non-Degenerate Pump – Probe on CNT Ensembles

Many pump-probe experiments are carried out with both pulse trains tuned to the same wavelength — often referred to as degenerate pump-probe — with the two pulse trains

simply split from a common source. Often it is more interesting to follow the dynamics of one transition as it evolves in response to a different excitation energy. This will mean pumping at one wavelength and probing at another — in this case a non-degenerate pump-probe measurement as depicted in Figure 4.5. Two-color time domain spectroscopy of a distribution of carbon nanotubes, as in the nanotube/polymer blends studied here, is motivated by the PLE spectra of CNTs shown in Figures 3.5 & 4.3. Isolating the response of a particular chiral species can be accomplished by pumping its E_{22} transition and probing at the energy of its E_{11} transition. Since the combination of the two transition energies is effectively unique the ultrafast dynamics of a particular chirality can be observed despite the presence of many other nanotube species in the same polymer.

Quite a few of the ultrafast dynamics studies on CNTs emphasize results focused on $(6,5)$ tubes only [158, 159, 160, 161, 129, 162, 100, 163]. These nanotubes have two distinct advantages over the other chiralities. First, creating nanotubes using the CoMoCAT process generates a majority of $(6,5)$ CNTs. The resulting nanotube distributions can contain 40% $(6,5)$ tubes significantly increasing the signal from this chirality over any others [164]. And second, from Figures 3.5 & 4.3 we can see that these tubes are spectrally more isolated from their neighbors than the others. This unique nanotube species approach is helpful if the researcher is focused on the properties of a single chirality. But the selective approach is not representative of multi-chiral devices like the Arnold device [16]. For such devices, designed to take advantage of broad distributions of CNT's and their corresponding sensitivity to a broad spectrum of light, this strategy will not help us understand how multiple chiralities can simultaneously contribute to the overall performance. Part of the motivation for using an OPA in this research was to be able to target as many different nanotubes as possible, not just the $(6,5)$'s.

The non-degenerate measurements in this dissertation used the signal and idler from the OPA as the respective pump and probe. Conservation of energy restricts the two output frequencies to the relation $\hbar\left(2\omega_{regen}\right) = \hbar\omega_{signal} + \hbar\omega_{idler}$. Figure 4.6 depicts the correlation

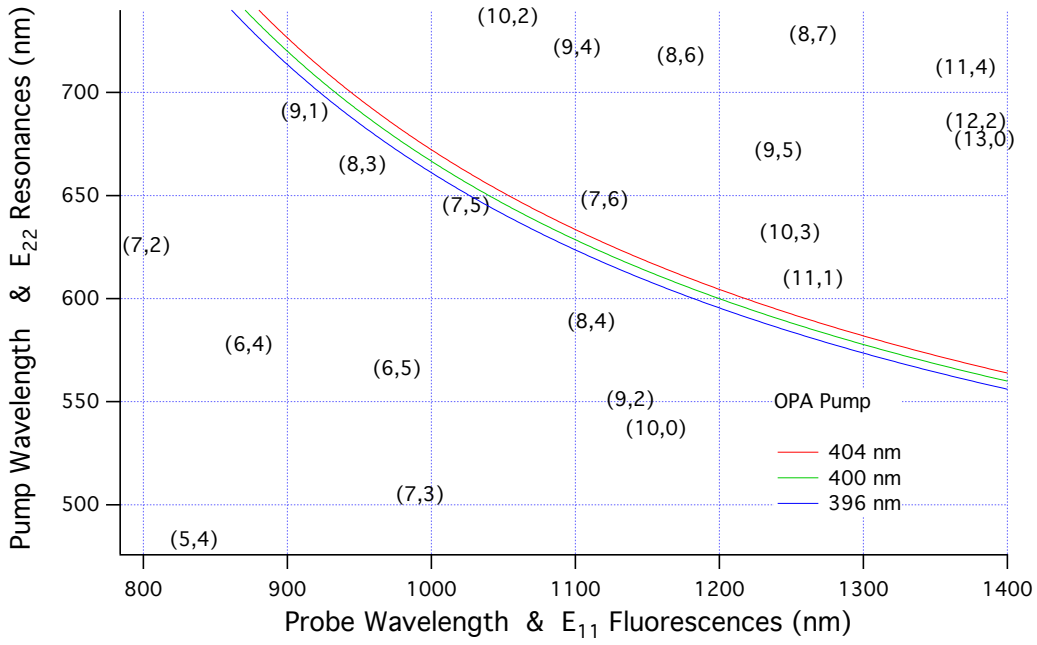

Figure 4.6: OPA range with PLE data. Signal and idler vs the absorption and fluorescence of (n,m) chiral tubes. Colored traces follow the relation between the signal (pump) and idler (probe) generated by the OPA. Multiple traces acknowledge variation from the regenerative amplifier pumping the OPA. (n,m) chiralities are located by their E_{22} absorption and E_{11} fluorescence. PLE data is reproduced from Weisman, et al. [40].

between the signal and idler together with a PLE-like map of the nanotube resonances in the same spectral region. The three curves in the figure are included to call attention to variations in the signal and idler due to observed changes over time in the center wavelength of the regeneratively amplified source.

The proximity of the curves to the $(7,5)$'s, $(7,6)$'s and possibly the $(8,3)$'s or $(8,4)$'s suggest that these nanotubes can be easily targeted by my experimental setup. Note, however, that the (E_{11}, E_{22}) coordinates depicted in Figure 4.6 were determined by Weisman, et al. [40] for surfactant suspended nanotubes. Their results do not guarantee the presence of any particular chirality after dispersion in a polymer. Their values will also differ from the coordinates seen in my samples. Despite this the measured resonances for my CNT/polymer blends (refer to Table 4.1) were consistent with targeting the E_{22} and E_{11} resonances of the $(7,5)$ and $(7,6)$ nanotubes. With the signal and idler tuned to these respective resonances pump – probe experiments can isolate the relaxation dynamics of these

particular nanotubes. In Chapter 5 I will discuss non-degenerate pump – probe measurements of this sort on both $(7,5)$ and $(7,6)$ nanotubes. In the context of the energy ladder for CNTs and its many sub-bands described in Section 2.5 the measurements will help unravel the relaxation cascade that takes place after excitation.

4.3 Energy Density and the Nanotube Environment

Special care must be taken when ultrafast measurements are taken on polymer/nanotube films. The unique character of carbon nanotubes as long, thread-like molecules, for example, results in their chaotic distribution and orientation within the host polymer. Given the sensitivity of nanotubes to the depolarization effect pump and probe polarization cannot be ignored.

The unique data that is the focus of my research also shows a sensitive and significant dependence on the fluences of both the pump and probe. As a result it is important to consider some of the typical power-dependent responses nanotube/polymer films may exhibit. In particular these include photo-damage and saturation at higher powers. At low powers we can expect the onset of both exciton-exciton annihilation and excited state absorption.

Diffusion Driven Depolarization

The ease with which excitons can diffuse along CNTs, added to the exceptional lengths these nanotubes can reach, leads to a curious twist in any polarization dependent ultrafast measurement. Once generated an exciton is free to travel — a process that is exacerbated by scattering from a dense population of excitons — and could then rapidly travel outside the region being probed. This potential problem is mostly avoided by pumping a much larger region than is accessed by the probe balancing outflow with inflow. However, with CNTs randomly mixed like floppy threads in a polymer, this diffusion leads to what appears to be an additional relaxation channel. Excitons that have diffused to a nanotube region

that is perpendicular to the probe polarization will no longer be susceptible to excited state absorption. As a result of this diffusion Korovyanko, et al., observed that the relaxation will see an accelerated, polarization-dependent relaxation representing only the redistribution of the excitons [97]. This behavior is directly analogous to the rapid rotations that take place in solution when the interaction of the probe with some molecular suspension is polarization sensitive. In order to compensate for this loss of polarization one strategy is to probe the sample at the "magic angle" of $54.7°$, a technique that is particularly relevant to nanotubes suspended in a solvent [165, 166]. The magic angle scheme was not in place for the measurements discussed in this study. As a result the polarization anisotropy in the relaxation measurements is not accounted for. This introduces an underlying monotonic relaxation that manifests itself as a small increase in all of the transition specific relaxation rates measured. Generally it does not effect lifetimes restricted to ground state bleaching.

The crazy loopy nature of nanotubes distributed in a polymer also introduces the possibility of pumping nanotubes perpendicular to their axes. This kind of cross-polarized excitation has been shown to lead to weak excitation of E_{12} or E_{21} transverse excitons [167, 168, 83]. These excitations relax to E_{11} excitons so the process introduces yet another relaxation path. In terms of most time-dependent measurements, however, transverse excitation will have only a tiny influence, rarely seen — cross-polarized pumping has been shown to generate a population of transverse excitons that is at most 10% as much as the corresponding direct E_{22} excitons despite the strong depolarization effect suppressing direct excitation [167].

Null-Effect of a C60 Cap Layer

The original device architecture for Arnold's prototype photodetector included a layer of C60 (Chapter 1). The layer primarily acted as an electron acceptor with excitons efficiently dissociated at the interfaces between the nanotubes and C60. As a preliminary step towards studying the evolution of charge states in a similar device some data was taken on thin films

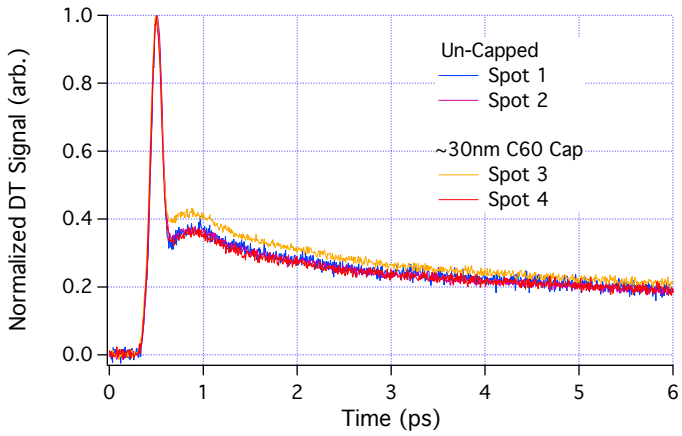

Figure 4.7: Null influence of C60 cap. Comparison of ultra-fast pump-probe scans on regions with and without a C60 cap. Cap thickness was ~30 nm deposited on a ~100 nm nanotube/polymer film. Spot 3 deviation due to sample variation.

similarly capped with ~30 nm of C60. This is specifically relevant to the data presented in this dissertation since much of the data presented here was acquired on C60 capped films.

Comparison of DT scans on polymer/nanotube films with and without a C60 cap was surprisingly boring. Aside from small spot-to-spot variations the results were essentially identical. Figure 4.7 shows four peak-normalized scans on films with and without a C60 cap. All scans show the same relaxation. The slight offset for Spot 3 with the C60 cap was also seen in traces (not shown) for spots in uncapped films. It is not clear why we see such a null result. One hypothesis is that few of the generated excitons could reach the C60 layer given the nanotube's isolation. These were thicker polymer films than Arnold used with the same very limited diffusion length through the polymer itself. Bindl et al., [169] noted in related research that device efficiency would be determined by the effective length scale for exciton migration. Differences in morphology due to process variations may have contributed as well. Regardless of the reasons behind the undifferentiated results I have assumed throughout this dissertation that a distinction cannot be made between data taken on capped or uncapped films. An outstanding problem is to determine why no difference was observed and what structural changes must be made to correct this.

Photo-Oxidation and Vacuum Isolation

Polymer based films are not nearly as robust as traditional bulk semiconducting or metallic materials on which the vast majority of ultrafast pump-probe research has been conducted. As a result, illumination of polymer based samples with focused, laser sourced beams can cause unintended photoprocessing and outright destruction of the sample.

The finished samples described in Section 3.3 had to be isolated in vacuum throughout the experiment to avoid photo-oxidation and any other possible external environmental influences. The challenge with these samples lies in their organic makeup. The photoactive polymers used to disperse and encapsulate the nanotubes are inherently susceptible to oxidation, and worse, photo-oxidation [170] which is certainly enhanced under laser illumination. The result was a rapidly decaying signal and signal data that appeared to vary with time. Early samples were initially stored in weak vacuum packs before being exposed to the air during the measurement process. But once exposed to air during a pump-probe measurement the degradation accelerated rapidly. Figure 4.8 shows the dramatic and irreversible effect of photo-oxidation and processing that can take place on the time scale of a single set of scans.[1]

Since this degradation and loss of signal could actually take place on the order of my scan times the sample had to be protected throughout the measurement — and longer if I were to even hope to take additional measurements on the sample later that day or week. The solution was to enclose the film in a cryostat. While the sample did not need to be cooled, let alone to cryogenic temperatures, the cryostat made it possible to store the sample in a consistently high vacuum — no temperature dependent measurements were ever taken. Initially the samples were loaded into a cryostat inside the nitrogen isolation box in which the slides were processed, completely isolating them from the air. While solving the degradation issue the loading and transportation process was annoying at best and

[1] Oxidation is not limited to the host polymer. Nish, et al. found that this redox process could also quench the fluorescence intensity of the carbon nanotubes [171]. In this case, however, the authors showed that the oxidation process is reversible.

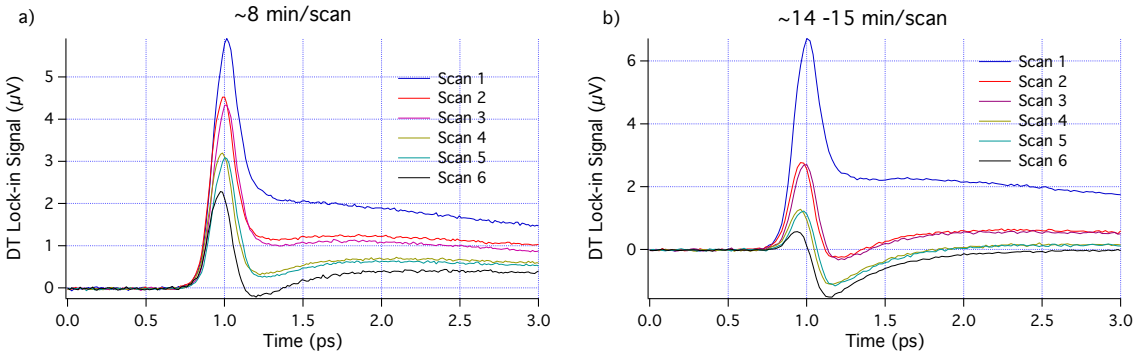

Figure 4.8: Photo-oxidation. Evidence of irreversible damage to P3HT/CNT blend thin film exposed to air during scans. The pump and probe powers were fixed for all scans so variation in DT signal is due to sample degradation only. Both graphs have been clipped to emphasize the more dramatic change in dynamics during the first 2 ps of each scan. a) 10 ps scans ~ 8 min/scan. b) 30 ps scans ~ 14-15 min/scan. Scans were looped forward then backward in delay resulting in the peak-to-peak jitter and what appears to be pairs of scans. Pump: 1.5 mW at 640 nm. Probe: 435 μW at 1080 nm.

conducive of any number of very expensive accidents. It was eventually determined that the samples could be stored temporarily in a pure nitrogen environment until transferred into the cryostat in air then promptly isolated in the cryostat vacuum. The vacuum was maintained at ~ 10^{-4}- 10^{-5} Torr (typically observed around 0.5 x 10^{-5} Torr) through frequent re-pumping. It should be noted, however, that the vacuum level was established by ion gauge using an inherited Varian Multi-Gauge which had not been recalibrated since 1995. As a result the presumed vacuum was only used as a relative value to establish that the vacuum had been consistently maintained. Maintaining the vacuum was sufficient. Once isolated in vacuum the samples appeared to be stable over a month or more.

Indirect Excitation by Host Polymer — Exciton Transfer

In Chapter 3 I noted that the selection of PFO as the host polymer was made to avoid indirectly exciting the CNTs since it has been observed that photo-excited polymers can readily transfer excitons to embedded carbon nanotubes [117, 172]. PFO, with a band edge below ~ 450 nm (See Fig. 3.1), should be largely insensitive to pumping at the red end of the visible and probing out in the near IR. If the polymer underwent two-photon absorption (TPA),

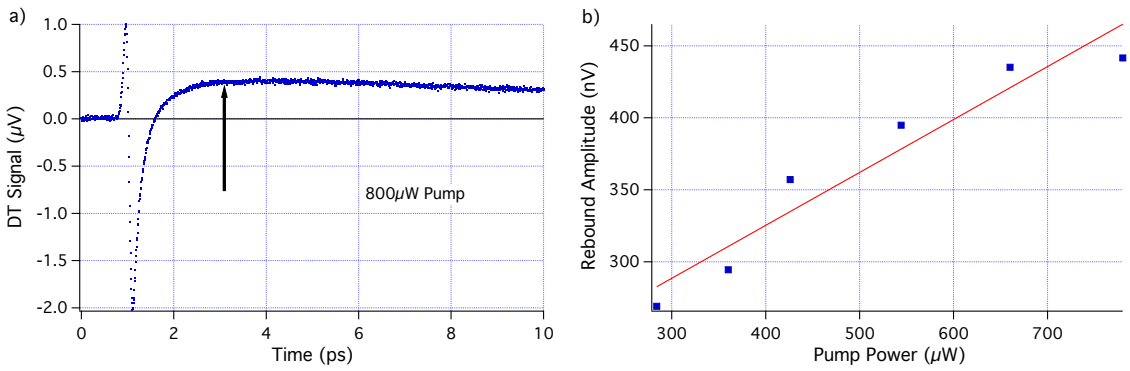

Figure 4.9: Ruling out two-photon absorption. (a) Rebound delay. After ~ 3 ps the DT signal is dominated by the dark exciton and/or trap state populations, independent of pump or excited state absorption dynamics. (b) Plot of DT rebound amplitude vs pump power and linear fit to the graph.

however, indirect excitation of the nanotubes would still be a possibility. Since the pump wavelengths were all in the neighborhood of 650 nm two-photon excitation of the PFO, while near the high energy limit of its absorption range, could not be immediately ruled out[2]. Assuming that the pump is in fact driving TPA in the polymer, the indirect exciton population would follow as the square of the pump power. And the exciton population that then crossed to the embedded CNTs would be directly proportional to this polymer exciton population. As a result the probe would then measure the total population of excitons that would also include a contribution following the statistics of TPA. In practice, since the pump excites the nanotubes directly, the total exciton population should show only a small nonlinear deviation from the expected linear response.

Refuting a TPA contribution (or confirming it) would require measuring the exciton population as a function of pump power. If the dynamical response of the system could be entirely determined by phase-space filling in the $E_G \rightarrow E_{11}$ transition the DT signal would be in direct proportion to the exciton population. Unfortunately, since the data indicate a strong induced absorption as well, this assumption cannot be made. At later delays, however, the majority of the exciton population is expected to pool into the longer lived dark exciton state of the E_{11} manifold or a trap state (recall Section 2.5). The resulting DT

[2]A differential transmission measurement on PFO free of nanotubes gave a null result — suggestive of negligible absorption of any order but not conclusive.

signal would then be entirely due to ground state depletion and directly proportional to the total exciton population. Ignoring, at our peril, the non-linear effects of high initial exciton populations, the DT signal at long delay times is a proxy for the total exciton population.

Figure 4.9 (a) shows qualitatively how the DT amplitude at a long delay time can be independent of the competing effects of induced absorption and photobleaching at earlier delays. The figure also demonstrates that after 2 – 3 ps the relaxation is dominated by a long slow decay with a lifetime that is 10's to 100's of picoseconds — a signature of dark and/or trap state excitons. In Chapter 5 we will see that all the relevant data sets evolve into a long lived positive signal in a manner independent of pump power. From this perspective the differential transmission at long delay vs pump power can be used as the proxy for exciton population vs pump power we are looking for.

Figure 4.9 (b) shows the increase in the DT signal versus pump power with a linear fit to the data. Excitation directly proportional to the pump power would be linear whereas excitation due exclusively to TPA would result in a quadratic increase with power. As a result, if the excitation is due to both direct absorption and two-photon absorption of the pump, we would expect a small but non-linear increase in the DT signal with power. Comparison of the data to the linear fit suggests that the data lacks a convincing quadratic component. In fact the data may be increasing sub-linearly suggesting the onset of saturation or that more complicated dynamics are at play. The choice of PFO as the host polymer therefore allows me to ignore the possibility of exciton transfer driving the excited state dynamics of the carbon nanotubes.[3]

Low Power Relaxation and Threshold Behavior

While the isolation of the polymer/CNT blend films in vacuum provided significant protection against photo-oxidation, the samples were still vulnerable to damage from the energy

[3] I have not considered the probe in this scenario since all probe wavelengths are beyond 1 μm and could only excite the polymer through an even less probable three-photon or higher order process.

of the pump and probe beams alone. Measurements on MDMO blended with CNTs showed that even at the relatively low pump power of 400 µW the DT signal would slowly degrade. Luckily, in samples of PFO blended with CNTs pump powers as high as 1.18 mW could be used without noticeable signal decay suggesting no sample destruction — the likely advantage for PFO being that its band edge is significantly higher in energy than the pump so that any energy absorbed would be restricted to the nanotubes.

Staying below the damage threshold, while critical to generating reproducible results, is necessary but not sufficient. Figure 4.10 shows two sets of DT traces at relatively low pump powers on MDMO/CNT-blend films[4]. Both graphs have been normalized to their signal peaks to emphasize the differences in their relaxation behavior. Figure 4.10 (a) shows traces recorded for pump powers of up to 800 µW and shows the curious onset of a trough in the signal at around 270 fs after the pump. Figure 4.10 (b) focuses on pump powers below 400 µW where it can be seen that subtle changes in behavior are already emerging from the simple exponential relaxation of a multi-level system. This deviation from simple relaxation, even at low pump powers, is a strong indication that the system is being driven out of the linear regime.

A number of studies have observed relaxation behavior in carbon nanotubes that deviate from the expected simple relaxation of a multi-level system as a function of power [173, 99, 162]. But the data in Figure 4.8 suggest that non-linear behavior may already contribute significantly at fairly low excitation. This interpretation is supported by observations from Xiao, et al., who observed that for CNTs resonantly pumped at low intensity saturation occurred for only 2 – 6 excitons [90]. Understanding the evolution and source of the trough and its dependence on the pump and probe powers has been the primary focus of this research.

[4]Despite the fact that degradation in the DT signal can be seen at these pump powers for MDMO/CNT-blend films these traces are representative of the general polymer/nanotube behavior vs. pump power. A strong signal-to-noise ratio allowed for rapid acquisition of the data limiting the exposure time and minimizing degradation across these particular data sets.

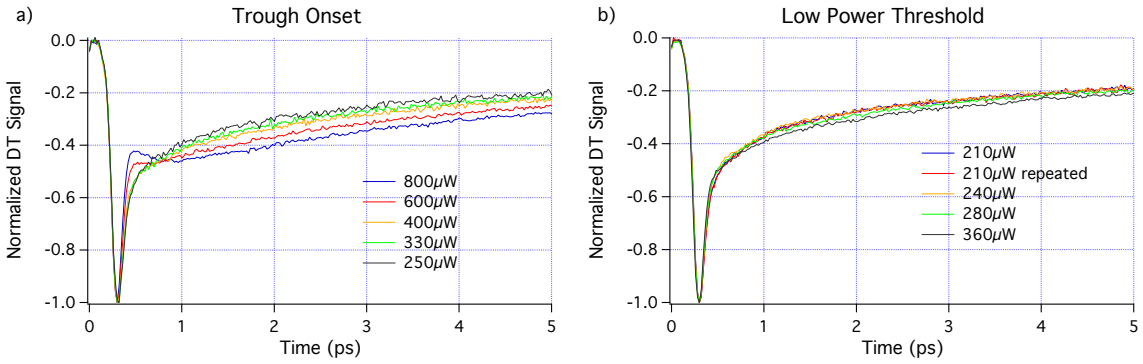

Figure 4.10: Threshold behavior in low power relaxation. Onset of complex behavior in the ultrafast relaxation dynamics of isolated $(7,5)$ single-walled carbon nanotubes at low pump powers. a) Onset of atypical trough contradicting the expected simple exponential relaxation. b) Low-power threshold of complex relaxation. All traces were peak-normalized to emphasize variation in relaxation behavior. Both data sets were measured on a CNT/MDMO-PPV blend film in N_2 isolation.

Saturation

It should be noted here that the onset of the behavior seen in Figure 4.10 is not due to any direct population saturation. Measurements of pump fluence driving CNTs have found that the onset of saturation occurs around $\sim 2 \times 10^{15}$ photons/pulse cm^2 as measured by peak induced transmission [163]. At lower fluences on the order of $\sim 10^{12} - 10^{14}$, evidence is already seen for high exciton densities leading to the nonlinear behavior attributed to Auger-like exciton-exciton annihilation [112, 47, 174]. These values are worth noting since my measurements involved pump photon densities ranging from $3 - 9 \times 10^{14}$ photons/pulse cm^2 and probe densities ranging from $4 \times 10^{14} - 2 \times 10^{15}$ photons/pulse cm^2. Since both the pump and probe densities are above 10^{12} photons/pulse cm^2 any assumptions on ultrafast relaxation have to take into account contributions from exciton-exciton annihilation. On the other hand, although the photon density of the probe reaches the onset of saturation at the highest powers, most of the pump and probe powers translate to densities that are below this threshold. The potential for saturation will be revisited in Section 5.3 when rate equations are proposed to describe the dynamical response of optically excited nanotubes.

4.4 Summary

Ultrafast pump-probe spectroscopy is an extremely sensitive technique for measuring the rapid evolution of excited states in carbon nanotubes. By tuning the pump and probe wavelengths of a time domain scan to predetermined E_{22} and E_{11} transition energies the relaxation dynamics of a specific nanotube species can be isolated and followed. Selection of a specific chirality in an ensemble of CNTs, however, requires an accurate map of the resonant transitions. This can be determined by fitting a series of Voigt (or more practically, Gaussian) profiles to the broad absorption profile of a polymer/nanotube blend. Identification of the first two bright excitons of a particular nanotube chirality can be further verified with the help of photoluminescence excitation. A bright PLE measurement has the concurrent advantage of verifying that the nanotubes have been thoroughly dispersed with most bundles stripped from the blend.

Before examining the ultrafast relaxation data over a range of pump and probe powers it was necessary to identify some of the limitations involved in testing these films. Most importantly, perhaps, was the susceptibility to damage from the pump and probe pulses themselves. Damage due to photo-oxidation necessitated isolating the films from the environment in high vacuum where even seemingly low powers were found to cause progressive damage in polymers other than PFO. The potential for saturation also had to be considered since the pulse fluences used in this research pushed the limits of linear excitation. This limiting behavior, however, and the unusually high probe fluences have led to some striking behavior in the excited state dynamics, hinted at in figures 4.9 & 4.10, that will be the focus of Chapter 5.

With the pump and probe tuned to the transition energies of a specific nanotube the temporal evolution of the excited states of a CNT can be followed as the system returns to its ground state. As states are variously depleted or populated changes in absorption by the nanotubes will be reflected in changes in the differential transmission. For pulses on the order of 100 fs and time steps that can be as short as 6 fs the typical pump-probe

setup described above allows us to measure very rapid changes in the electronic states of a nanotube. In the following chapter the evolution will be used to unwrap the excited state dynamics of CNTs under changing power scenarios. But there is a twist. Despite carefully extracting the resonant transitions of nanotubes in my samples the tuning constraints of the OPA and the broadband nature of ultrafast pulses limit my ability to selectively target specific chiralities. Because of this we will see in the following chapter that both the $(7, 5)$ and $(7, 6)$ nanotubes have to be considered.

CHAPTER 5

Excitation, Relaxation and Scattering Dynamics

The pump-probe experiment described in Chapter 4 was expected to yield straight-forward relaxation lifetimes. These were to have been used to simply validate the experimental setup. Then the same measurements were to have been applied to a solar cell design much like the device prototype developed by the Forrest group (Chapter 1). Such a measurement strategy was sheer elegance in its simplicity.[1] Ultrafast measurements, however, come with advantages and disadvantages in that they are both spectrally broadband and, of course, take place on very short time scales. This can and does result in measurements that record multiple transitions. The broadband pulses may, for example, spectrally overlap several resonances at once. And on ultrafast time scales intermediate excited states are often susceptible to secondary pumping or probing pulses. In the spectrally congested region of the dispersed nanotubes being targeted this is particularly relevant. I have already shown in Section 4.1, for example, that even with a two-color pump and probe strategy my measurements may interrogate both the $(7, 5)$ and $(7, 6)$ nanotubes. In the same section I also noted that the probe could easily be in resonance with one or more of the excited state transitions of these tubes.

In what follows I will explore the very non-monotonic differential transmission (DT) patterns excitons in nanotubes can exhibit and how my ultrafast non-degenerate pump-probe experiments revealed far more complex behavior than expected. In an attempt to

[1] With apologies to the writers and villains of *The Middleman* [175].

quantify this behavior a relaxation model will be proposed. Based on our existing understanding of excited state dynamics in carbon nanotubes (CNTs) a system of rate equations will be proposed and fit to the data across a series of results covering variations in both pump and probe power. This model of relaxation as a cascade down discrete energy levels meets with some success in quantifying the dynamics of a two-chiral system. But we will see that the model cannot completely describe the unusual relaxation behavior in the data and an alternative explanation is needed.

The most likely interpretation of our missing dynamics is the coherent interaction of the nanotube system with the pump and probe fields. Evidence for coherent interaction can be seen both in the dependence of the population on the field strength and in calculations of the pulse areas relative to the nanotube resonances. In order to understand the impact of coherent interaction on the relaxation data a density matrix approach will be considered that adds depth to our general understanding of nanotube dynamics.

5.1 Competing Dynamics in PFO/CNT Relaxation

Evidence for distinctly non-monotonic relaxation in my carbon nanotube/polymer blend films can be seen in Figure 5.1. The early and dominant onset of a negative DT signal, i.e. induced absorption, can be clearly seen around 130 femtoseconds after time zero. Around one picosecond later the absorption behavior vanishes as a long lived photo-bleach takes over. Induced absorption in ultrafast DT measurements of CNTs has been seen in many experiments to date. Credit for these absorption signatures has been assigned mostly to inter- [84, 97, 78] and intra-exciton transitions [46, 99, 100, 75] as well as bi-exciton formation [89, 85, 94] and Hydrogen-like excited exciton states [99, 100] including exciton ionization [67]. But in all of these experiments none of them observed the dramatic double crossing behavior seen in the DT signal of Figure 5.1 suggesting a multistage process that has not been fully accounted for.

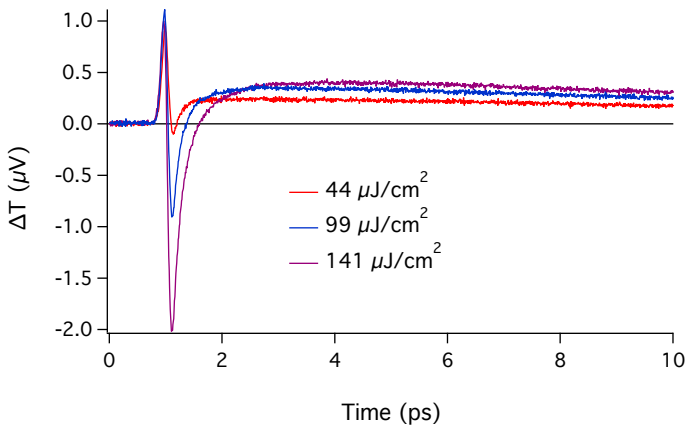

Figure 5.1: Transient photo-induced absorption. Ultrafast relaxation of CNT/PFO blend showing short-lived photo-induced absorption and extended recovery of long-lived dark state. Pump pulses were centered at 650 nm (1.91 eV). Probe pulses were centered at 1062 nm (1.17eV) and fixed at ~ 43 μJ/cm^2. Data has not been normalized (See text).

Background absorption We don't have to fully understand these results to make some reasonable assumptions about this dynamic relaxation based on previous results in the literature. Below I will revisit these observations with quantitative models in an attempt to confirm or refute them. Let me first rule out contributions from anything other than the carbon nanotubes themselves. In Chapter 3 I described the general method of dispersing carbon nanotubes in a surfactant or polymer. Once dispersed differential transmission experiments could be reliably designed to focus on nanotubes of a single chirality. Despite these methods of purification and separation the process is not perfect and linear absorption spectra will show a broad background for these samples (See Figures 3.2 & 3.4). By pumping residual contaminants and tubes that are only indirectly probed we have to expect at least a small contribution from this junk will creep into our differential transmission measurements. Fortunately, by comparing the first excited state kinetics of (6, 5) tubes with fluorescence up-conversion measurements — when pumped along either the E_{22} or E_{11} resonances — background contributions have been determined to be negligible [89]. Thus any dominant dynamical response seen in a DT measurement on dispersed carbon nanotubes can be attributed to the nanotubes themselves.

The long tail Working backwards, consider the decay at long delay times. After the DT trace returns to positive we can see a long slow decay consistent with the stable dark excitonic state. The long lifetime is expected since relaxation from a dark state to the ground state is a dipole forbidden transition. Published observations put the lifetimes for this dark state at 20 to 200 ps [76] providing a rather large sample-dependent acceptance window for the apparent 20 – 30 ps lifetimes seen in these traces. Since the probe doesn't couple directly to the dipole forbidden dark state this tail is a signature of ground state depletion impeding absorption of the probe.

The negative trough Next, consider the short-lived negative DT signal. In Table 4.2 I showed that the $E_{11} \rightarrow E_{22}$ transition energies for the $(7,5)$ and $(7,6)$ tubes where consistent with the probe energy. The negative DT signal therefore suggests that for about 1 ps there is a large enough population of bright E_{11} excitons that the probe can be efficiently and dominantly absorbed through the excited state transition. It should be noted that many of the induced absorption signatures identified in the literature can be ruled out in this case as representing transitions with energies that differ significantly from the probe used in this experiment. All of the intraband transitions, for example, are out in the infrared and terahertz regions [46, 99, 100, 75] while excited state transitions to higher energy excitons, E_{33} and beyond, require energies much greater than the probe [97, 78]. In this experiment, however, the broadband probe $\approx E_{22} - E_{11}$ and covers multiple possible excited state interband transitions for the $(7,5)$ and $(7,6)$ nanotubes. The overlap allows for excited state absorption of the probe as E_{11} excitons are re-excited into the E_{22} manifold leading to the negative DT component in the total signal. Induced photo-absorption would then be directly dependent on the transient population of the bright E_{11} excitons. As soon as a sizable percentage of bright E_{11} excitons has decayed to the ground state or drained into the dark excitonic states the contribution from induced photo-absorption can no longer dominate — any remaining negative DT signal would be overwhelmed by the ground state

bleaching due to the long-lived dark excitons that remain.

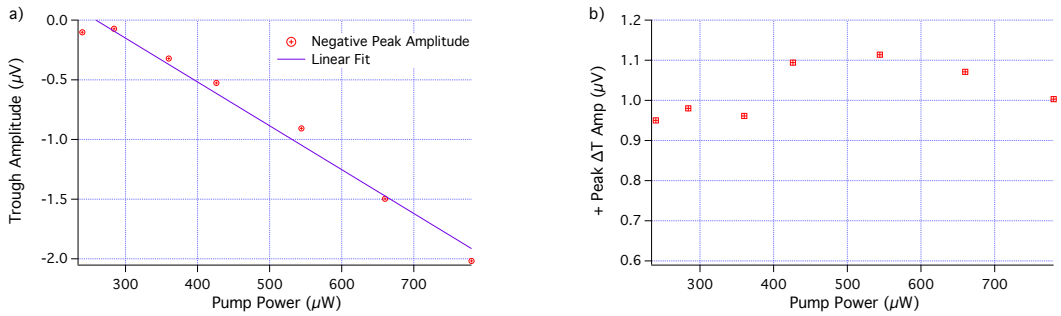

Figure 5.2: Peak amplitudes versus pump power. a) Direct correlation between photo-induced absorption strength and pump power. b) Positive (initial) peak amplitude largely invariant with pump power.

Photo-induced absorption is further supported by the direct correlation between pump power and absorption amplitude seen in Figure 5.2. Since ~ 80% of the E_{22} excitons decay nonradiatively into the E_{11} state [81], and do so on a time scale shorter than the pump pulse, the E_{11} excitons act as an almost immediate proxy for the photo-generated E_{22} excitons. As long as the system remains below saturation the pump will almost directly drive the bright E_{11} population higher facilitating the induced absorption. As a result the photo-induced absorption (PA) amplitude should increase directly with the pump power as observed.

Bi-exciton formation An alternative interpretation of photo-induced absorption considers that in the tightly confined environment of a nanotube the formation of complex multi-particle excitations like bi-excitons is energetically favorable [176]. Estimates from the theory show that bi-excitons would have a binding energy $E_{xx} \approx {}^{0.195\,eV\text{Å}}/_{r}$, where r is the tube radius in Angstroms. This would result in an absorption signature red-shifted roughly 50 meV from the corresponding E_{11} resonance. Observations supporting this theory have been made by one team [89] while subsequent measurements by another lab did not see evidence for this result [94] though their pump fluences (roughly the same as in Fig. 5.1) may have been too low to see this effect. Still more recent measurements attributed their photo-induced absorption to bi-exciton formation in small bundles of nanotubes [85]. Since my measurements were carried out on samples that were processed in

order to eliminate bundling it is unlikely that the rather dominant PA in my results is due to the weak signal from optically induced bi-exciton formation. In addition, all of the measured transition energies corresponding to absorption are around the lower end of the probe energy. Since these transitions are already at the edge of the probe band a 50 meV redshift for bi-exciton formation would mean it was further out of resonance. Nonetheless residual bundles within the polymer/CNT films were not ruled out and cannot be completely discounted. In addition, some of the kinetics observed by Ma, et al. [89] are consistent with the relaxation data shown in Figure 5.1 and will be discussed in more detail below.

The initial positive peak The initial peak in the data also deviates from expected behavior. Since the generation of E_{22} excitons correspondingly depletes the ground state a DT measurement of the probe will show a corresponding increase in transmission. This ground state depletion acts as a proxy for the E_{22} population. Since the initial peak occurs as the E_{22} excitonic state is populated there should be at least some correlation between the population and the pump power. What is seen instead (Figure 5.2) is a nearly constant amplitude for the range of pump powers despite the fact that this data has not been normalized.

Competing dynamics The most likely reason behind the unexpectedly flat amplitude of the first peak is competition between induced transmission and absorption. The initial positive DT, attributed to populating the E_{22} state, is short-lived given its rapid decay. But the rapid decay is also responsible for rapidly populating the E_{11} state. Consequently the induced absorption arising from the excited state transition increases as rapidly as the E_{22} state decays. The data suggest that the induced absorption grows so rapidly that it overwhelms the induced transmission. And increasing the pump power simply increases the strength of both competing processes — any expected increase in the positive peak amplitude with pump power is balanced by, and then overrun by, the increase in absorption.

This competition between temporally overlapping transitions is also likely present throughout the evolution of the induced absorption trough. As the population of E_{11} ex-

citons increases, phase-space filling in the E_{11} transition will lead to higher transmission of the probe. In the absence of excited state absorption then one would expect the $1-3$ ps range of the relaxation traces to be strictly positive. Since both the E_{11} transition and excited state transition depend directly on the E_{11} population they must be present and contribute at the same time. As a result the negative trough seen in Figure 5.1 must be completely masking the expected induced transmission until the E_{11} dark state is sufficiently populated.

5.2 Disrupted Induced Absorption

The dominant induced absorption seen in the data above (Fig. 5.1) appears as a response to the pump power. And yet the pump can only indirectly drive the bright exciton population that underlies the excited state absorption. A more direct measure of this transition and the ground-to-E_{11} transition would be its response to variations in the probe. In Figure 5.3 several traces are shown corresponding to DT scans at a range of probe powers. The lowest amplitude trace corresponds closely with the lowest amplitude trace in Figure 5.1. In contrast, however, the new figure represents changes in the dynamical response of the nanotubes for a fixed pump power as the probe power is increased. These measurements run counter to the traditional notion of a low power probe that only weakly interacts with the system it measures. But the DT scans also add considerably more information about the dynamics of CNTs than would be available if only the pump power were allowed to vary.

Loss of induced absorption signature The differences between relaxation behaviors seen in the two data sets is striking. The only behavior that is consistent between the two sets is the slow relaxation at long delay times. In contrast, the initial positive peak now appears to increase with power. This is not a direct comparison, however, since it is now tracking with the probe power instead of the pump represented in the previous data set.

Instead of measuring an expected increase in the induced absorption response, to which the probe is assumed to couple, the increase in power appears to aggressively counteract the

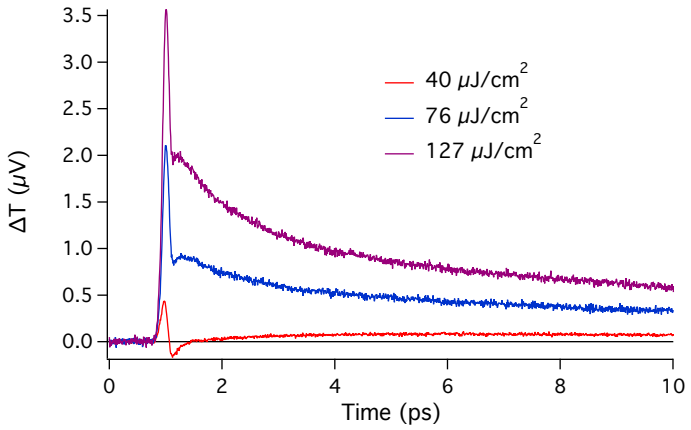

Figure 5.3: Disrupted induced absorption. Ultrafast relaxation of PFO/CNT blend showing the induced absorption trough impeded with increasing probe power. Pump pulses were centered at 650 nm (1.91 eV) and fixed at ~ 40 μJ/cm^2. Probe pulses were centered at 1062 nm (1.17eV). Data has not been normalized (See text).

absorption process. Given the uncharacteristically high power of the probe one possibility is that the excited state transition is simply saturated by the probe. This in turn would allow the weaker (and unsaturated) induced transmission component to increasingly dominate with higher probe power. While the probe powers reach the threshold of observed saturation we will see in the quantitative analysis below that this does not adequately explain the observed relaxation behavior.

5.3 Quantifying CNT Relaxation Dynamics

General observations of the relaxation seen in Figures 5.1 & 5.3 assumed that the CNT energy levels contributing to this behavior can be thought of as discrete and relatively dispersionless. Figure 2.8 illustrated this description as a ladder of excitonic states. The assumption is based on our understanding of the optically excited states of CNTs as tightly bound excitons. Given that the joint density of states approximates van Hove singularities and that the optical matrix elements suppress absorption away from band minima [30] it is reasonable to expect that these transitions have narrowly defined energies. Experimentally we see that the optical properties of CNTs are indeed dominated by their excitonic

states [89] with relatively narrow linewidths (Table E.1). All of which is to say that it is reasonable to consider the excited states of a carbon nanotube as a discrete series of dispersionless energy levels.

The dynamic excitation and relaxation process should therefore be fully quantifiable as a set of coupled differential equations representing these discrete levels. Equations 5.1 represent all of the relevant energy levels of an ensemble of CNTs from excitation of the E_{22} state through return to the ground state. For completeness the equations must also account for the non-linear exciton-exciton annihilation dynamic.

$$\begin{aligned}
n'_{22} &= -r_{22}\,n_{22} + \tfrac{1}{2}\gamma\,n_{11}^2 + A_{12}I_bP_b\,(t-\tau)\,(n_{11}-n_{22}) \\
&\qquad + A_{G2}I_pP_p\,(t)\,(n_G-n_{22}) \\
n'_{11} &= c_{21}\,r_{22}\,n_{22} - r_{11}\,n_{11} - \gamma\,n_{11}^2 - A_{12}I_bP_b\,(t-\tau)\,(n_{11}-n_{22}) \\
&\qquad + A_{G1}I_bP_b\,(t-\tau)\,(n_G-n_{11}) \\
n'_D &= + c_{1D}\,r_{11}\,n_{11} - r_D\,n_D \\
n'_G &= c_{2G}\,r_{22}\,n_{22} + c_{1G}\,r_{11}\,n_{11} + r_D\,n_D + \tfrac{1}{2}\gamma\,n_{11}^2 - A_{G1}I_bP_b\,(t-\tau)\,(n_G-n_{11}) \\
&\qquad - A_{G2}I_pP_p\,(t)\,(n_G-n_{22})
\end{aligned} \tag{5.1}$$

Following the energy level cascade depicted in Figure 2.8 the n_{ii} variables represent the populations of the E_{ii} bright singlet excitons, n_D represents the lowest energy E_{11} dark singlet exciton and n_G the ground state population.[2] Each of the time-dependent variables, $n_s = n_s[t]$, is a relative population with $n_s[t] = \eta_s[t]/N$. Here $\eta_s[t]$ is the number of excitons in a given state s and $N = n_G[t^- \rightarrow -\infty]$ is the total number of excitons that can be generated. In this sense the exciton population is effectively normalized since $\sum n_s = 1$. The three E_{11} dark and weakly dark states (Section 2.4) have been lumped together as n_D. Since the probe can only interact with dark states through ground state depletion there is

[2]Note that n_G represents the relative population of the ground state for the carbon nanotube and should not be confused with the ground state of an exciton as discussed in Section 2.4.

no way to distinguish between the different sublevels in this experiment. As a result the total recovery rate is limited by the combined effect of relaxation through the ladder of dark states.

Similarly the relaxation rates, r_s, of each of the n_s exciton populations represent the effective relaxation rates since the excitons may follow several decay paths. To compensate for this lack of information I have introduced branching coefficients c_{ij} to quantify the fraction of n_i excitons decaying into n_j excitons. Each transition specific rate can then be determined through the branching coefficients since $r_{ij} = c_{ij} r_{ii}$.

Auger-like exciton-exciton annihilation is included in the dynamical equations through the non-linear $\gamma\, n_s^2$ terms. As described earlier exciton-exciton annihilation (EEA) involves the interaction of two excitons in the same state — in this case the E_{11} bright state — where one is annihilated and its energy transfers to the other exciton. This energy is roughly equal to the $E_{11} \rightarrow E_{22}$ transition energy for both the $(7,5)$ and $(7,6)$ tubes so that in these experiments the re-excited excitons repopulate the E_{22} state.

The driving terms $A_{ij}(\omega)\, I\, P(t)$ quantify the coupling of the field to the nanotubes for both the pump (p) and the probe (b) pulses with absorption coefficients $A_{ij}(\omega)$, intensity I and pulse envelope $P\,(t)$. Unlike typical pump-probe experiments with a weakly interacting probe the measurements in this research used probe intensities capable of significantly changing exciton populations. As noted earlier, the probe also overlaps with both the ground, $E_{\mathrm{G}} \rightarrow E_{11}$, and excited state, $E_{11} \rightarrow E_{22}$, transitions. Probe excitations are therefore included for both cases. In both the pump and probe driving terms the intensity term, I , is included separately as a known parameter. It is useful to separate the field intensities since the variations in relaxation behavior are compared/contrasted to their changing values. The frequency dependent absorption coefficients $A_{ij}(\omega)$ account for spectral overlap of the pump or probe with the frequency dependent absorption cross-section of each transition and its oscillator strength. The $A_{ij}(\omega)$ also take into account sample dependent absorption parameters including, for example, nanotube density, chiral distribu-

tion and orientation, and process history (polymer annealing, nanotube lengths, etc. See Chapter 3). For the time delay experiments all of these factors are considered constant so that the combined $A_{ij}(\omega)$ term is constant in turn. The corresponding pulse profiles, $P(t-\tau) = e^{-\frac{(t-\tau)^2}{\Delta^2}}$, are simple gaussian pulses centered at times τ. For the pump fixed in time ($\tau = t_o$) the probe delay relative to the pump will be $\Delta t = \tau - t_o$. The pulsewidth, full-width at half-max (FWHM), then corresponds to its experimentally determined value with $\Delta = \text{FWHM}/2\sqrt{ln\,2}$. Since the pump and probe intensities are on the threshold of driving the system into saturation (See Section 4.3) these driving terms also include the population differences $\Delta n = n_j - n_i$.

In the absence of saturation, non-linear Auger-like exciton-exciton annihilation and excited state absorption this system of equations would represent a simple relaxation problem reducible to a multi-exponential decay. The presence of these driving terms, however, is necessary if we are going to account for the decidedly more complex behavior seen in Figures 5.1 & 5.3.

Differential Transmission with Competing Transitions

The basic form of a differential transmission measurement described in Chapter 4 assumes that the probe interacts with a single transition. The results from the absorption measurements (Table 4.2) and use of a broadband probe, however, have dictated that Equations 5.1 account for at least two transitions interacting with the probe. Extending this observation to calculations of the differential transmission signal in terms of the absorption coefficients of Equations 5.1 the DT amplitude becomes

$$\begin{aligned} \Delta T(t) &= -C(t)\left\{A_{12}\left[n_{11}(t) - n_{22}(t)\right] + A_{G1}\left[n_G(t) - n_{11}(t)\right]\right\} + T' \\ &= C(t)\left\{A_{12}n_{22}(t) + \left[A_{G1} - A_{12}\right]n_{11}(t) - A_{G1}n_G(t)\right\} + T' \end{aligned} \tag{5.2}$$

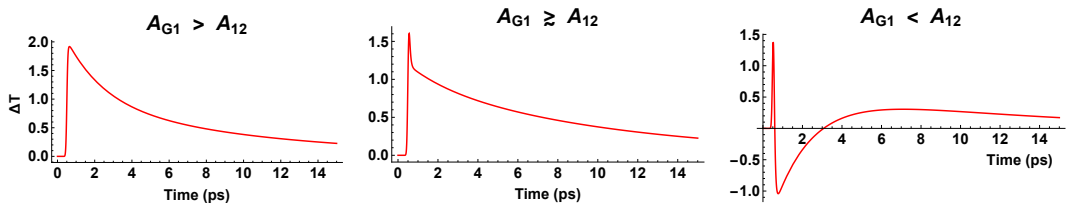

Figure 5.4: Differential transmission with competing transitions. Model differential transmission traces with contributions from both induced transmission and absorption. ΔT decays smoothly when the ground state transition dominates ($A_{G1} > A_{12}$). For roughly balanced contributions ($A_{G1} \sim A_{12}$) a bend appears in ΔT shortly after the peak. When the excited state transition dominates ($A_{12} > A_{G1}$) the bend in ΔT evolves into a kink or deepening trough.

where $C(t) = I_b P_b(t)$ captures the probe intensity (I_b) and pulse envelope $P_b(t)$, while T' just consolidates all constant background terms. Due to the very rapid variation in transmission relative to the probe pulsewidth calculations of ΔT have to be integrated over the full width of the probe in order to realistically capture these changes. For the simplest term representing the background this means the full expression should be

$$T' = A_{G1} I_b \int P_b\left(t - t^-\right) n_G\left(t^-\right) dt \tag{5.3}$$

by assuming $n_{11}(t^-) = 0$ and $n_{11} \ll n_G \; \forall \, t$.

Equation 5.2 was restated on the second line to emphasize the competition that results between the induced transmission for the $E_G \rightarrow E_{11}$ transition and the induced absorption of the $E_{11} \rightarrow E_{22}$ transition. The competition appears in the second term comparing the two absorption coefficients A_{G1} and A_{12}. Figure 5.4 demonstrates how the differential transmission evolves under the competing influence of these transitions. There are three possible regimes. For the case in which induced transmission dominates over induced absorption, i.e. $A_{G1} > A_{12}$, the system will always be positive and relax monotonically. The multi-exponential decay in this case will simply reflect the individual lifetimes of the energy levels. If the contributions are balanced with $A_{G1} \sim A_{12}$ — effectively ignoring the n_{11} contribution — the combined effect will still lead to monotonic relaxation in the DT signal. In this case, however, the contribution from induced absorption can already be seen for $A_{G1} \gtrsim A_{12}$ with the emergence of a kink very early in the relaxation. The early

appearance of this kink is consistent with a rapid increase in the n_{11} population facilitating excited state absorption. Finally, if $A_{12} > A_{G1}$ an increasing n_{11} population will substantially alter the measured transmission since the induced absorption can briefly dominate the DT signal.

Also note that the induced absorption is independent of the background and ground state depletion contributions. The combination of background and ground state terms (the third and last terms of Equation 5.2) is always positive following

$$T' - C(t) A_{G1} n_G(t) = A_{G1} I_b \int P_b(t-\tau) \left[n_G\left(t^-\right) - n_G(t-\tau) \right] dt \qquad (5.4)$$

and $\left(n_G\left(t^-\right) - n_G(t-\tau)\right) > 0, \ \forall\, t$.

Rate Equation Mismatch with Data

Figure 5.5 shows the optimized fits of the discrete relaxation model (Equations 5.1 & 5.2) to two DT scans. Both were taken in the middle of the pump (left) and probe (right) energy ranges and test the model's ability to reproduce the most representative behaviors observed. For the lower energy (fixed) probe and higher pump power — the typical regime for a pump-probe measurement — the model can reproduce the experimental results fairly accurately. For the reverse case, however, the model as described fails to account for the narrow trough occurring ~150 fs after the initial peak. Note that if the probe had been restricted to the low power regime this failure of the rate equations to fully account for the nanotube dynamics would have been missed.

Two-Chiral Extension

Comparison of the DT scans across multiple pump and probe powers (see Fig.s 5.1 & 5.3) suggests that the kink originates from the same dynamics that produce the deep troughs at high pump powers. For this to be true increasing the probe power should correspond to an increase in the induced absorption. Instead the trough appears to get washed out by an

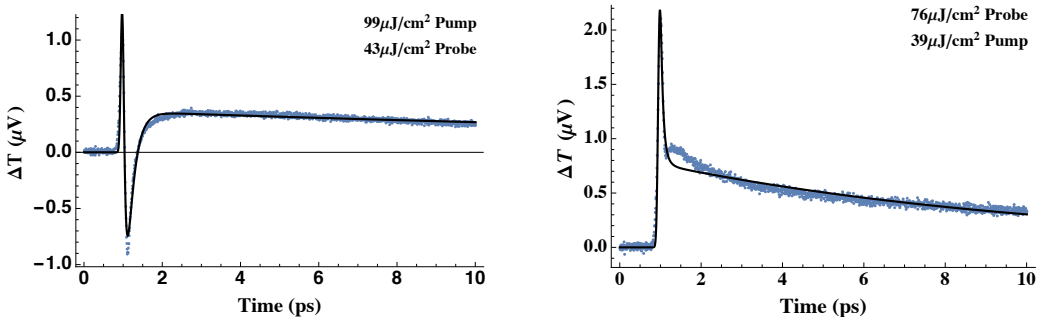

Figure 5.5: Single-chiral fit with mismatch. Optimized fits of rate equation model to differential transmission data. (Left) Model accurately reproduces deep trough that appears as pump energy densities increase. (Right) Model cannot reproduce the kink that remains at higher probe energy densities.

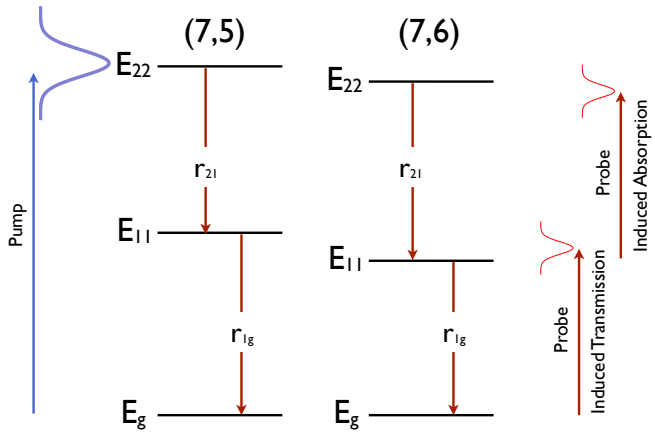

Figure 5.6: Two-chiral transitions. Multiple transitions interact with the pump and probe for $(7,5)$ and $(7,6)$ nanotubes.

increasing positive DT component that is apparently not accounted for by the relaxation model. This strongly suggests that there is an additional transition that can couple to the probe and that its contribution to the DT signal increases more rapidly with probe power than the contributions from the other transitions.

One likely source of this missing transition was strongly suggested in Figure 4.3 and Table 4.2 where both the $(7,5)$ and $(7,6)$ nanotubes are seen to be efficiently excited by the pump. Measured and calculated transition energies recorded in Table 4.2 also indicate that both nanotube species have transitions that overlap with the probe. The close relationship between the transition energies and the pump and probe are shown schematically in

Figure 5.6. Given the approximate transition energies of Table 4.2 it is likely that both the $(7,5)$ and $(7,6)$ nanotubes contributed to the measured differential transmission.

If the two nanotube species are assumed to be independent (as would have to be the case if the nanotube/polymer film has few or no bundles) the rate equation model can be directly extended by including a separate, identical system of equations for a second chirality. The transmission is then a function of the total contribution from both species independently. That is, the differential transmission now takes the extended form

$$\begin{aligned}\Delta T(t) = &-C_A(t)\left\{A_{12}n_{22,A}(t) + \left[A_{G1} - A_{12}\right]n_{11,A}(t) - A_{G1}n_{G,A}(t)\right\} \\ &- C_B(t)\left\{B_{12}n_{22,B}(t) + \left[B_{G1} - B_{12}\right]n_{11,B}(t) - B_{G1}n_{G,B}(t)\right\} + T' \qquad (5.5)\end{aligned}$$

Two-Chiral Model and Data

Early attempts to fit the data used the full two-chiral model assuming that both species contributed significantly to the induced absorption as well as the induced transmission (Equation 5.5). The results, however, were noisy and inconsistent as parameter values oscillated between the two species indicating an overdetermined system. This attempt also ignored the results seen in the left panel of Figure 5.5 showing that assuming a single chirality adequately described the induced absorption driven by the pump. The data fits shown in Figure 5.7 have therefore been calculated without the second induced absorption term, i.e., for $B_{12} = 0$. In this configuration one chiral species can reproduce the behavior seen in Figure 5.4 with both transmission and absorption terms while the second chiral species accounts for the induced transmission that washes out the absorption signature with rising probe power.

Figure 5.7 shows the combined differential transmission fits (red traces) for both the $(7,5)$ and $(7,6)$ nanotubes against the raw data (blue dots) for the same two data sets shown in Figure 5.5. The green trace represents the DT contribution from the nanotube species

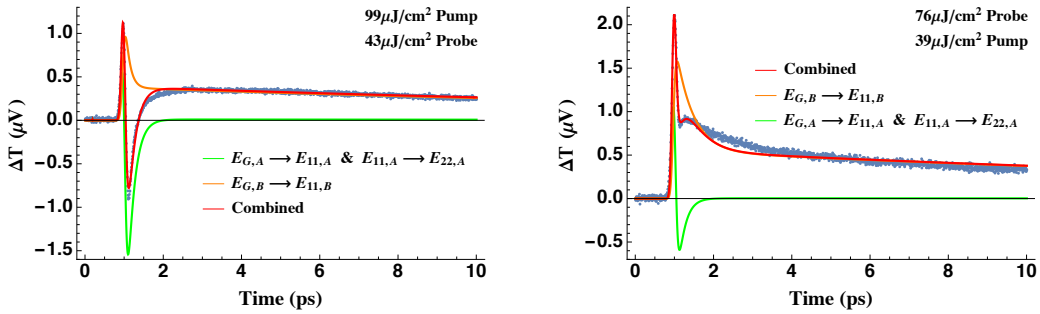

Figure 5.7: Two-chiral fit. Optimized fits for the rate equation model assuming two nanotube species with the differential transmission accounting for both. (Blue) Differential transmission data. (Green) Both ground and excited state transitions couple to probe. (Orange) Only ground state transition couples to probe. (Red) Total DT contribution from both chiralities.

exhibiting both induced transmission and absorption. The orange trace represents the contribution from the second nanotube species that only contributes induced transmission to the DT signal. Unlike the single chiral assumption (Eq. 5.2) seen to fail in Figure 5.5 the two fits shown in Figure 5.7 now reproduce the general relaxation behavior including the more distinctive cases in the data. Of particular note is that the rate equation model can account for the rapid changes in behavior a few hundred femtoseconds after the initial peak. For both data sets the deep trough seen in the high pump regime and the remnant kink of the washed out trough of the higher probe regime can be fit.

At early times the green and orange traces demonstrate the impact of the underlying competition between the induced absorption and transmission. In the first picosecond the induced absorption completely negates the net transmission of the combined DT signal. At later times the green trace shows a very weak positive DT suggesting only weak coupling to the first transition.

The fit is not ideal. In both cases, as well as the fits to all the other data sets not shown, the total optimized DT calculation exhibits an overshoot around one picosecond after the trough or kink. It is unlikely that the overshoot can be attributed to the minimal inclusion of saturation terms in Equation 5.5 since the behavior occurs after excited state absorption has mostly ceased. Rather, the deviation takes place at time scales where the dominant populations are shifting from primarily bright n_{11} excitons to dark n_D excitons.

It is also dominated by the contribution from the second chiral species that couples only to the ground state transition. This may suggest that there is a bottleneck in the transition to dark excitons that has not been accounted for by the rate equations. Such a bottleneck supports the underlying idea of a stable population of n_{11} excitons available for excited state absorption. On the other hand we would expect to see this balanced by an increase in exciton-exciton annihilation — not seen in the data or the literature — and a corresponding increase in the lifetime of the bright E_{11} excitons. The later is seen in the data but is not consistent with the literature.

The distinction between the two contributing nanotube chiralities is irrelevant to the fitting process. But we can make some reasonable assumptions based on the transitions listed in Table 4.2. Given that the probe was 1.17 eV with a linewidth of ~ 24 meV it should be expected to interact differently with the $(7,5)$ and $(7,6)$ nanotubes. For the $(7,6)$ tubes the probe should overlap efficiently with the excited state transition and only very weakly with the $E_{\mathrm{G}} \rightarrow E_{11}$ transition. This is consistent with the deep trough of the green trace representing case A of Equation 5.5 with nearly zero contribution at later times. In contrast, for the $(7,5)$ tubes the probe should overlap efficiently with the $E_{\mathrm{G}} \rightarrow E_{11}$ transition and weakly with the $E_{11} \rightarrow E_{22}$ transition consistent with the dominant induced transmission of the orange trace approximating case B with $B_{12} = 0$.

Coefficient Values from Optimized Fits

Table 5.1 shows the coefficient values determined by optimizing the fit of Equations 5.1 & 5.5 to the data. All of the parameters showed some variation from data set to data set, as expected, given experimental fluctuations between the data sets themselves. Most had standard deviations below 20% across all data sets. Of these the $\tau_{11,A}$ lifetime, the dark state lifetimes, the exciton-exciton annihilation rates and the $c_{21,B}$ branching coefficient from the $E_{22,\mathrm{B}}$ state into the $E_{11,\mathrm{B}}$ state are all consistent with the literature (See Appendix F for previously observed lifetimes).

Table 5.1: Rate equation fitting parameters. Optimized fitting parameters for the discrete rate equation model with two chiral species. Case B represents a second, independent nanotube species that only couples to the probe through the ground state transition. All parameters given in mean values except for $c_{21,A}$ and $\tau_{11,B}$ where ranges have been included for increasing pump (pp) and probe (pb) power in the data sets.

Case *A* $E_G \rightarrow E_{11}$ & $E_{11} \rightarrow E_{22}$		**Case *B*** $E_G \rightarrow E_{11}$	
Lifetimes ($1/r_{ii}$)			
$\tau_{22,A}$	34 (fs)	$\tau_{22,B}$	22 (fs)
$\tau_{11,A}$	175 (fs)	$\tau_{11,B}$	119_{pp}(fs) / 154-1041_{pb}(fs)
$\tau_{D,A}$	30 (ps)	$\tau_{D,B}$	24 (ps)
Exciton-Exciton Annihilation Rates γ (ps^{-1})			
γ_A	0.12	γ_B	0.19
Coupling Coefficients A_{ij} & B_{ij} (W^{-1})			
A_{G2}	25	B_{G2}	94
A_{G1}	0.67	B_{G1}	2.3
A_{12}	50	B_{12}	~0
Branching Coefficients c_{ij} (%)			
$c_{21,A}$	37-73_{pp} / 40-18_{pb}	$c_{21,B}$	83
$c_{1D,A}$	23	$c_{1D,B}$	50

The coupling coefficients, on the other hand, are simply too sample and experiment dependent to compare with other results. Similarly the c_{1D} branching coefficients depend critically on the presence of defects, traps and perturbations in the local dielectric which can significantly alter the evolution of bright E_{11} excitons (See section 4.3) and therefore the effective values of the branching coefficients. The τ_{22} lifetimes, while consistent with observations in the literature [77], are shorter than generally reported (also listed in Appendix F). Since they are well below the resolution of the pump-probe experiment they are

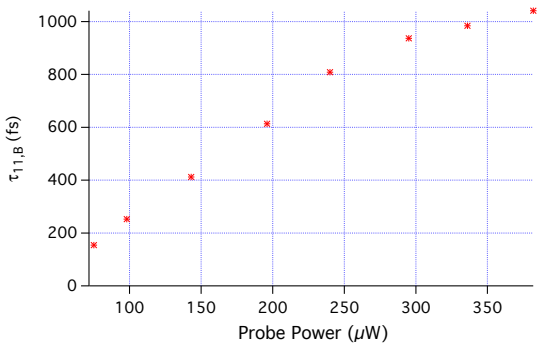

Figure 5.8: $E_{11,\mathrm{B}}$ lifetime variation. Increasing probe power results in increasing $E_{11,\mathrm{B}}$ exciton lifetime.

accepted as is or, alternatively, assumed to be free parameters necessary for solving the complete model.

branching coefficients depend critically on the presence of defects, traps and perturbations in the local dielectric which can significantly alter the evolution of bright E_{11} excitons (See section 4.3) and therefore the effective values of the branching coefficients.

Limitations of the Rate Equation Model

Despite the beautiful fits in Figure 5.7 the rate equation model presented has two troubling failures. Of the other fitting parameters the $\tau_{11,B}$ lifetime and the $c_{21,A}$ branching coefficient showed substantial variation: In addition to being uncharacteristically small [80, 81] the branching coefficient values diverged, increasing 50% as the pump power increased while decreasing 50% as the probe power increased; The variation in the $\tau_{11,B}$ lifetime was restricted to the increasing probe power results and was much worse as it increased by almost 700% over the range of the probe power (See Figure 5.8). Significantly, and unlike the results for the other parameters, the average values of these parameters determined for the pump variation and probe variation data sets separately were also not statistically close.

We can imagine that the large variation of the $c_{21,A}$ branching coefficient with pulse power is an indication of an increased phonon population preferentially driving the E_{22} state to the E_{11} state at the expense of radiative decay to the ground state. The phonon

population will certainly increase with the pump power since nonradiative relaxation from the E_{22} to the E_{11} state must generate phonons. An increase in phonon population due to relaxation, however, would have to be much different in the case of increasing probe power. Here, since the phonon population is still generated by relaxation from the E_{22} state, it would also be a function of both the excited state absorption and exciton-exciton annihilation repopulating the E_{22} state. These indirect driving mechanisms would result in a smaller phonon distribution and as a result any variation in the branching coefficient would be expected to be smaller. In this scenario the increased contribution from phonons would be expected to contribute to an increase in the value of the $c_{21,A}$ branching coefficient. The observation that the coefficient values instead diverge with increasing pump and probe powers, however, essentially refutes this hypothesis.

Variation in the $\tau_{11,B}$ lifetime appears to be unprecedented. Manzoni, et al., did find slowing τ_{22} lifetimes for higher excitation densities [78], but this is in contrast to many observations by Ma, et al., [173] and Valkunas, et al., [162] among others who observed faster decays driven by EEA. Manzoni attributed the change in relaxation rate to a phonon bottleneck where a large phonon population could quench the phonon emission rate from the E_{22} relaxation. A similar argument could be made here for the $E_{11,\mathrm{B}}$ lifetime increasing due to a phonon blockade. But the change in lifetime only occurs in the probe power variation case where an increase in phonon population should be less dramatic than the pump power variation case. This also rules out a possible contribution from saturation as this would also have to be driven by the pump.

The changes in value for two ostensibly constant parameters point to a failure in the rate equation model as conceived. One likely scenario could be a missing piece to the puzzle. Perhaps the rate equations do not account for all of the relevant dynamical changes seen in the electronic states of the nanotubes. But this contradicts the fact that the rate equations representing the two-chiral system were built from our current understanding of the relaxation cascade that takes place in a single chiral species. The restriction to low probe power

in earlier research, however, means that we may have arrived at the conclusion that the rate equation model captures everything, when in fact it does not. If the model captures all of the relevant physics, then the entire range of pump and probe powers — even atypically high probe powers — could be fit with the same set of parameters. Instead, excellent fits to the dynamics are found but only if the parameters are allowed to vary with intensity. The rate equation models based on the literature must therefore carry limitations as they fail to include key processes in the carrier dynamics and exciton interactions. As a result, we are left to conclude that this interpretation is simply not adequate for understanding the dynamics of a two-chiral system when a strong probe interacts with the system.

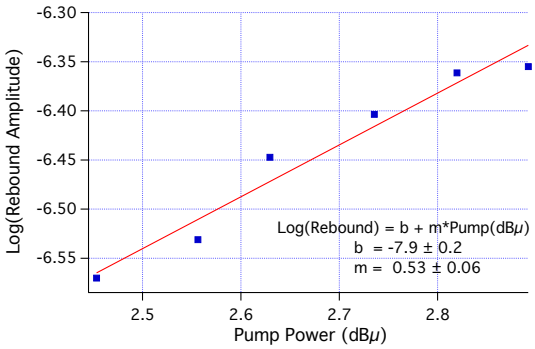

Figure 5.9: Rebound amplitude versus pump power. Log scale shows that the rebound amplitude varies with the square root of the pump power. The rebound amplitude acts as a proxy for the total E_{22} population (Section 4.3).

5.4 Coherent Dynamics in a Two-Chiral System

One possible explanation for the rate equation failure is hinted at in the results of Figure 5.3. The washout of the absorption signature when an increase would be expected suggests instead that the behavior should be interpreted in terms of Rabi oscillations. If the pump and probe are interacting coherently with the nanotubes, we might expect the total population to follow the field. And, in fact, in Figure 5.9 the data has been re-plotted (originally Figure 4.9) on a Log-Log scale. The result indicates that total population follows the field amplitude (square root of the intensity) rather than the intensity itself. While a similar

result was observed by Ma, et al., [89] for peak fluorescence values[3] their results cannot be directly compared to the amplitudes in Figure 5.9 measured at later times when EEA no longer dominates. We are left with the likely scenario that coherent interaction between the nanotubes and the fields may be contributing to the overall dynamics of the system. And there are other indications of coherent interaction. Both Rabi frequencies and pulse areas also strongly suggest that the data represents nanotube dynamics in a coherent regime.

Rabi frequencies Estimates of the Rabi frequencies, $\Omega = {}^{\mu \cdot E}/_{\hbar}$, can be made from the interband optical matrix elements. Following the approach by Malic and Knorr [30] the Rabi frequency for a specific transition can be expressed within the $\mathbf{A} \cdot \mathbf{p}$ Hamiltonian as

$$\Omega_z^{vc}(\boldsymbol{k}, t) = i\frac{e_o}{m_o} M_z^{vc}(\boldsymbol{k}) \cdot \mathbf{A}\,(t) \tag{5.6}$$

by assuming the incident light is polarized in the axial (z) direction of the nanotube. The $M_z^{vc}(\boldsymbol{k})$ in the expression represent the general interband optical matrix elements and can be derived as

$$M_z^{vc}(\boldsymbol{k}) = \frac{M_o}{2\sqrt{N}\,|e\,(\boldsymbol{k})|}\left[(n_1 - n_2)\cos\Psi_3 - (2n_1 + n_2)\cos\Psi_1 + (n_1 + 2n_2)\cos\Psi_2\right] \tag{5.7}$$

for a CNT with chiral indices (n_1, n_2). The other indices signify that the transition is between the valence (v) and conduction (c) bands. In this expression N is the number of hexagons per unit cell (Eq. 2.2) and $e\,(\boldsymbol{k}) = \sum_{j=1}^{3} e^{i\vec{k}\cdot\vec{b}_j}$ where the $\mathbf{b}_j$ are the connecting vectors between a given atom and its three nearest neighbors. The factor M_o represents the expectation value coming from the momentum operator so that by setting any $\mathbf{b}_j = b\hat{e}_x$ we get $M_o = \langle \phi\,(\boldsymbol{r}')\,|\partial_{x'}|\,\phi\,(\boldsymbol{r}' + be_{x'})\rangle$ where the $\phi\,(\boldsymbol{r}')$ are $2p_z$ orbital functions. Based on calculations by Malic and Knorr, and including a Coulomb correction to account for

[3] Ma, et al., modeled relaxation kinetics for early delay times finding evidence of the significant contribution the exciton-exciton annihilation process can have on exciton relaxation dynamics [89].

exciton binding, the factor has been approximated as $M_o \cong -3.5\,\mathrm{nm}^{-1}$.

The cosine functions, Ψ_i, encode much of the dependence of the matrix elements on the quasi-angular (m) and transverse (k_z) components of the electron momentum and are defined by[4]

$$\begin{aligned} \Psi_1 &= \pi m \tfrac{2n_1+n_2}{N} - a\tfrac{n_2}{q}k_z \\ \Psi_2 &= \pi m \tfrac{n_1+2n_2}{N} + a\tfrac{n_1}{q}k_z \\ \Psi_3 &= \pi m \tfrac{n_1-n_2}{N} - a\tfrac{n_1+n_2}{q}k_z \end{aligned} \tag{5.8}$$

where the wave vectors $\mathbf{k} = (m, k_z)$ are described in terms of these discrete and continuous components respectively. Here $a = |\vec{a}|$ is the translational period — the natural length of $\overrightarrow{T}$ for a nanotube's unit cell (See Fig. 2.2) — and q is the number of hexagons in a nanotube unit cell with the ratio a/q reducing to $a/q = (1/2)\, a_o \sqrt{3/N}$.

Calculated Rabi frequencies for the pump are in the range $0.07 - 0.12\,\mathrm{fs}^{-1}$ while for the probe they are in the range $0.05 - 0.11\,\mathrm{fs}^{-1}$. For both cases this puts $\Omega^{-1} \leq 20\,\mathrm{fs}$ while Fleming, et al., observed dephasing in nanotubes to be much larger at 205 fs [159].

Pulse areas Based on the Rabi frequency calculations the pulse areas

$$\theta = \int \Omega\,(t)\; dt \tag{5.9}$$

assuming integration over the full Gaussian pulse envelopes of these experiments. Figure 5.10 shows the growth of the pulse areas with fluence for both the pump and probe. Pulse areas are found to range from $\sim \pi/2$ to π for the 80 fs pump resonant with the E_{22} transition and π to 2π for the 120 fs probe resonant with the E_{11} transition. In this range the pulse areas are a strong indication that the rapid shifts in behavior may be due to pulses inverting populations or driving them into superpositions of states, i.e. coherences.

[4] These Ψ_i differ slightly from Malic and Knorr based on a recalculation.

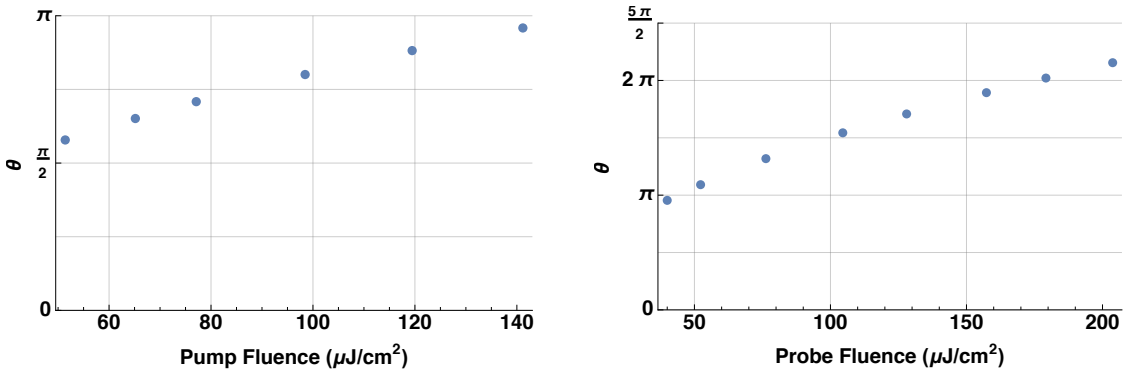

Figure 5.10: Pump and probe pulse areas. Both the pump (left) and probe (right) pulse areas, θ, approximate π-pulses in the range of fluences seen in the data.

Density Matrix Description of Nanotube Dynamics

The general idea behind the following coherent representation of the collective carbon nanotube dynamics is that they can be defined in terms of the discrete energy levels described in Equations 5.1 while accounting for the pump and probe fields interacting resonantly with the primary transitions. See Figure 5.11 for an illustrative description.

All of the transition rates and energies are taken from the measurements and fitting parameters described in the previous sections. The values specifically include results from the rate equation fits so that calculated results can be compared with the data as directly as possible.

Using the standard approach to including dissipation in a coherent light-matter interaction model [177] we begin with the general form of the system Hamiltonian with field interaction given by

$$H = H_o + H_{int} \tag{5.10}$$

where H_{int} is

$$H_{int} = -\vec{d} \cdot \vec{E}\,(t) = -E\,(t) \sum_{mn} d_{mn} \left|m\right\rangle \left\langle n\right| \tag{5.11}$$

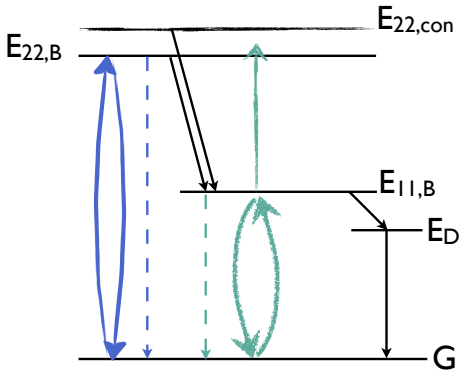

Figure 5.11: Coherent interaction with discrete level system. Textured arrows represent pump (blue) and probe (green) fields with curved arrows indicating coherent coupling between ground and exciton states. Dashed arrows (blue and green) depict radiative decay. Solid black arrows correspond to non-radiative decay.

and represents the first order dipole interaction of the light and nanotubes. The equation of motion can then be extended to account for dissipation channels including relaxation and dephasing by including the Lindblad equation resulting in the expression

$$\frac{\partial \rho}{\partial t} = -\frac{i}{\hbar}\left[H, \rho\right] + \sum_{s}\left(A_s \rho A_s^{\dagger} - \frac{1}{2}A_s^{\dagger}A_s\rho - \frac{1}{2}\rho A_s^{\dagger}A_s\right) \tag{5.12}$$

where the A_s represent system operators given by

$$A = \sum_{nm}\sqrt{\Gamma_{mn}}\left|m\right\rangle\left\langle n\right| \tag{5.13}$$

The operators account for each of the s dissipation channels including, in particular, relaxation and dephasing.

In the three sets of equations that follow the notation is that of M. Florian who generated the code used to test this dynamical interpretation [178]. Here ω_p and ω_b are the frequencies of the pump (p) and probe (b) respectively. Also note that the indices correspond to the exciton states, that is

$$\left|G\right\rangle \equiv \left|0\right\rangle,\ \left|11, D\right\rangle \equiv \left|1\right\rangle,\ \left|11, B\right\rangle \equiv \left|2\right\rangle,\ \left|22, B\right\rangle \equiv \left|3\right\rangle,\ \text{and}\ \left|22, D\right\rangle \equiv \left|4\right\rangle$$

For clarity the various components of equation 5.12 are described separately in terms of

the contributions from the population, polarization and dissipation dynamics.

The population dynamics are described by the diagonal matrix elements through the equations

$$\begin{aligned}
\dot{\rho}_{00}|_{pop} &= \Omega_{30}^{p}(t)\,\mathrm{Im}\left\{\rho_{03}e^{i(\omega_{30}-\omega_p)t}\right\} + \Omega_{20}^{b}(t)\,\mathrm{Im}\left\{\rho_{02}e^{i(\omega_{20}-\omega_b)t}\right\} \\
\dot{\rho}_{11}|_{pop} &= 0 \\
\dot{\rho}_{22}|_{pop} &= \Omega_{42}^{b}(t)\,\mathrm{Im}\left\{\rho_{24}e^{i(\omega_{42}-\omega_b)t}\right\} - \Omega_{20}^{b}(t)\,\mathrm{Im}\left\{\rho_{02}e^{i(\omega_{20}-\omega_b)t}\right\} \\
\dot{\rho}_{33}|_{pop} &= -\Omega_{30}^{p}(t)\,\mathrm{Im}\left\{\rho_{03}e^{i(\omega_{30}-\omega_p)t}\right\} \\
\dot{\rho}_{44}|_{pop} &= -\Omega_{42}^{b}(t)\,\mathrm{Im}\left\{\rho_{24}e^{i(\omega_{42}-\omega_b)t}\right\}
\end{aligned} \tag{5.14}$$

The polarizations are described by the off-diagonal matrix elements through the relations

$$\begin{aligned}
\dot{\rho}_{02} &= \tfrac{i}{2}\Omega_{02}^{b}(t)\left[\rho_{22}-\rho_{00}\right]e^{-i(\omega_{20}-\omega_b)t} + \tfrac{i}{2}\Omega_{03}^{p}(t)\,\rho_{32}e^{-i(\omega_{30}-\omega_p)t} - \tfrac{i}{2}\Omega_{42}^{b}(t)\,\rho_{04}e^{i(\omega_{42}-\omega_b)t} \\
\dot{\rho}_{03} &= \tfrac{i}{2}\Omega_{02}^{b}(t)\,\rho_{23}e^{-i(\omega_{20}-\omega_b)t} + \tfrac{i}{2}\Omega_{03}^{p}(t)\left[\rho_{33}-\rho_{00}\right]e^{-i(\omega_{30}-\omega_p)t} \\
\dot{\rho}_{04} &= \tfrac{i}{2}\Omega_{02}^{b}(t)\,\rho_{24}e^{-i(\omega_{20}-\omega_b)t} + \tfrac{i}{2}\Omega_{03}^{p}(t)\,\rho_{34}e^{-i(\omega_{30}-\omega_p)t} - \tfrac{i}{2}\Omega_{24}^{b}(t)\,\rho_{02}e^{-i(\omega_{42}-\omega_b)t} \\
\dot{\rho}_{23} &= \tfrac{i}{2}\Omega_{20}^{b}(t)\,\rho_{03}e^{i(\omega_{20}-\omega_b)t} + \tfrac{i}{2}\Omega_{24}^{b}(t)\,\rho_{43}e^{-i(\omega_{42}-\omega_b)t} - \tfrac{i}{2}\Omega_{03}^{p}(t)\,\rho_{20}e^{-i(\omega_{30}-\omega_p)t} \\
\dot{\rho}_{24} &= \tfrac{i}{2}\Omega_{20}^{b}(t)\,\rho_{04}e^{i(\omega_{20}-\omega_b)t} + \tfrac{i}{2}\Omega_{24}^{b}(t)\left[\rho_{44}-\rho_{22}\right]e^{-i(\omega_{42}-\omega_b)t} \\
\dot{\rho}_{34} &= \tfrac{i}{2}\Omega_{30}^{p}(t)\,\rho_{04}e^{i(\omega_{30}-\omega_p)t} - \tfrac{i}{2}\Omega_{24}^{b}(t)\,\rho_{32}e^{-i(\omega_{42}-\omega_b)t}
\end{aligned} \tag{5.15}$$

where the notation $\dot{\rho}_{ij}|_{pol}$ is assumed for $\dot{\rho}_{ij}$ for lack of a wide enough margin.

The contributions from dissipation, meanwhile, enter the density matrix calculations through the Lindblad terms as follows with the γ_{ij}^{*} terms representing pure dephasing and the Γ_{ij} denoting the relaxation rates.

$$
\begin{aligned}
\dot{\rho}_{00}|_d &= \Gamma_{30}\rho_{33} + \Gamma_{20}\rho_{22} + \Gamma_{10}\rho_{11} \\
\dot{\rho}_{11}|_d &= \Gamma_{21}\rho_{22} - \Gamma_{10}\rho_{11} \\
\dot{\rho}_{22}|_d &= \Gamma_{42}\rho_{44} + \Gamma_{32}\rho_{33} - (\Gamma_{21} + \Gamma_{20})\,\rho_{22} \\
\dot{\rho}_{33}|_d &= -(\Gamma_{32} + \Gamma_{30})\,\rho_{33} \\
\dot{\rho}_{44}|_d &= -\Gamma_{42}\rho_{44} \\
\dot{\rho}_{02}|_d &= -\tfrac{1}{2}(\Gamma_{21} + \Gamma_{20} + \gamma^*_{02})\,\rho_{02} \\
\dot{\rho}_{03}|_d &= -\tfrac{1}{2}(\Gamma_{32} + \Gamma_{30} + \gamma^*_{03})\,\rho_{03} \\
\dot{\rho}_{04}|_d &= -\tfrac{1}{2}\Gamma_{42}\rho_{04} \\
\dot{\rho}_{23}|_d &= -\tfrac{1}{2}(\Gamma_{32} + \Gamma_{30} + \Gamma_{21} + \Gamma_{20})\,\rho_{23} \\
\dot{\rho}_{24}|_d &= -\tfrac{1}{2}(\Gamma_{42} + \Gamma_{21} + \Gamma_{20} + 2\gamma^*_{24})\,\rho_{24} \\
\dot{\rho}_{34}|_d &= -\tfrac{1}{2}(\Gamma_{42} + \Gamma_{32} + \Gamma_{30})\,\rho_{34}
\end{aligned}
\tag{5.16}
$$

Populations by coherent model

By solving the equation of motion with strong field interactions, while accounting for the appropriate dissipation channels, predictions can now be made for the evolution of the nanotube system in a coherent regime representative of the experimental measurements. In particular, predictions of the exciton populations that underlie the measured DT signals can be distilled from these results. Unlike the incoherent rate equation model, however, the evolution of the populations now include their dependence on the polarizations and the likelihood of Rabi oscillations — contributions that were entirely neglected in the incoherent rate equation model.

The right-hand panel of Figure 5.12 depicts the exciton populations given by the coherent interaction model. For comparison these results are graphed next to the exciton populations found from the optimized data fits of Section 5.3. Despite differences in the notation and ranges the evolution of the E_{22}, $E_{11,\mathrm{B}}$ and $E_{11,\mathrm{D}}$ state populations show globally identical behavior. Significantly, however, the density matrix approach now also accounts for polarizations (overlapping traces of $|\mathrm{P}_{\mathrm{G}-11,\mathrm{B}}|$ and $|\mathrm{P}_{11,\mathrm{B}-22,\mathrm{D}}|$) in the system which

contribute to the system dynamics for several hundred femtoseconds.

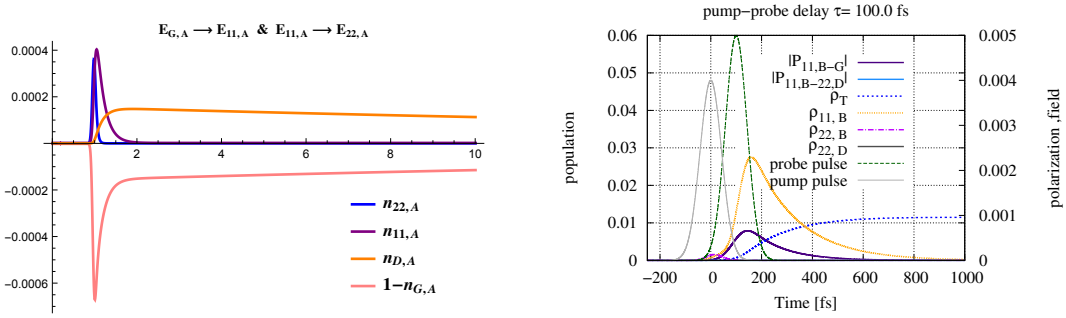

Figure 5.12: Evolution of exciton populations. Left) Population breakout from rate equation fit to data (pump-probe delay in picoseconds). Right) Population breakout from density matrix calculations for $\Omega_{pump} = 40/\text{fs}$ and $\Omega_{probe} = 5/\text{fs}$ at 100 fs pump-probe delay. Overlapping polarizations are also included. Coherent population data provided by Jahnke, et al., [179].

Differential absorption responses

The differential absorption (DA) can also be distilled from the solutions to Equation 5.12 through the microscopic polarization. Since the polarization is defined in terms of the susceptibility by $P = \varepsilon_o \chi E$ [177], and the absorption is a function of the imaginary part of the susceptibility, $\alpha(\omega, t) = (\omega^2/c^2 k)\, \chi''(\omega, t)$, the differential absorption follows. Figure 5.13 presents two aspects of the differential absorption calculations (take note that the DA has the opposite sign from the DT data discussed earlier in this chapter). The left-hand panel shows a progression of DA spectra for fixed pump ($\Omega_{30} = 0.004/\text{fs}$) and increasing pump-probe delay where both positive (absorption) and negative (transmission) regions can be seen in the spectra. The decay in amplitude with time is a direct consequence of including the dissipation channels in the coherent model and consistent with the data. The panel on the right demonstrates the power dependence at zero delay of both the transmission and absorption regions consistent with the expected connection between population and field strength.

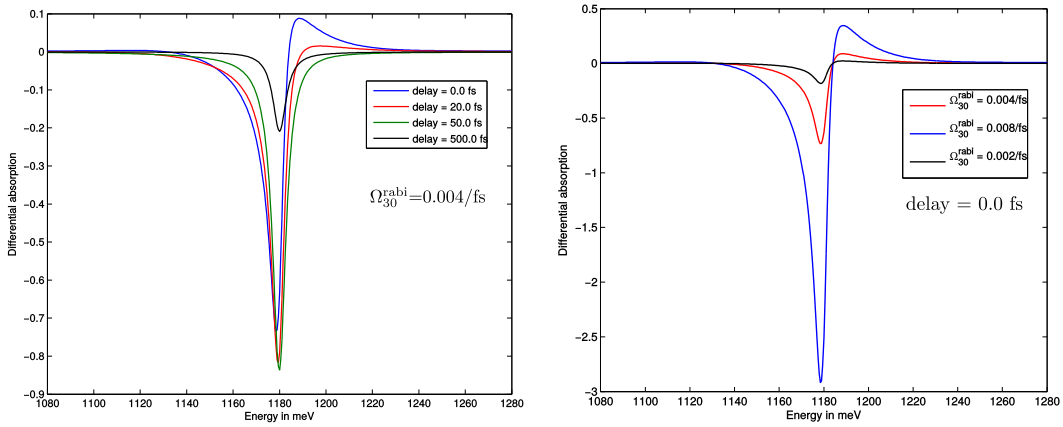

Figure 5.13: Differential absorption versus power and delay. Absorption for (left) various delays and (right) pump powers (Ω_{30} Rabi frequencies) in the coherent regime. [178]

Polarization effects

The impact of including polarization transfer in the coherent dynamical system can be seen in Figure 5.14. This graph demonstrates the change in lineshape when polarization is, and is not, present. The blue trace represents the case where all off-diagonal terms are set to zero except for the transitions (ρ_{02} and ρ_{03}) driven by the optical fields. The result shows that there is a direct correspondence between the polarizations and the emergence of a positive DA signal.

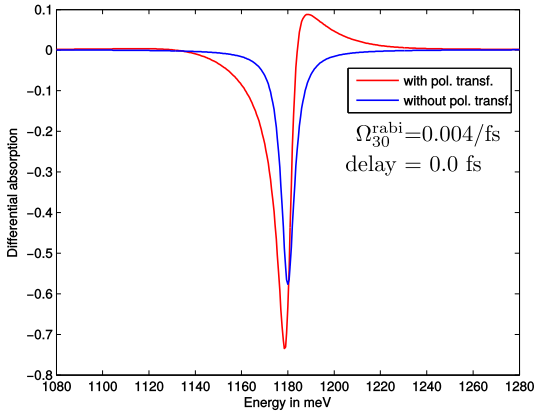

Figure 5.14: Polarization transfer. Blocking polarization transfer turns off the induced absorption. [178]

Power dependence for coherent interaction

The previous analyses considered absorption from the point of view of the susceptibility only. Florian and Jahnke [180] extended the model to include propagation through the sample so that calculations of the differential transmission could be more directly compared to the data. By assuming the sample is thin compared to an optical wavelength, propagation can then be accounted for by solving Maxwell's equation at the sample plane

$$E_{QW}(t) = E_o(t) - \frac{\mu_o c}{2}\frac{\partial}{\partial t}P(t) \tag{5.17}$$

where $E_o(t)$ represents the superposition of the pump and probe fields and the response of the carbon nanotubes is included through the macroscopic polarization $P(t)$. In this case the polarization is determined from the discrete density matrix calculations so that the complete model is a coupled set of Maxwell-Bloch equations.

The results from the propagation calculations can be seen in Figure 5.15. The left-hand graph covers the lower range of probe powers as the Rabi frequency, Ω_{20}, increases from $0.2/\text{fs}$ to $0.3/\text{fs}$. A kink in the calculated DT signal is clearly seen in the higher amplitude traces. Florian and Jahnke determined that the kink can be traced to polarization transfer between the pump and probe fields. The coherent aspect of these results is also revealed as the probe approaches a $\pi/2$-pulse and the amplitude diminishes with the system being driven into a superposition of states (black traces). Further increases in the probe power then cause the sign of the differential transmission to flip as the system is driven back towards a population state. As with the results in Figure 5.14 the polarizations play a key role in the DT behavior. If the polarization terms are turned off (not shown) the kinks disappear.

The emergence of a deep trough in the DT signal indicates that the absorption in this model is also power dependent as observed in the data. The fact that it appears as a function of the probe power instead of the pump, however, differs from the earlier assumption of ex-

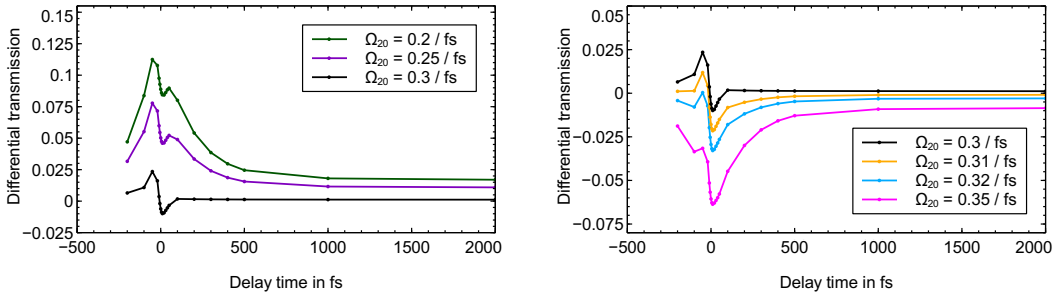

Figure 5.15: DT signal amplitude cycles with power. Signal progresses from transmission to absorption with increasing probe powers. Trend in left-hand graph continues into right-hand graph. Pump was fixed for $\Omega_{30} = 0.08/\text{fs}$. [181]

cited state absorption applied in the incoherent rate equation model. Instead, the power dependent trough amplitude supports the idea that the absorption behavior is more likely a result of the probe pulse cycling the nanotubes through population and superposition states. If I have described this in rather general terms it is because nanotubes are not simple two level atoms as in many Bloch sphere examples and the initially prepared state from the pump as well as the detuning are not precisely known. Despite this, the discrete density matrix approach shows that the general behavior and power dependence of the kink/absorption trough can be reproduced with an appropriate combination of pulse powers.

Pump-probe non-linearity

The black curve in the left panel of Figure 5.15 recreates behavior seen in the DT signal of the data but differs significantly in its origin. Where the kink seen in the original data corresponds to higher probe powers, in results of the coherent model it is the black curve that represents the highest pump and probe powers. This is not entirely surprising in a coherent interaction picture given the dramatic changes in behavior possible going from $\pi/2$ to π pulse areas. That is, in this coherent regime the results should be expected to be sensitive to small changes in pulse power. The apparent contradiction, therefore, is more likely an expression of this sensitivity.

Because the black traces correspond to the low pump and probe behavior of the data

an attempt was made to test the population and polarization responses to increases in the pump power rather than the probe. The results are graphed in Figure 5.16 for two slightly different probe powers $\Omega_{20} = 0.3/\text{fs}$, same as the black cure, and a slightly higher probe power giving $\Omega_{20} = 0.31/\text{fs}$.

Instead of observing an increase in the absorption predicted by the behavior of the data the trough shifts in time and a new trough emerges. Florian attributes this to the pump and probe simultaneously driving the nanotubes through Rabi oscillations [182]. In this scenario the pump and probe compete as the E_{22} and $E_{11,\text{B}}$ states are linked through the non-radiative decay path and Rabi oscillation depend in a non-linear way on the fields.

While the pump and probe powers in this test case are too high to compare with the data the new results and those summarized in Figure 5.15 provide testable predictions of the nanotube system behavior if the pulse powers were increased. They also underscore the sensitivity of the results to small variations in the probe power.

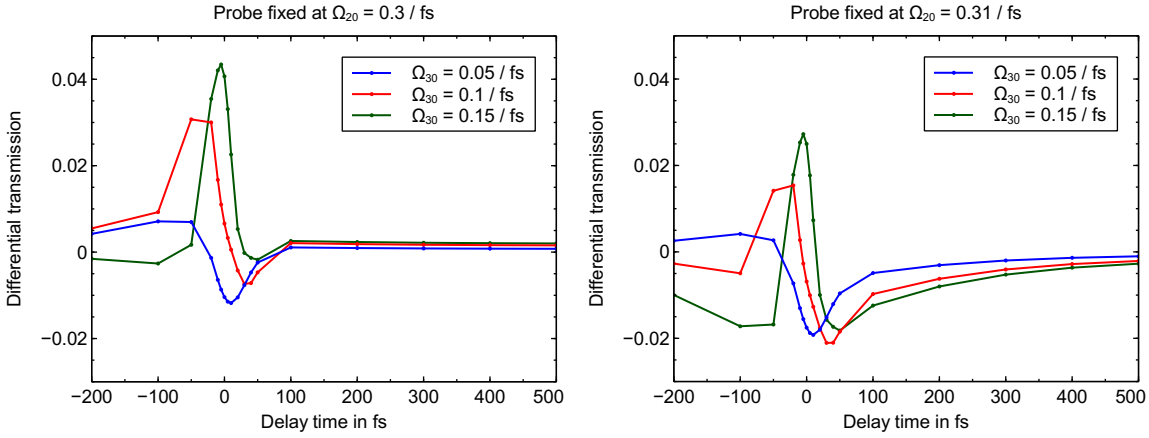

Figure 5.16: Oscillations in DT signal. Onset of pump-probe non-linearity with increasing pump power (Left & Right). Small increase in high probe power drives additional dip not yet observed in data (Right). [182]

5.5 Summary

The relaxation behavior of any system can deviate spectacularly from its expected behavior: If the material is driven into saturation, if the material being measured differs from

its expected structure, if we do not or cannot fully account for all of its energy levels, if there are additional mechanisms that can perturb typical relaxation steps . . . , we may see unexpected structure in the relaxation behavior.

In the case of the PFO/carbon nanotube films the deviations were surprising and significant. Instead of the expected monotonic relaxation behavior the differential transmission showed rapid sign changes in the data including a deep trough suggesting strong absorption.

Attempts to interpret this data followed two strategies. First, the data was analyzed in terms of a discrete set of rate equations representing all the known dynamical processes of the electronic states of CNTs. The model successfully fit the wide variation in ultrafast relaxation behaviors (Figures 5.1 & 5.3). Results indicated that two chiral species were likely present in the DT data and that there was significant competition between contributions of both photo-induced absorption and transmission. And most of the results were consistent with our current understanding of carbon nanotube dynamics. Despite this success, two fitting parameters could only be described in a range of values indicating that the rate equations do not constitute a complete model for the system dynamics.

The second strategy was to consider that the measured CNT dynamics exhibit coherent interaction between the nanotubes and the fields. A discrete density matrix approach based on results from the rate equation model reproduces the rapid oscillations in the DT signal and attributes this behavior to polarization transfer.

At higher pump and probe powers the coherent model predicts behaviors that have not yet been observed in the laboratory. One calculation predicts that, once initialized by the pump, increasing the probe power puts the nanotubes into a superposition of states and that further increases in the probe power will drive the nanotubes back into a population distribution that facilitates efficient absorption. A second calculation indicates that for select high pump and probe powers an additional oscillation in the DT signal will be observed due to non-linear competition as both the pump and probe drive Rabi flopping in their respec-

tive transitions. Both predictions should be testable and will lead to a better understanding of the dynamics of carbon nanotubes.

CHAPTER 6

Summary & Conclusions

The development of organic solar cells and electronics in general is a very active area of research with the ease of solution based manufacturing and reduced material costs as driving motivations [183, 184]. Organic solar cell prototypes, however, have struggled to reach efficiencies beyond a few percent [16]. Fortunately, improvements in efficiency have been achieved in part with hybrid organic/inorganic designs that overcome the limited diffusion lengths and spectral ranges found for the tightly bound excitons expressed by these photoactive polymers. Inclusion of Buckyballs (C60), semiconducting nano-crystals and/or carbon nanotubes in a hybrid solar cell, however, complicates the evolution of charge carriers as they relax, dissociate and/or diffuse through multiple materials from initial excitation to harvested photocurrent.

Understanding this evolution has been the primary goal of this research. Quite a few publications have addressed the relaxation dynamics of individual carbon nanotubes at this point but in order to optimize the design of a hybrid organic/inorganic solar cell we would like to know the contributions to the harvested photocurrent from each component. Losses can arise from rapid exciton decay, inefficient diffusion and trapping, and heterojunctions that cannot efficiently facilitate exciton dissociation to name just a few. Identifying and overcoming these losses could lead to significant improvements in efficiency.

The first step in this project has been to establish a measurement system that is consistent with our current understanding of carbon nanotube dynamics after optical excitation.

The primary goal was to ensure that these measurements can be extended to the multi-chiral polymer/nanotube blends that account for the broadband absorption in the solar cell design. The measurement system is based on a general understanding of the optical properties of carbon nanotubes and ultrafast pump-probe experiments to date.

- The optical properties of carbon nanotubes are dominated by excitonic states.
- Tightly bound excitons in CNTs can be described in terms of a ladder of discrete energy levels with the contributing degenerate singlet excitons splitting into four sublevels: One optically allowed bright state and three dipole forbidden states lower in energy.
- Non-degenerate pump–probe measurements can isolate the dynamics of single chiral species in a broad distribution of carbon nanotubes by populating the second excitonic state (E_{22}) and observing the evolution of the lower energy first excitonic state (E_{11}) as the targeted nanotubes relax.
- The excited state dynamics of CNTs can primarily be described with a rate equation model representing a simple cascade down a ladder of discrete energy levels. A complete description of excited state dynamics, however, must include excited state absorption and exciton-exciton annihilation.

Of course, all the best laid plans of mice and scientists can go awry in even the simplest of experiments.[1] Non-degenerate, or two-color, pump-probe measurements can, in general, isolate the relaxation dynamics of individual nanotube species. Unfortunately, the unique (E_{22}, E_{11}) exciton pairs that are easily identified in photoluminescence excitation measurements are not as easily isolated when broadband ultrafast pulses target multi-chiral nanotube distributions. Many studies (see Section 4.2) have addressed this problem by measuring highly purified samples of $(6, 5)$ nanotubes. Since the multi-chiral nature of our

[1] With apologies to Robert Burns and, of course, the "wee, sleekit, cow'rin, tim'rous beastie" [185].

samples is an important aspect of their design a different strategy was pursued. By probing the sample with atypically strong pulses, sensitive to both excited state populations and transitions, a multi-chiral picture of the nanotube dynamics was obtained.

Curiously the relaxation observed when these nanotube distributions were measured also shows unexpected deviations in behavior. Fitting the relaxation traces to discrete level rate equations reveals successes and failures. On the one hand the analysis, paired with knowledge of the relevant nanotube resonances, successfully distinguishes the contributions from different nanotube species and closely reproduces the experimental results. More importantly, most of the free parameters fit to values consistent with known lifetimes and branching coefficients. Surprisingly, the analysis also uncovers limitations to the rate equation treatment of CNTs. In a narrow range around 1.5 ps after excitation, for example, the data fits can only approximately reproduce the relaxation. In another example, two parameters (a branching coefficient and a lifetime) show remarkable variation when both would be expected to remain constant. Thus, attempting to fit a discrete level rate equation to nanotube relaxation in a strong probe regime reveals weaknesses in the model not previously seen in the literature.

An alternative picture of the relaxation behavior with its striking, short lived induced photoabsorption emerges when we consider the behavior on the ~ 100 fs time scale of the pump and probe pulses while the dephasing time has been observed to be as long as 205 fs [159]. Indirect measurements of the pump generated population following the field strength support a coherent interaction picture and approximations showing that the pump and probe pulse areas are on the order of π-pulses lend further support to the idea. In order to test this hypothesis a density matrix model of the nanotube system is proposed. The equation of motion is extended beyond the idealized system and interaction Hamiltonians to include the previously noted dephasing as well as the relaxation observations of this research so that computational results can then be compared with the data.

The coherent interpretation, like the rate equation model, finds some success and some

limitations in describing the nanotube dynamics. For a passive probe the general population dynamics, stemming largely from the rate equation results are consistent with the data. This includes the observation that a stronger pump corresponds to a small oscillation in the differential transmission spectrum — much like the kink in the data — which can be attributed to polarization transfer between the E_{11} and E_{22} states.

Not surprisingly, increasing the probe power contributes more questions than answers. While an initial increase in power corresponds to an increase in DT signal amplitudes the small kink, attributed here to polarization transfer, does not vary or bleach out as in the data. Then, by further increasing the probe power the excitation profile first shrinks down to one very reminiscent of the data then evolves into deep absorption troughs much like those seen for high pump powers. In a coherent regime this should indicate that the system is evolving from population states to superpositions and back. But it is notable that this progression is not entirely consistent with the data which follows this pattern as a function of the pump not the probe. One possible explanation for this inconsistent behavior is seen in the sensitivity of the model to small changes in the probe. For calculations of higher probe powers additional oscillations emerged alerting us to the underlying influence of transient grating effects. In the end, a coherent interpretation can reproduce nanotube relaxation dynamics but only over selected ranges of parameters.

Assessing an opto-electronic device with a heterogenous distribution of carbon nanotubes has unearthed challenges in identifying contributions from individual nanotube species that can be addressed in several ways that are largely successful but that ultimately do not lead to a complete picture of the underlying dynamics.

- Dispersed, multi-chiral nanotube ensembles contain spectrally congested neighborhoods that can be a challenge for ultrafast relaxation measurements. Broadband pulses can overlap multiple resonances resulting in the simultaneous observation of dynamics from various nanotube species.

- Incorporating a strong probe into a non-degenerate pump-probe experiment can un-

lock information about system dynamics that a traditional passive probe cannot access. In particular, for multi-chiral nanotube distributions a strong probe tuned to an excited state transition can help distinguish between the contributions from various nanotube species with similar excitation profiles.

- Discrete level rate equations based on our current understanding of nanotube dynamics cannot fully account for the relaxation behavior.

- A discrete matrix model that addresses coherent interaction with the pump and probe fields and is based on the observed nanotube relaxation dynamics is also unable to fully reproduce the measured behavior.

- Inclusion of a strong probe in the density matrix approach revealed that polarization transfer is a significant contributor to oscillations in the DT signal. Sensitivity to small changes in probe power also revealed the onset of non-linear (transient grating) effects.

Ultimately we would still like to establish a detailed understanding of all the contributions to the extracted photocurrent from a prototype solar cell. However, since the discrete level rate equation model was based on our current understanding of nanotube dynamics its inability to account for all aspects of the relaxation behavior suggests that we do not yet fully understand the physics involved. Analyzing the results in terms of a discrete density matrix confirmed that the coherent interaction picture should not be ignored. But it also confirms that both models are inadequate and a more complete microscopic theory is needed before we can fully understand the results from ultrafast measurements of a multi-chiral nanotube device.

APPENDIX A

Nanotube Classes and Families

Origin of the Modulo 3 Classification

The curious $(2n+m)\mathtt{mod}3$ classification of different nanotube chiralities observed in Chapter 2 comes out of the quantization constraint imposed by the finite circumference of each tube. This quantization condition $\vec{k} \cdot \vec{C_h} = 2\pi j,\ j \in \mathbb{Z}$, on the circumferential vector $\vec{C_h} = n\,\vec{a_1} + m\,\vec{a_2}$ can be expanded in terms of the lattice vectors to put a constraint on the variables k_x and k_y. Recall that the lattice vectors (fig. 2.2) are described by

$$\vec{a_1} = \frac{a_{C-C}}{2}\left(3, \sqrt{3}\right) \qquad \text{and} \qquad \vec{a_2} = \frac{a_{C-C}}{2}\left(3, -\sqrt{3}\right) \tag{A.1}$$

where $a_{C-C} = 1.42\text{Å}$ [6, 32] is defined as the nearest neighbor separation between carbon atoms in the graphene lattice. Substituting these vectors into the quantization condition we get the relation

$$\vec{k} \cdot \vec{C_h} = \frac{3a_{C-C}}{2}\,(n+m)\,k_x + \frac{\sqrt{3}a_{C-C}}{2}\,(n-m)\,k_y = 2\pi j \tag{A.2}$$

Now note that at the zero bandgap "Dirac points" *K* and *K′* the energy described by the graphene dispersion relation vanishes. In terms of the Brillouin zone shown in Figure 2.3 four of these Dirac points are of the form

$$K = (k_x, k_y) = \pm\left(\frac{2\pi}{3a_{C-C}}, \frac{2\pi}{3\sqrt{3}a_{C-C}}\right) \qquad \text{and} \qquad K' = \pm\left(\frac{2\pi}{3a_{C-C}}, \frac{-2\pi}{3\sqrt{3}a_{C-C}}\right) \tag{A.3}$$

Substituting the values of k_x and k_y from any of these four *K* and *K′* points into the quantization constraint (Eq. A.2) and simplifying we get

$$\frac{2n+m}{3} = j \tag{A.4}$$

Since $j \in \mathbb{Z}$ this result imposes the rule that for a nanotube with chirality (n, m), if $2n + m$ is integer divisible by 3 then the bands will cross the Dirac point and it is therefore metallic. Conversely if $2n + m$ is not integer divisible by 3 then the bands will not cross the Dirac point and the nanotube must be semiconducting.

The relationship between $(n - m)\mathtt{mod}3$ and $(2n + m)\mathtt{mod}3$

Another classification, the $(n-m)\mathtt{mod}3$ classification, is occasionally used in the literature. This classification and the $(2n + m)\mathtt{mod}3$ classification are not independent. They should be thought of as alternatives although $(2n + m)\mathtt{mod}3$ appears to be (I've never counted) a much more common classification in the literature.

In the derivation of the classification equation (Eq. A.4) only four of the Dirac points found in the 2D Brillouin zone of graphene were considered. The other two high symmetry *K* points are located at

$$K'' = \pm\left(0, \frac{4\pi}{3\sqrt{3}a_{C-C}}\right) \tag{A.5}$$

The double prime is just to distinguish these points from the previously discussed Dirac points. For graphene each Dirac point can be reproduced through a simple combination of $\pi/3$ rotations. For carbon nanotubes, however, the transformation from *K* or *K′* to *K″* is not

strictly equivalent to moving between *K* and *K′*. The other two high symmetry points I'm calling *K″*, however, still constitute Dirac points at which the graphene bandgap vanishes and can be treated as a linear combination of the *K* and *K′* points. Because of this they have a similar effect on the zone folding criteria seen above.

Substituting the values of k_x and k_y from *K″* into equation A.2 as before yields

$$\frac{n-m}{3} = j \tag{A.6}$$

where $j \in \mathbb{Z}$ as before. The resulting equation is nearly the same as Equation A.4 and similarly divides the nanotubes into metallic and semiconducting classes.

Rewriting Equations A.4 and A.6 in terms of the cyclic nature of division by 3 we get the criteria $(2n+m)\texttt{mod}3$ and $(n-m)\texttt{mod}3$ respectively. Both criteria distinguish between metallic, when either = 0, and semiconducting nanotubes, when either $= \pm 1$. The answers for the semiconducting tubes differ in sign but represent the same properties. To see the connection between $(n-m)\texttt{mod}3$ and $(2n+m)\texttt{mod}3$ for the chiral indices n and m the relationship has to be described in terms of the modulo 3 algebra. Briefly, for $p, p' \in \{0, 1, -1\}$, we know

$$(2n+m)\texttt{mod}3 = p \tag{A.7}$$

Similarly

$$(2m+n)\texttt{mod}3 = p' \tag{A.8}$$

Adding them we see

$$p + p' = (2n+m)\texttt{mod}3 + (2m+n)\texttt{mod}3 = (3n+3m)\texttt{mod}3 = 0 \tag{A.9}$$

so that $p' = -p$. Meanwhile, let $(n-m)\texttt{mod}3 = q$. Now the relation between the two

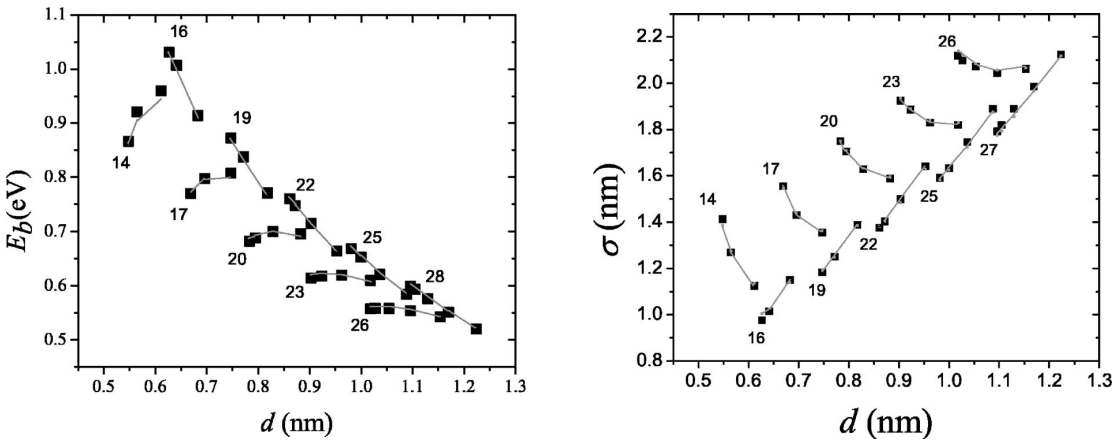

Figure A.1: Kataura plots. Capaz, et al., demonstrates consistent properties of nanotube families [153]. Connected points belong to the same family where $2n + m =$ constant. Left) Binding energies, E_{b} (eV), of lowest-energy bright excitons as a function of tube diameter. Right) Exciton sizes, σ (nm), of the same bright excitons versus diameter.

forms can be found from

$$p - p' = (2n + m)\mathtt{mod}3 - (2m + n)\mathtt{mod}3 = (n - m)\mathtt{mod}3 = q \tag{A.10}$$

In other words $2p = q$. In terms of the modulo 3 algebra (where $2 \equiv -1$) the mapping $(2n+m)\mathtt{mod}3 \rightarrow (n-m)\mathtt{mod}3$ maps $\{0, 1, -1\} \rightarrow \{0, -1, 1\}$. The semiconducting classes are simply switched.

Families and Kataura Plots

In addition to the metallic versus semiconducting classification several patterns can be observed across multiple nanotube chiralities. CNTs for which $2n + m =$ constant, for example, have comparable diameters with varying chiral angles while nanotubes for which $n - m =$ constant follow the opposite pattern with families of chiral angles but different diameters [41]. Similar patterns can be found for binding energies and exciton sizes [153]. These patterns can be easily seen in what have become known as Kataura plots after Kataura, et al., demonstrated the appearance of these patterns in 1999 [186]. Representative Kataura plots for binding energies and exciton sizes from calculations by Capaz, et al.,

can be see in Figure A.1.

Just as the families described above exhibit patterns, the two semiconducting nanotube classes also follow predictable patterns. Much of the distinction between parameters from one class or the other can be qualitatively attributed to the trigonal warping of the graphene dispersion relation near a Dirac point. This trigonal warping effect is discussed in Appendix B.

APPENDIX B

Ratio Test

Free-carrier assumptions for modeling excited states in carbon nanotubes predicted that the ratio of second to first excited state E_{22}/E_{11} would converge to 2 for large diameters [31]. Experimental results did not agree, however, with O'Connell, et al. finding $E_{22}/E_{11} \sim 1.7$ [10], Bachilo, et al. finding $E_{22}/E_{11} \sim 1.85$ [42] and Weisman, et al., depicted in Figure B.1, finding $E_{22}/E_{11} \sim 1.8$ [40].

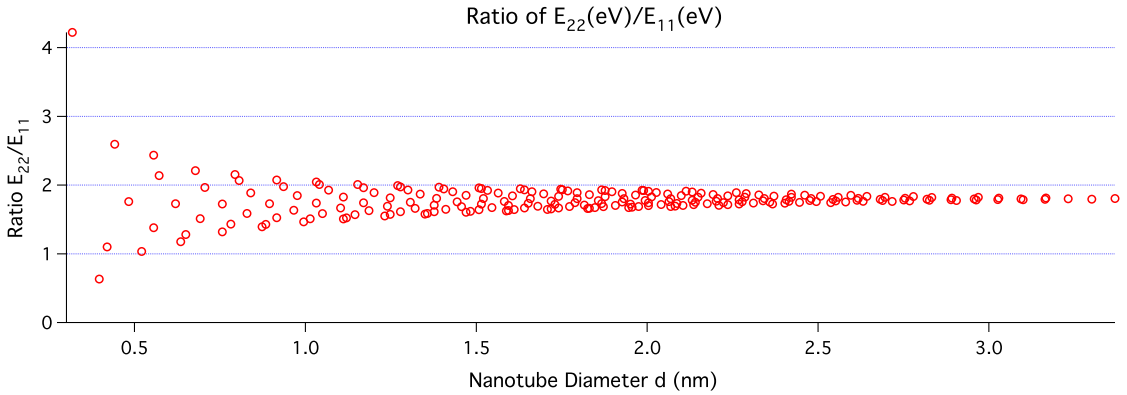

Figure B.1: The "Ratio Problem." The measured ratio of the first two excited states, E_{22} and E_{11} as a function of nanotube diameter. In this data set the ratio converges to 1.80 [40].

The discrepancy between the predicted ratio and what has been observed is a direct result of assuming that the electronic structure of a carbon nanotube (CNT) can be described within a free-carrier model. With this assumption the transition energies can be entirely determined by the energy dispersion relation derived for CNTs as extensions of graphene (Eq.s 2.3 & 2.5). The free-carrier bands derived in this way (see Fig. 2.4) show that the

lowest energy excitations are described by the two bands in closest proximity to one of the Dirac points. Since these bands were determined by the zone-folding criteria they are separated within the graphene Brillouin zone by $2\pi/\|\vec{C}_h\| = 2/d_t$ where d_t is the tube diameter. The closest band will lie at one-third of this band-to-band separation from the *K* point [31]. The second band will then have to be at two-thirds the separation from the *K* point. For larger diameter nanotubes this band-to-band separation will be very small bringing the first two bands in very close to the Dirac point where the approximation of the Dirac cone is most accurate. Since the Dirac cone is linear in energy we can reasonably estimate that the second excited state should be twice the first, i.e., $E_{22}/E_{11} \sim 2$. Comparing the expectation that $E_{22}/E_{11} \sim 2$ to the reality of Figure B.1 there are two notable discrepancies. First, for smaller diameter nanotubes there is a notable scatter. And second is that the ratio converges to 1.8 for larger diameters and not to the idealized value 2.

Trigonal Warping

If one stays within the single-electron framework of the tight binding model for graphene one can still explain the scatter for smaller diameter nanotubes as a result of trigonal warping. The term trigonal warping [31] refers to the transformation of the graphene bandstructure from conical — close to a *K* point — to triangular for crystal momenta further away. For large diameter nanotubes with dispersion relations that cut close to a *K* point the ratios will be roughly the same and close to the convergent value. For smaller and smaller tube diameters, however, the resulting increase in band-to-band separation moves the bands further away from the Dirac point where the CNT bands cut across more complex contours of the graphene dispersion relation. Figure B.2 (a) shows how the bands of the (6, 1) nanotubes — for which $(2n + m) \bmod 3 = 1$ — cut through regions of the graphene dispersion where contours are more triangular than circular. Similarly, Figure B.2 (b) shows the closest bands of the $(6, 2)$ nanotubes — for which $(2n + m) \bmod 3 = 2$ — cutting across contours but

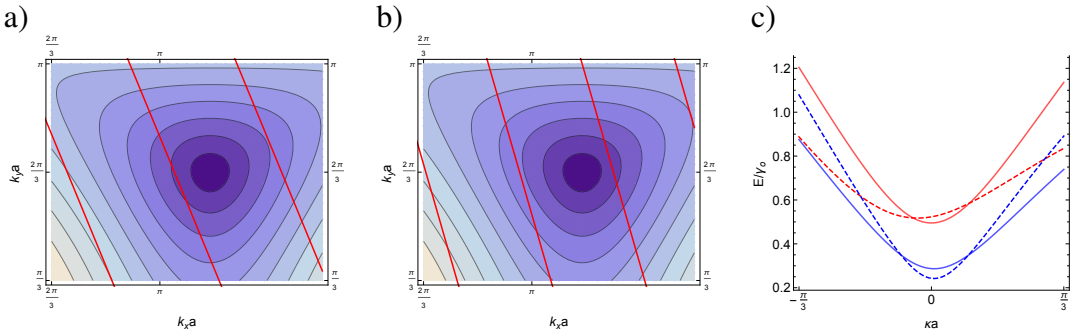

Figure B.2: Effect of trigonal warping on CNT class and bandstructure. a) $\pi^\star$ branches nearest K point for $(6,1)$ nanotubes. b) $\pi^\star$ branches nearest K point for $(6,2)$ nanotubes. c) First two branches for both $(6,1)$, (solid) with $(2n+m)\,\mathrm{mod}3 = 1$, with $(6,2)$, (dashed) and $(2n+m)\,\mathrm{mod}3 = 2$, nanotubes showing opposite trends at their minima due to trigonal warping. Graphs inspired by similar calculations shown in Fig. 4 of Jorio, et al., [187].

with the opposite offset to the one seen for $(6,1)$ tubes. The switched offset results in slices cutting across contours of a different nature despite having roughly the same diameters. In Figure B.2 (c) the CNT bands cutting across the $\pi^\star$ (upper) surface are compared. The solid lines representing the $(6,1)$ nanotubes show that the branch corresponding to the E_{22} exciton is lower in energy than for the $(6,2)$ tubes at their minima. The opposite is true for the E_{11} branches. As a result the E_{22}/E_{11} ratios depicted in Figure B.1 deviate higher and lower (for the $(6,2)$ and $(6,1)$ nanotubes respectively) than the convergent value seen for larger diameters. And this is true in general for the $(2n+m)\,\mathrm{mod}3 = 2$ class nanotubes verses the $(2n+m)\,\mathrm{mod}3 = 1$ class tubes resulting in the increasing scatter as the nanotube diameters get smaller.

Binding Energies

The convergence of the E_{22}/E_{11} ratio to a value other than 2 cannot be explained in terms of the free-particle model. As noted above, the expectation that the ratio should be 2 is based simply on the assumption of π–to–$\pi^\star$ excitations within a Dirac cone. Nothing in this model accounts for the strong Coulomb interactions between charge carriers in the tightly confined geometry of a carbon nanotube. In Chapter 2 I discussed the fact that in order to

properly model the electronic properties of CNTs a many-body formalism is needed that includes the formation of bound excitons. One of the observations that comes from this more comprehensive model is that the binding energies for the E_{22} excitons are (almost entirely) larger than for the E_{11} excitons [30]. As a result the free particle transitions Δ_{11} and Δ_{22} are disproportionately reduced and the ratios, E_{22}/E_{11}, of the exciton transition energies must be < 2.

APPENDIX C

Irreducible Representations and Exciton Wavevectors

The following table, graphs and discussion, unless otherwise noted, are taken entirely from publications by Barros, et al., to provide a fuller explanation of the exciton degeneracy discussion and graph presented in the main text (See Fig. 2.7). The complete set of symmetry relations and graphs are presented for comparison of the chiral nanotube case with those of the achiral (both *armchair* and *zig-zag*) nanotube results not discussed [188, 68]. The symmetries presented here apply to the one- and two-photon transitions that generate E_{ii} excitons in CNTs. The interested reader is strongly encouraged to consult the comprehensive discussion of all the symmetry-related properties in the original Physics Letters paper [188].

Table C.1 compares the irreducible representations of the Line Group (LG) and the Group of the Wave Vector (GWV) for carbon nanotubes as described by Barros. The irreducible representations were arrived at by evaluating the direct product of the individual components — the conduction (c) and valence (v) states and the envelope function (F_ν) of the exciton — under the effective mass approximation (EMA). For the E_{11} state of a chiral nanotube, for example, they assume that the Coulomb interaction mixes the inequivalent free-electron and -hole states and that the exciton is represented by the $\nu = 0$ envelope function to get

$$\begin{aligned}\mathcal{D}(\psi^{EMA}) &= \mathcal{D}(\varphi_c)\otimes\mathcal{D}(\varphi_v)\otimes\mathcal{D}(F_\nu)\\ &= \left[E_{\tilde{\mu}}(k_o)+E_{-\tilde{\mu}}(-k_o)\right]\otimes\left[E_{-\tilde{\mu}}(-k_o)+E_{\tilde{\mu}}(-k_o)\right]\otimes A_1(0)\\ &= A_1(0)+A_2(0)+E_{\tilde{\mu}'}(k')+E_{-\tilde{\mu}'}(-k')\end{aligned}$$

The quasi-angular momentum ($\tilde{\mu}' = 2\tilde{\mu}$) and linear momentum ($k' = 2k_o$) refer to the exciton momenta and may differ in value if they fall outside the first Brillouin zone.

Table C.1: Irreducible representations for carbon nanotube symmetry. (*Reproduction of TABLE 1 and caption from Barros, et al.*): Irreducible representations ($\mathcal{D}$) relevant to the exciton problem for chiral and achiral nanotubes. GWV and LG stand for "group of the wave vector" and "line group" notation, respectively. The dimension (d) of each representation is shown on the right (sic) for both GWV and LG formalisms. The last column describes the wave vector (k), quasi-angular momentum ($\tilde{\mu}$) and parity quantum numbers (II). For chiral tubes, the relevant parity is related to the C_2 operation (Π^{C_2}), whereas for achiral tubes the parity II is also related to σ_h, σ_ν reflections and inversion i. The GWV notation chooses the parity under i as a quantum number and the LG notation chooses the parity under σ_h as a quantum number, thus making the translation between the two notations somewhat cumbersome. A zero parity quantum number means that the representation does not have a well defined parity [68].

	GWV		LG		
Chiral	$\mathcal{D}$	d	$\mathcal{D}$	d	$(k,\tilde{\mu},\Pi^{C_2})$
	$A_1(0)$	1	${}_0A_0^+$	1	$(0,0,+1)$
	$A_2(0)$	1	${}_0A_0^-$	1	$(0,0,-1)$
	$[\mathbb{E}_{\tilde{\mu}}(k)+\mathbb{E}_{-\tilde{\mu}}(-k)]$	1	${}_kE_{\tilde{\mu}}$	2	$(\pm k,\pm\tilde{\mu},0)$
Achiral	$\mathcal{D}$	d	$\mathcal{D}$	d	$(k,\tilde{\mu},\Pi^{\sigma_v},\Pi^{\sigma_h},\Pi^{i},\Pi^{C_2})$
	$A_{1u}(0)$	1	${}_0B_0^-$	1	$(0,0,-1,-1,-1,+1)$
	$A_{2u}(0)$	1	${}_0A_0^-$	1	$(0,0,+1,-1,-1,-1)$
	$A_{1g}(0)$	1	${}_0A_0^+$	1	$(0,0,+1,+1,+1,+1)$
	$A_{2g}(0)$	1	${}_0B_0^+$	1	$(0,0,-1,+1,+1,-1)$
	$E_{\lvert\tilde{\mu}\rvert u}(0)$	2	${}_0E_{\lvert\tilde{\mu}\rvert}^{\Pi^{\sigma_h}}$	2	$(0,\tilde{\mu},0,(-1)^{\tilde{\mu}+1},-1,0)$
	$E_{\lvert\tilde{\mu}\rvert g}(0)$	2	${}_0E_{\lvert\tilde{\mu}\rvert}^{\Pi^{\sigma_h}}$	2	$(0,\tilde{\mu},0,(-1)^{\tilde{\mu}},+1,0)$
	$[B'(k)+B'(-k)]$	1	${}_kE_n^A$	2	$(\pm k,n,+1,0,0,0)$
	$[B''(k)+B''(-k)]$	1	${}_kE_n^B$	2	$(\pm k,n,-1,0,0,0)$
	$[E_{\lvert\tilde{\mu}\rvert}(k)+E_{\lvert\tilde{\mu}\rvert}(-k)]$	2	${}_kG_{\tilde{\mu}}$	4	$(\pm k,\tilde{\mu},0,0,0,0)$

The free-carrier and excitonic states are depicted qualitatively in Figure C.1, also from Barros, et al. For both chiral and achiral nanotubes it shows the component free-electron and -hole dispersions nearest the Dirac points and the resulting exciton dispersions by the

irreducible representations determined above [68]. The two-electron and two-hole states with the opposite quantum numbers transform as the A_1 and A_2 irreducible representations and those with the same quantum numbers transform as the $E_{\tilde{\mu}'}$ and $E_{-\tilde{\mu}'}$ representations. Since the interaction between the electric field of the light parallel to the nanotube axis and the electric dipole of the carbon nanotube transforms as the A_2 representation only the exciton with the corresponding symmetry will be optically active [188]. The result is a single bright exciton with three energetically similar dark excitons. And, while this was the calculation for the first excited state only, the large energy separation between excited states leads to negligible mixing between states and an equivalent exciton distribution at each level.

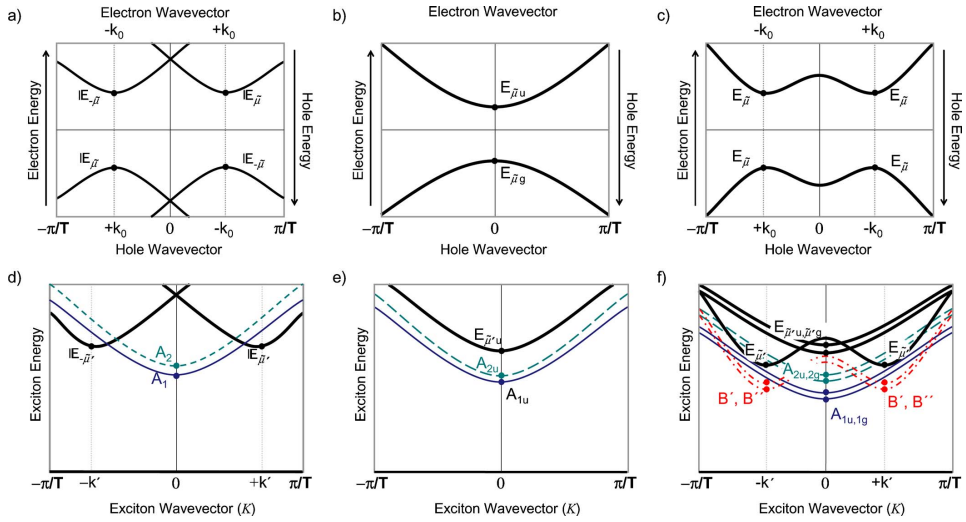

Figure C.1: Electronic and excitonic bands. (*Figure and caption from Barros, et al.*) Diagrams for the electronic bands and symmetries for (a) chiral (n,m), (b) zigzag (n, 0), and (c) armchair (n,n) nanotubes and for their respective excitonic bands (d), (e), and (f). The electron, hole and exciton states at the band edges are indicated by a solid circle and labeled according to their irreducible representation. Different line types and colors in this figure are related to bands with different symmetries. Thick (black solid) lines correspond to the $E_{\tilde{\mu}'}$ representation, the blue (thin solid) lines correspond to A_1 excitons while the cyan (thin dashed) lines correspond the A_2 excitonic states. In the case of achiral nanotubes, we also have inversion and mirror plane symmetries. For a better visualization, the bands with different parities under the inversion and mirror planes were grouped together and appear with the same line color and pattern. In the case of armchair nanotubes, the bands that transform as the B' and B'' representations are shown using a red dot-dash pattern. The electronic and excitonic band structures shown here are only pictorial. Group theory does not order the values for the eigenenergies and energy dispersions [68].

It should be noted that the confident placement of the A_2 exciton above the A_1 exciton and below the others cannot actually be determined by group theory. The relative energies must be determined by experiment or calculation.

One interesting result of this study is a contradiction of earlier research based on exciton parity. In an important study by Wang, et al., one- and two-photon absorption was used to access different excited states of the lowest energy E_{11} exciton. These authors argued that selection rules for one- and two-photon absorption were such that they could effectively select states in the Rydberg ladder of the excited states of the E_{11} exciton [45]. While their results are consistent with the other studies confirming exciton formation their assumptions of selection rules are contradicted by those of Barros just discussed. Using their analysis both excitation schemes lead to the same symmetry. Barros therefore concludes that oscillator strengths must be considered to gain a full picture of the available excitations.

APPENDIX D

Carbon Nanotube Film Preparation

A suspension of carbon nanotubes (raw grade HiPCO, Unidym [102]) was made with a loading of 1 mg/ml carbon nanotubes in 2 wt% sodium dodecyl sulfate/deionized water solution. Nanotube bundles were dispersed using a 400 W probe sonicator for 30 min at 25% amplitude. The suspension was then centrifuged at 280,000 g for 1 hr and the supernate collected to select material with primarily singly dispersed CNTs. 10 ml of the supernate was filtered through anodic alumina filters (Whatman Anodisc 0.02 μm pore size) to make a film of CNTs which was then rinsed to remove residual surfactant. The film was re-dispersed in 10 ml of 10 mg/ml poly[9,9-dioctylfluorenyl-2,7-diyl] (PFO, American Dye Source) dissolved in chlorobenzene using the probe sonicator at 10% amplitude for 30 min. The suspension was then centrifuged for 6 hours at 14000 g to remove remaining bundles and particulates and the supernate collected. The film was formed on quartz substrates using multiple passes of a film casting knife (e.g. a "doctor-blade") resulting in a thickness of ~ 45 nm[1] as described previously [16].

[1]The samples that were specifically prepared for the experiments discussed in this dissertation were actually ~ 100 nm.

APPENDIX E

Optical Resonances Distilled from the Absorption Profile

Table E.1 summarizes the results of fitting the shoulder of the full absorption spectrum (Inset, Fig. 4.1) to the individual absorption spectra of 25 carbon nanotubes. Figure 4.2 showing the individual absorption lines — as well as the total combined absorption spectrum and original data — is reproduced here for comparison. All absorption lines are assumed to be Gaussian in profile (see Ch. 4).

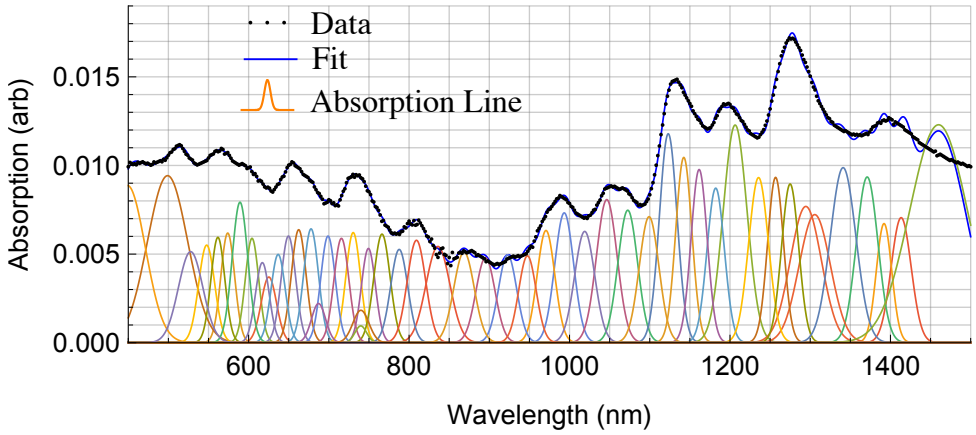

Figure E.1: Nanotube absorption lines. Many individual nanotube absorption lines combine to make up the substructure of the complex absorption spectrum determined in Section 4.1. Deconstructing the substructure yields resonant energies and linewidths. (Same as Figure 4.2)

As discussed in Chapter 4 the specific nanotubes represented in the fitting algorithm were chosen because of evidence for their presence (PLE data, Section 4.1), their likely presence as seen in the literature and their likely presence due to any misfit by the algorithm

without them. The last criterion is really a failure of the second in which only the most likely chiralities were chosen for the fit. In fact, even the least likely chiralities may be present but at populations too small to detect in an ensemble measurement. The least likely chiralities were neglected primarily for the sake of computation speed but also because the algorithm cannot distinguish between likely and unlikely nanotubes leading to improbable results. An indication of missing chiralities can be seen in the individual lines at the limits of the absorption spectrum. Table E.1 lists some amazing and improbable line widths for the nanotubes at the range limits — see, for example, the $(6, 2)$'s. This could only be improved upon with information on the additional presence of specific nanotubes (i.e. with photoluminescence excitation (PLE) or resonance Raman spectroscopy).

Nano-material bandgaps in general must be sensitive to the surrounding dielectric environment due to both their molecular scale and their characteristically high surface-to-volume ratio. For CNTs one also has to take into account the possibility of local variation in the dielectric over any extended nanotube. Local variation of this sort is particularly likely in organic materials and different results from sample to sample are to be expected. Even for experiments where attempts were made to isolate nanotubes from the environment, bandgap energies have shown tube-to-tube variation in their blue shifts relative to ensemble measurements of surfactant coated nanotubes [58]. As a result the values listed in Table E.1 have to be considered the best available for my sample — there is no realistic way to verify these results with a different sample.

More comprehensive assignments of nanotube resonances have been made by Bachilo, et al., [42, 104], Fantini, et al., [189], and Weisman, et al., [40] for various samples. These tabulated results are convenient for validating results but only after accounting for the dielectric environment dependent spectral shifts that will occur between samples.

Table E.1: Transition energies and linewidth estimates. Nanotube distribution fit to the PFO/CNT-blend absorption shoulder. Chiralities listed by increasing diameter (not shown) to be consistent with the literature.

Chirality	E_{11} Resonances			E_{22} Resonances			Ratio
(n,m)	λ_c	E_{11} (eV)	ΔE_{11} (meV)	λ_c	E_{22} (eV)	ΔE_{22} (meV)	E_{22}/E_{11}
(5, 3)	740	1.68	53	528	2.35	160	1.40
(6, 2)	923	1.34	39	449	2.76	322	2.05
(7, 2)	836	1.48	62	625	1.98	72	1.34
(6, 4)	895	1.38	43	589	2.10	82	1.52
(7, 3)	1019	1.22	35	499	2.48	296	2.04
(6, 5)	993	1.25	35	574	2.16	77	1.73
(8, 3)	971	1.28	34	678	1.83	59	1.43
(10, 0)	1182	1.05	23	548	2.26	97	2.16
(9, 2)	1162	1.07	22	562	2.21	80	2.07
(7, 5)	1046	1.18	34	650	1.91	63	1.61
(8, 4)	1123	1.10	26	604	2.05	67	1.86
(10, 2)	1073	1.16	31	766	1.62	50	1.40
(7, 6)	1142	1.09	22	662	1.87	61	1.72
(9, 4)	1099	1.13	30	740	1.68	38	1.49
(11, 1)	1306	0.95	33	617	2.01	66	2.12
(10, 3)	1257	0.99	18	637	1.95	64	1.97
(8, 6)	1206	1.03	30	730	1.70	50	1.65
(9, 5)	1236	1.00	24	687	1.80	54	1.80
(8, 7)	1295	0.96	34	749	1.65	45	1.73
(13, 0)	1413	0.88	18	699	1.77	54	2.02
(12, 2)	1392	0.89	14	716	1.73	53	1.94
(10, 5)	1275	0.97	19	809	1.53	51	1.58
(10, 6)	1371	0.90	21	788	1.57	50	1.74
(13, 2)	1341	0.92	26	868	1.43	49	1.54
(15, 1)	1460	0.85	49	948	1.31	35	1.54

APPENDIX F

Lifetime Variations

Table F.1 lists a snapshot of some relevant relaxation lifetimes. It shows a remarkable range in time scales between dipole allowed photoluminescence to ultrafast decay from the E_{22} excitonic state. More surprising is the variation seen in measurements of the same transition. One of the most striking differences can be seen in the fluorescence lifetimes of Wang vs Hagen in 2004 [112, 190]. And yet both were measured using the same technique. Later Berciaud, et al. [158] observed similar order of magnitude discrepancies and attributed the differences to relaxation from the band edge versus from a dark state only a few meV below.

Similar discrepancies can be seen for the E_{11} dark state lifetimes. In this case, given the comparatively long lifetimes of dark states and high mobility of excitons in CNTs differences in lifetimes may be more representative of the local environment. Given the high mobility of carbon nanotubes and their relative lengths, excitons can easily travel through varying dielectric environments, encounter defect sites, be captured by deep traps or decay at quenching sites. All of these possibilities can significantly alter an intrinsic lifetime.

Variations in lifetimes can also occur if there is residual bundling [141], if the temporal resolution in the experiment is insufficient to untangle multi-exponential decay rates, if pump energies are resonant with phonon sidebands [77] or if there hasn't been a full accounting of all dynamical processes as seen above with exciton-exciton annihilation or

excited state absorption.

Table F.1: Selected relaxation lifetimes for carbon nanotubes.

Lifetimes	Description	Author
E_{22} Exciton Lifetimes (Resonantly pumped)		
400 fs	Transient Polarized Pump-Probe with Ultra-Broadband Probe	Luer, et al. (2009) [46]
39 – 52 fs	Non-Degenerate Pump-Probe with 10 fs Pulses on Small Aggregates	Luer, et al. (2010) [141]
40 fs	Non-Degenerate Pump-Probe with 15 – 30 fs Pulses	Manzoni, et al. (2005) [78]
Bright E_{11} Exciton Lifetimes (Radiative & non-radiative decay)		
2 ps	Early Degenerate Pump-Probe Assumes Free-Electron Relaxation	Huang, et al. (2004) [92]
0.3 – 1.5 ps	Early Non-Degenerate Pump-Probe Lifetimes Sensitive to pH	Kono, et al. (2004) [191]
400 fs	Non-Degenerate Pump-Probe with 15 – 30 fs pulses	Manzoni, et al. (2005) [78]
Bright to Dark E_{11} Exciton Transition (${}_0\mathbf{A}_0^- \rightarrow {}_0\mathbf{B}_0^-$)		
~ 6 ps	Deconvolved Transient Spectra	Zhu, Z. P., et al. (2007) [94]
3 ps	Transient Grating Measurements	Seferyan, H. Y., et al. 2006 [67]
160 fs	Low Power Transient Absorption on Zig-Zag Nanotubes	Ma, Y. Z., et al. 2006 [91]
Dark E_{11} Exciton Lifetimes (Dipole forbidden decay)		
280 ps	Transient Grating Measurements	Seferyan, H. Y., et al. 2006 [67]
20 – 200 ps	Isolated $(6, 4)$ nanotubes in SDS. Lifetimes varied from tube to tube.	Hagen, A., et al. 2005 [76]
~ 50 ps	Enriched (DNA wrapped) $(6, 5)$ nanotubes	Chou, S. G., et al. 2005 [192]
Fluorescence Lifetimes		
110 ns	Time resolved photoluminescence	Wang, F., et al. 2004 [190]
10 ns	Time resolved photoluminescence	Hagen, A., et al. 2004 [112]
10 ns	Ab initio calculation of radiative lifetimes Includes bright & dark excitons	Spataru, C. D., et al. 2005 [73]

Bibliography

[1] G. Mittal, V. Dhand, K. Y. Rhee, S. J. Park, and W. R. Lee. A review on carbon nanotubes and graphene as fillers in reinforced polymer nanocomposites. *Journal of Industrial and Engineering Chemistry*, 21:11–25, 2015.

[2] H. He, L. A. Pham-Huy, P. Dramou, D. Xiao, P. Zuo, and C. Pham-Huy. Carbon nanotubes: applications in pharmacy and medicine. *Biomed Res Int*, 2013:578290, 2013.

[3] D. Jariwala, V. K. Sangwan, L. J. Lauhon, T. J. Marks, and M. C. Hersam. Carbon nanomaterials for electronics, optoelectronics, photovoltaics, and sensing. *Chem Soc Rev*, 42(7):2824–60, 2013.

[4] M. Scarselli, P. Castrucci, and M. De Crescenzi. Electronic and optoelectronic nanodevices based on carbon nanotubes. *J Phys Condens Matter*, 24(31):313202, 2012.

[5] C. Dekker. Carbon nanotubes as molecular quantum wires. *Physics Today*, 52(5):22–28, 1999.

[6] M. P. Anantram and F. Leonard. Physics of carbon nanotube electronic devices. *Reports on Progress in Physics*, 69(3):507–561, 2006.

[7] S. Iijima. Helical microtubules of graphitic carbon. *Nature*, 354(6348):56–58, 1991.

[8] K. S. Novoselov, A. K. Geim, S. V. Morozov, D. Jiang, Y. Zhang, S. V. Dubonos, I. V. Grigorieva, and A. A. Firsov. Electric field effect in atomically thin carbon films. *Science*, 306(5696):666–669, 2004.

[9] P. R. Wallace. The band theory of graphite. *Physical Review*, 71(9):622–634, 1947.

[10] M. J. O'connell, S. M. Bachilo, C. B. Huffman, V. C. Moore, M. S. Strano, E. H. Haroz, K. L. Rialon, P. J. Boul, W. H. Noon, C. Kittrell, J. P. Ma, R. H. Hauge, R. B. Weisman, and R. E. Smalley. Band gap fluorescence from individual single-walled carbon nanotubes. *Science*, 297(5581):593–596, 2002.

[11] T. Ando. Excitons in carbon nanotubes. *Journal of the Physical Society of Japan*, 66(4):1066–1073, 1997.

[12] M. Ichida, S. Mizuno, K. Tani, Y. Saito, and A. Nakamura. Exciton effects of optical transitions in single-wall carbon nanotubes. *Journal of the Physical Society of Japan*, 68(10):3131–3133, 1999.

[13] T. Dürkop, S. A. Getty, Enrique Cobas, and M. S. Fuhrer. Extraordinary mobility in semiconducting carbon nanotubes. *Nano Letters*, 4(1):35–39, 2003.

[14] A. Bachtold, P. Hadley, T. Nakanishi, and C. Dekker. Logic circuits with carbon nanotube transistors. *Science*, 294(5545):1317–20, 2001.

[15] P. Avouris, M. Freitag, and V. Perebeinos. Carbon-nanotube photonics and optoelectronics. *Nature Photonics*, 2(6):341–350, 2008.

[16] M. S. Arnold, J. D. Zimmerman, C. K. Renshaw, X. Xu, R. R. Lunt, C. M. Austin, and S. R. Forrest. Broad spectral response using carbon nanotube/organic semiconductor/C60 photodetectors. *Nano Lett*, 9(9):3354–8, 2009.

[17] M. Bockrath, D. H. Cobden, J. Lu, A. G. Rinzler, R. E. Smalley, L. Balents, and P. L. McEuen. Luttinger-liquid behaviour in carbon nanotubes. *Nature*, 397(6720):598–601, 1999.

[18] O. Nairz, M. Arndt, and A. Zeilinger. Experimental verification of the Heisenberg uncertainty principle for fullerene molecules. *Physical Review A*, 65(3), 2002.

[19] E. Kymakis and G. A. J. Amaratunga. Electrical properties of single-wall carbon nanotube-polymer composite films. *Journal of Applied Physics*, 99(8), 2006.

[20] P. M. Ajayan, L. S. Schadler, C. Giannaris, and A. Rubio. Single-walled carbon nanotube-polymer composites: Strength and weakness. *Advanced Materials*, 12(10):750–753, 2000.

[21] A. H. Barber, S. R. Cohen, and H. D. Wagner. Measurement of carbon nanotube-polymer interfacial strength. *Applied Physics Letters*, 82(23):4140–4142, 2003.

[22] Hong-Zhang Geng, Ki Kang Kim, Kang Pyo So, Young Sil Lee, Youngkyu Chang, and Young Hee Lee. Effect of acid treatment on carbon nanotube-based flexible transparent conducting films. *Journal of the American Chemical Society*, 129(25):7758–7759, 2007.

[23] A. K. Geim and K. S. Novoselov. The rise of graphene. *Nature Materials*, 6(3):183–191, 2007.

[24] J. Lu, P. S. E. Yeo, C. K. Gan, P. Wu, and K. P. Loh. Transforming C-60 molecules into graphene quantum dots. *Nature Nanotechnology*, 6(4):247–252, 2011.

[25] Juan Peng, Wei Gao, Bipin Kumar Gupta, Zheng Liu, Rebeca Romero-Aburto, Liehui Ge, Li Song, Lawrence B. Alemany, Xiaobo Zhan, Guanhui Gao, Sajna Antony Vithayathil, Benny Abraham Kaipparettu, Angel A. Marti, Takuya Hayashi, Jun-Jie Zhu, and Pulickel M. Ajayan. Graphene quantum dots derived from carbon fibers. *Nano Letters*, 12(2):844–849, 2012.

[26] M. V. Berry and A. K. Geim. Of flying frogs and levitrons. *European Journal of Physics*, 18(4):307, 1997.

[27] T. W. Odom, J. L. Huang, P. Kim, and C. M. Lieber. Structure and electronic properties of carbon nanotubes. *Journal of Physical Chemistry B*, 104(13):2794–2809, 2000.

[28] S. Morim Santos. *Optical Spectroscopy of Bound Excitonic States in Single Walled Carbon Nanotubes*. Thèse de Docteur, L'Université de Bordeaux 1, 2012.

[29] M. I. Katsnel´son. *Graphene: carbon in two dimensions*. Cambridge University Press, New York, 2012.

[30] Ermin Malic, Andreas Knorr, and Library Wiley Online. *Graphene and carbon nanotubes: ultrafast optics and relaxation dynamics*. Wiley-VCH, Weinheim, Germany, 2013.

[31] R. Saito, G. Dresselhaus, and M. S. Dresselhaus. Trigonal warping effect of carbon nanotubes. *Physical Review B*, 61(4):2981–2990, 2000.

[32] A. H. Castro Neto, F. Guinea, N. M. R. Peres, K. S. Novoselov, and A. K. Geim. The electronic properties of graphene. *Reviews of Modern Physics*, 81(1):109–162, 2009.

[33] S. Reich, J. Maultzsch, C. Thomsen, and P. Ordejon. Tight-binding description of graphene. *Physical Review B*, 66(3), 2002.

[34] M. Ouyang, J. L. Huang, C. L. Cheung, and C. M. Lieber. Energy gaps in "metallic" single-walled carbon nanotubes. *Science*, 292(5517):702–705, 2001.

[35] C. D. Spataru, S. Ismail-Beigi, L. X. Benedict, and S. G. Louie. Excitonic effects and optical spectra of single-walled carbon nanotubes. *Physical Review Letters*, 92(7), 2004.

[36] O. Jost, A. A. Gorbunov, W. Pompe, T. Pichler, R. Friedlein, M. Knupfer, M. Reibold, H. D. Bauer, L. Dunsch, M. S. Golden, and J. Fink. Diameter grouping in bulk samples of single-walled carbon nanotubes from optical absorption spectroscopy. *Applied Physics Letters*, 75(15):2217–2219, 1999.

[37] J. W. G. Wildoer, L. C. Venema, A. G. Rinzler, R. E. Smalley, and C. Dekker. Electronic structure of atomically resolved carbon nanotubes. *Nature*, 391(6662):59–62, 1998.

[38] D. Kienle, J. I. Cerda, and A. W. Ghosh. Extended Huckel theory for band structure, chemistry, and transport. I. Carbon nanotubes. *Journal of Applied Physics*, 100(4), 2006.

[39] Gyungseon Seol, Youngki Yoon, James K Fodor, Jing Guo, Akira Matsudaira, Diego Kienle, Gengchiau Liang, Gerhard Klimeck, Mark Lundstrom, and Ahmed Ibrahim Saeed. CNTbands, 2006, from https://nanohub.org/resources/1838.

[40] R. B. Weisman and S. M. Bachilo. Dependence of optical transition energies on structure for single-walled carbon nanotubes in aqueous suspension: An empirical Kataura plot. *Nano Letters*, 3(9):1235–1238, 2003.

[41] A. Jorio, G. Dresselhaus, M. S. Dresselhaus, and SpringerLink. *Carbon Nanotubes Advanced Topics in the Synthesis, Structure, Properties and Applications*. Topics in Applied Physics, 0303-4216; 111. Springer-Verlag Berlin/Heidelberg, Berlin, Heidelberg, 2008.

[42] S. M. Bachilo, M. S. Strano, C. Kittrell, R. H. Hauge, R. E. Smalley, and R. B. Weisman. Structure-assigned optical spectra of single-walled carbon nanotubes. *Science*, 298(5602):2361–6, 2002.

[43] Y. Z. Ma, L. Valkunas, S. M. Bachilo, and G. R. Fleming. Exciton binding energy in semiconducting single-walled carbon nanotubes. *Journal of Physical Chemistry B*, 109(33):15671–15674, 2005.

[44] J. Maultzsch, R. Pomraenke, S. Reich, E. Chang, D. Prezzi, A. Ruini, E. Molinari, M. S. Strano, C. Thomsen, and C. Lienau. Exciton binding energies in carbon nanotubes from two-photon photoluminescence. *Physical Review B*, 72(24), 2005.

[45] F. Wang, G. Dukovic, L. E. Brus, and T. F. Heinz. The optical resonances in carbon nanotubes arise from excitons. *Science*, 308(5723):838–841, 2005.

[46] L. Luer, G. Lanzani, J. Crochet, T. Hertel, J. Holt, and Z. V. Vardeny. Ultrafast dynamics in metallic and semiconducting carbon nanotubes. *Physical Review B*, 80(20), 2009.

[47] Y. Z. Ma, J. Stenger, J. Zimmermann, S. M. Bachilo, R. E. Smalley, R. B. Weisman, and G. R. Fleming. Ultrafast carrier dynamics in single-walled carbon nanotubes probed by femtosecond spectroscopy. *Journal of Chemical Physics*, 120(7):3368–3373, 2004.

[48] L. Perfetti, T. Kampfrath, F. Schapper, A. Hagen, T. Hertel, C. M. Aguirre, P. Desjardins, R. Martel, C. Frischkorn, and M. Wolf. Ultrafast dynamics of delocalized and localized electrons in carbon nanotubes. *Physical Review Letters*, 96(2), 2006.

[49] Robert S. Knox. *Theory of excitons*, volume 5 of *Solid state physics. Supplement;*. Academic Press, New York, 1963.

[50] Steven G. Louie and Marvin L. Cohen. *Conceptual foundations of materials: a standard model for ground and excited state properties*. Contemporary concepts of condensed matter science; 2. Elsevier, Boston, MA, 2006.

[51] Neil W. Ashcroft and N. David Mermin. *Solid state physics*. Holt, Rinehart and Winston, New York, 1976.

[52] J. Jiang, R. Saito, G. G. Samsonidze, A. Jorio, S. G. Chou, G. Dresselhaus, and M. S. Dresselhaus. Chirality dependence of exciton effects in single-wall carbon nanotubes: Tight-binding model. *Physical Review B*, 75(3), 2007.

[53] S. Kilina, E. Badaeva, A. Piryatinski, S. Tretiak, A. Saxena, and A. R. Bishop. Bright and dark excitons in semiconductor carbon nanotubes: insights from electronic structure calculations. *Physical Chemistry Chemical Physics*, 11(21):4113–4123, 2009.

[54] G. D. Scholes, S. Tretiak, T. J. McDonald, W. K. Metzger, C. Engtrakul, G. Rumbles, and M. J. Heben. Low-lying exciton states determine the photophysics of semiconducting single wall carbon nanotubes. *Journal of Physical Chemistry C*, 111(30):11139–11149, 2007.

[55] S. Tretiak. Triplet state absorption in carbon nanotubes: A TD-DFT study. *Nano Letters*, 7(8):2201–2206, 2007.

[56] E. Malic, M. Hirtschulz, S. Reich, and A. Knorr. Excitonic absorption spectra and ultrafast dephasing dynamics in arbitrary carbon nanotubes. *Physica Status Solidi-Rapid Research Letters*, 3(6):196–198, 2009.

[57] E. Malic, M. Hirtschulz, J. Maultzsch, S. Reich, and A. Knorr. Environmental influence on linear optical spectra and relaxation dynamics in carbon nanotubes. *Physica Status Solidi B-Basic Solid State Physics*, 246(11-12):2592–2597, 2009.

[58] O. Kiowski, S. Lebedkin, F. Hennrich, S. Malik, H. Rosner, K. Arnold, C. Surgers, and M. M. Kappes. Photoluminescence microscopy of carbon nanotubes grown by chemical vapor deposition: Influence of external dielectric screening on optical transition energies. *Physical Review B*, 75(7), 2007.

[59] L. Luer, S. Hoseinkhani, M. Meneghetti, and G. Lanzani. Dynamical screening of the exciton resonance in conjugated polymers/carbon nanotubes composites. *Physical Review B*, 81(15), 2010.

[60] V. Perebeinos, J. Tersoff, and P. Avouris. Scaling of excitons in carbon nanotubes. *Physical Review Letters*, 92(25), 2004.

[61] Claude Cohen-Tannoudji, Bernard Diu, and Franck Laloë. *Quantum mechanics. Vol. 2*. Mecanique quantique.English. Wiley, New York, 1977.

[62] R. J. Nicholas, I. B. Mortimer, L. J. Li, A. Nish, O. Portugall, and G. L. J. A. Rikken. Temperature and magnetic field dependent photoluminescence from carbon nanotubes. *International Journal of Modern Physics B*, 21(8-9):1180–1188, 2007.

[63] T. Ando. Spin-orbit interaction in carbon nanotubes. *Journal of the Physical Society of Japan*, 69(6):1757–1763, 2000.

[64] V. Perebeinos, J. Tersoff, and P. Avouris. Radiative lifetime of excitons in carbon nanotubes. *Nano Letters*, 5(12):2495–2499, 2005.

[65] S. J. Tans, M. H. Devoret, H. J. Dai, A. Thess, R. E. Smalley, L. J. Geerligs, and C. Dekker. Individual single-wall carbon nanotubes as quantum wires. *Nature*, 386(6624):474–477, 1997.

[66] G. A. Steele, F. Pei, E. A. Laird, J. M. Jol, H. B. Meerwaldt, and L. P. Kouwenhoven. Large spin-orbit coupling in carbon nanotubes. *Nature Communications*, 4, 2013.

[67] H. Y. Seferyan, M. B. Nasr, V. Senekerimyan, R. Zadoyan, P. Collins, and V. A. Apkarian. Transient grating measurements of excitonic dynamics in single-walled carbon nanotubes: The dark excitonic bottleneck. *Nano Letters*, 6(8):1757–1760, 2006.

[68] E. B. Barros, R. B. Capaz, A. Jorio, G. G. Samsonidze, A. G. Souza, S. Ismail-Beigi, C. D. Spataru, S. G. Louie, G. Dresselhaus, and M. S. Dresselhaus. Selection rules for one- and two-photon absorption by excitons in carbon nanotubes. *Physical Review B*, 73(24), 2006.

[69] F. Kuemmeth, S. Ilani, D. C. Ralph, and P. L. McEuen. Coupling of spin and orbital motion of electrons in carbon nanotubes. *Nature*, 452(7186):448–52, 2008.

[70] B. F. Habenicht, C. F. Craig, and O. V. Prezhdo. Time-domain ab initio simulation of electron and hole relaxation dynamics in a single-wall semiconducting carbon nanotube. *Physical Review Letters*, 96(18), 2006.

[71] A. Srivastava, H. Htoon, V. I. Klimov, and J. Kono. Direct observation of dark excitons in individual carbon nanotubes: Inhomogeneity in the exchange splitting. *Physical Review Letters*, 101(8), 2008.

[72] S. Kilina, S. Tretiak, S. K. Doorn, Z. T. Luo, F. Papadimitrakopoulos, A. Piryatinski, A. Saxena, and A. R. Bishop. Cross-polarized excitons in carbon nanotubes. *Proceedings of the National Academy of Sciences of the United States of America*, 105(19):6797–6802, 2008.

[73] C. D. Spataru, S. Ismail-Beigi, R. B. Capaz, and S. G. Louie. Theory and ab initio calculation of radiative lifetime of excitons in semiconducting carbon nanotubes. *Physical Review Letters*, 95(24), 2005.

[74] H. B. Zhao and S. Mazumdar. Electron-electron interaction effects on the optical excitations of semiconducting single-walled carbon nanotubes. *Physical Review Letters*, 93(15), 2004.

[75] H. Zhao, S. Mazumdar, C. X. Sheng, M. Tong, and Z. V. Vardeny. Photophysics of excitons in quasi-one-dimensional organic semiconductors: Single-walled carbon nanotubes and pi-conjugated polymers. *Physical Review B*, 73(7), 2006.

[76] A. Hagen, M. Steiner, M. B. Raschke, C. Lienau, T. Hertel, H. H. Qian, A. J. Meixner, and A. Hartschuh. Exponential decay lifetimes of excitons in individual single-walled carbon nanotubes. *Physical Review Letters*, 95(19), 2005.

[77] H. Htoon, M. J. O'Connell, S. K. Doorn, and V. I. Klimov. Single carbon nanotubes probed by photoluminescence excitation spectroscopy: The role of phonon-assisted transitions. *Physical Review Letters*, 94(12), 2005.

[78] C. Manzoni, A. Gambetta, E. Menna, M. Meneghetti, G. Lanzani, and G. Cerullo. Intersubband exciton relaxation dynamics in single-walled carbon nanotubes. *Physical Review Letters*, 94(20), 2005.

[79] J. Jiang, R. Saito, A. Gruneis, S. G. Chou, G. G. Samsonidze, A. Jorio, G. Dresselhaus, and M. S. Dresselhaus. Photoexcited electron relaxation processes in single-wall carbon nanotubes. *Physical Review B*, 71(4), 2005.

[80] T. Hertel, V. Perebeinos, J. Crochet, K. Arnold, M. Kappes, and P. Avouris. Intersubband decay of 1-D exciton resonances in carbon nanotubes. *Nano Letters*, 8(1):87–91, 2008.

[81] S. Lebedkin, F. Hennrich, O. Kiowski, and M. M. Kappes. Photophysics of carbon nanotubes in organic polymer-toluene dispersions: Emission and excitation satellites and relaxation pathways. *Physical Review B*, 77(16), 2008.

[82] O. Kiowski, K. Arnold, S. Lebedkin, F. Hennrich, and M. M. Kappes. Direct observation of deep excitonic states in the photoluminescence spectra of single-walled carbon nanotubes. *Physical Review Letters*, 99(23), 2007.

[83] Y. Miyauchi, M. Oba, and S. Maruyama. Cross-polarized optical absorption of single-walled nanotubes by polarized photoluminescence excitation spectroscopy. *Physical Review B*, 74(20), 2006.

[84] N. O. Haugen, A. B. Phillips, T. E. Dykstra, S. Watthage, M. J. Heben, and R. J. Ellingson. Intraexciton transitions observed in high stability doped single-wall carbon nanotube films and solutions. *Journal of Physical Chemistry C*, 118(43):25253–25260, 2014.

[85] D. J. Styers-Barnett, S. P. Ellison, B. P. Mehl, B. C. Westlake, R. L. House, C. Park, K. E. Wise, and J. M. Papanikolas. Exciton dynamics and biexciton formation in single-walled carbon nanotubes studied with femtosecond transient absorption spectroscopy. *Journal of Physical Chemistry C*, 112(12):4507–4516, 2008.

[86] M. Freitag, Y. Martin, J. A. Misewich, R. Martel, and P. H. Avouris. Photoconductivity of single carbon nanotubes. *Nano Letters*, 3(8):1067–1071, 2003.

[87] Y. Kumamoto, M. Yoshida, A. Ishii, A. Yokoyama, T. Shimada, and Y. K. Kato. Spontaneous exciton dissociation in carbon nanotubes. *Physical Review Letters*, 112(11), 2014.

[88] Jacques I. Pankove. *Optical processes in semiconductors*. Dover, New York, 1975.

[89] Y. Z. Ma, L. Valkunas, S. L. Dexheimer, and G. R. Fleming. Ultrafast exciton dynamics in semiconducting single-walled carbon nanotubes. *Molecular Physics*, 104(8):1179–1189, 2006.

[90] Y. F. Xiao, T. Q. Nhan, M. W. B. Wilson, and J. M. Fraser. Saturation of the photoluminescence at few-exciton levels in a single-walled carbon nanotube under ultrafast excitation. *Physical Review Letters*, 104(1), 2010.

[91] Y. Z. Ma, C. D. Spataru, L. Valkunas, S. G. Louie, and G. R. Fleming. Spectroscopy of zigzag single-walled carbon nanotubes: Comparing femtosecond transient absorption spectra with ab initio calculations. *Physical Review B*, 74(8), 2006.

[92] L. B. Huang, H. N. Pedrosa, and T. D. Krauss. Ultrafast ground-state recovery of single-walled carbon nanotubes. *Physical Review Letters*, 93(1), 2004.

[93] J. Lefebvre, D. G. Austing, J. Bond, and P. Finnie. Photoluminescence imaging of suspended single-walled carbon nanotubes. *Nano Letters*, 6(8):1603–1608, 2006.

[94] Z. P. Zhu, J. Crochet, M. S. Arnold, M. C. Hersam, H. Ulbricht, D. Resasco, and T. Hertel. Pump-probe spectroscopy of exciton dynamics in (6,5) carbon nanotubes. *Journal of Physical Chemistry C*, 111(10):3831–3835, 2007.

[95] S. G. Chou, F. Plentz, J. Jiang, R. Saito, D. Nezich, H. B. Ribeiro, A. Jorio, M. A. Pimenta, G. G. Samsonidze, A. P. Santos, M. Zheng, G. B. Onoa, E. D. Semke, G. Dresselhaus, and M. S. Dresselhaus. Phonon-assisted excitonic recombination channels observed in DNA-wrapped carbon nanotubes using photoluminescence spectroscopy. *Physical Review Letters*, 94(12), 2005.

[96] J. S. Lauret, C. Voisin, G. Cassabois, C. Delalande, P. Roussignol, O. Jost, and L. Capes. Ultrafast carrier dynamics in single-wall carbon nanotubes. *Physical Review Letters*, 90(5), 2003.

[97] O. J. Korovyanko, C. X. Sheng, Z. V. Vardeny, A. B. Dalton, and R. H. Baughman. Ultrafast spectroscopy of excitons in single-walled carbon nanotubes. *Physical Review Letters*, 92(1), 2004.

[98] A. Gambetta, C. Manzoni, E. Menna, M. Meneghetti, G. Cerullo, G. Lanzani, S. Tretiak, A. Piryatinski, A. Saxena, R. L. Martin, and A. R. Bishop. Real-time observation of nonlinear coherent phonon dynamics in single-walled carbon nanotubes. *Nature Physics*, 2(8):515–520, 2006.

[99] Sangwan Sim, Jeongmook Choi, Seongchu Lim, Young Hee Lee, and Hyunyong Choi. Ultrafast intra-excitonic quasiparticle annihilation by exciton-exciton scattering in individually isolated single-walled carbon nanotubes. In *CLEO: 2013*, OSA Technical Digest (online), page QM3D.4. Optical Society of America.

[100] J. G. Wang, M. W. Graham, Y. Z. Ma, G. R. Fleming, and R. A. Kaindl. Ultrafast spectroscopy of midinfrared internal exciton transitions in separated single-walled carbon nanotubes. *Physical Review Letters*, 104(17), 2010.

[101] J. H. Hafner, M. J. Bronikowski, B. R. Azamian, P. Nikolaev, A. G. Rinzler, D. T. Colbert, K. A. Smith, and R. E. Smalley. Catalytic growth of single-wall carbon nanotubes from metal particles. *Chemical Physics Letters*, 296(1-2):195–202, 1998.

[102] Unidym, Inc. Single-wall carbon nanotubes, 2008, from http://www.unidym.com/technology/cnt_manufacture.html.

[103] SouthWest NanoTechnologies, Inc. Single-wall carbon nanotubes, 2015, from http://www.swentnano.com/single-wall-cnts.html.

[104] S. M. Bachilo, L. Balzano, J. E. Herrera, F. Pompeo, D. E. Resasco, and R. B. Weisman. Narrow (n,m)-distribution of single-walled carbon nanotubes grown using a solid supported catalyst. *J Am Chem Soc*, 125(37):11186–7, 2003.

[105] B. Kitiyanan, W. E. Alvarez, J. H. Harwell, and D. E. Resasco. Controlled production of single-wall carbon nanotubes by catalytic decomposition of CO on bimetallic Co-Mo catalysts. *Chemical Physics Letters*, 317(3-5):497–503, 2000.

[106] A. G. Rinzler, J. Liu, H. Dai, P. Nikolaev, C. B. Huffman, F. J. Rodriguez-Macias, P. J. Boul, A. H. Lu, D. Heymann, D. T. Colbert, R. S. Lee, J. E. Fischer, A. M. Rao, P. C. Eklund, and R. E. Smalley. Large-scale purification of single-wall carbon nanotubes: process, product, and characterization. *Applied Physics a-Materials Science & Processing*, 67(1):29–37, 1998.

[107] A. Thess, R. Lee, P. Nikolaev, H. J. Dai, P. Petit, J. Robert, C. H. Xu, Y. H. Lee, S. G. Kim, A. G. Rinzler, D. T. Colbert, G. E. Scuseria, D. Tomanek, J. E. Fischer, and R. E. Smalley. Crystalline ropes of metallic carbon nanotubes. *Science*, 273(5274):483–487, 1996.

[108] L. A. Girifalco, M. Hodak, and R. S. Lee. Carbon nanotubes, buckyballs, ropes, and a universal graphitic potential. *Physical Review B*, 62(19):13104–13110, 2000.

[109] S. Reich, M. Dworzak, A. Hoffmann, C. Thomsen, and M. S. Strano. Excited-state carrier lifetime in single-walled carbon nanotubes. *Physical Review B*, 71(3), 2005.

[110] J. J. Crochet, J. D. Sau, J. G. Duque, S. K. Doorn, and M. L. Cohen. Electrodynamic and excitonic intertube interactions in semiconducting carbon nanotube aggregates. *ACS Nano*, 5(4):2611–8, 2011.

[111] T. Hertel, R. Fasel, and G. Moos. Charge-carrier dynamics in single-wall carbon nanotube bundles: a time-domain study. *Applied Physics a-Materials Science & Processing*, 75(4):449–465, 2002.

[112] A. Hagen, G. Moos, V. Talalaev, and T. Hertel. Electronic structure and dynamics of optically excited single-wall carbon nanotubes. *Applied Physics a-Materials Science & Processing*, 78(8):1137–1145, 2004.

[113] O. Obaiza. 5 easy recipes for gooey homemade ooze, 2013, from http://science.wonderhowto.com/how-to/make-slime-without-borax-5-easy-recipes-for-gooey-homemade-ooze-0147194/.

[114] M. S. Arnold, S. Lan, S. C. Cruz, J. E. Sharping, S. I. Stupp, P. Kumar, and M. C. Hersam. Optical absorption and transient photobleaching in solutions of surfactant encapsulated and DNA wrapped single-walled carbon nanotubes. *Quantum Sensing and Nanophotonic Devices*, 5359:376–386, 2004.

[115] C. Fantini, A. Jorio, A. P. Santos, V. S. T. Peressinotto, and M. A. Pimenta. Characterization of DNA-wrapped carbon nanotubes by resonance raman and optical absorption spectroscopies. *Chemical Physics Letters*, 439(1-3):138–142, 2007.

[116] A. Nish, J. Y. Hwang, J. Doig, and R. J. Nicholas. Highly selective dispersion of singlewalled carbon nanotubes using aromatic polymers. *Nature Nanotechnology*, 2(10):640–646, 2007.

[117] A. Nish, J. Y. Hwang, J. Doig, and R. J. Nicholas. Direct spectroscopic evidence of energy transfer from photo-excited semiconducting polymers to single-walled carbon nanotubes. *Nanotechnology*, 19(9), 2008.

[118] J. Y. Hwang, A. Nish, J. Doig, S. Douven, C. W. Chen, L. C. Chen, and R. J. Nicholas. Polymer structure and solvent effects on the selective dispersion of single-walled carbon nanotubes. *Journal of the American Chemical Society*, 130(11):3543–3553, 2008.

[119] Christoph Brabec, Ullrich Scherf, Vladimir Dyakonov, Dechan Angmo, and Library Wiley Online. *Organic photovoltaics materials, device physics, and manufacturing technologies*. Wiley-VCH, Weinheim, Germany, 2014.

[120] Martin Pope and Charles E. Swenberg. *Electronic processes in organic crystals and polymers*. Monographs on the physics and chemistry of materials; #56. Oxford University Press, New York, 1999.

[121] E. Kymakis and G. A. J. Amaratunga. Single-wall carbon nanotube/conjugated polymer photovoltaic devices. *Applied Physics Letters*, 80(1):112–114, 2002.

[122] D. E. Markov, E. Amsterdam, P. W. M. Blom, A. B. Sieval, and J. C. Hummelen. Accurate measurement of the exciton diffusion length in a conjugated polymer using a heterostructure with a side-chain cross-linked fullerene layer. *Journal of Physical Chemistry A*, 109(24):5266–5274, 2005.

[123] O. V. Mikhnenko, H. Azimi, M. Scharber, M. Morana, P. W. M. Blom, and M. A. Loi. Exciton diffusion length in narrow bandgap polymers. *Energy & Environmental Science*, 5(5):6960–6965, 2012.

[124] K. W. Lee, S. P. Lee, H. Choi, K. H. Mo, J. W. Jang, H. Kweon, and C. E. Lee. Enhanced electroluminescence in polymer-nanotube composites. *Applied Physics Letters*, 91(2), 2007.

[125] Brian J. Landi, Ryne P. Raffaelle, Stephanie L. Castro, and Sheila G. Bailey. Single-wall carbon nanotube-polymer solar cells. *Progress in Photovoltaics: Research and Applications*, 13(2):165–172, 2005.

[126] S. D. Stranks, C. Weisspfennig, P. Parkinson, M. B. Johnston, L. M. Herz, and R. J. Nicholas. Ultrafast charge separation at a polymer-single-walled carbon nanotube molecular junction. *Nano Letters*, 11(1):66–72, 2011.

[127] M. C. Wu, Y. Y. Lin, S. Chen, H. C. Liao, Y. J. Wu, C. W. Chen, Y. F. Chen, and W. F. Su. Enhancing light absorption and carrier transport of P3HT by doping multi-wall carbon nanotubes. *Chemical Physics Letters*, 468(1-3):64–68, 2009.

[128] A. J. Siitonen, D. A. Tsyboulski, S. M. Bachilo, and R. B. Weisman. Surfactant-dependent exciton mobility in single-walled carbon nanotubes studied by single-molecule reactions. *Nano Letters*, 10(5):1595–1599, 2010.

[129] L. Luer, S. Hoseinkhani, D. Polli, J. Crochet, T. Hertel, and G. Lanzani. Size and mobility of excitons in (6,5) carbon nanotubes. *Nature Physics*, 5(1):54–58, 2009.

[130] L. Cognet, D. A. Tsyboulski, J. D. R. Rocha, C. D. Doyle, J. M. Tour, and R. B. Weisman. Stepwise quenching of exciton fluorescence in carbon nanotubes by single-molecule reactions. *Science*, 316(5830):1465–1468, 2007.

[131] A. J. Siitonen, D. A. Tsyboulski, S. M. Bachilo, and R. B. Weisman. Dependence of exciton mobility on structure in single-walled carbon nanotubes. *Journal of Physical Chemistry Letters*, 1(14):2189–2192, 2010.

[132] A. Ishii, M. Yoshida, and Y. K. Kato. Exciton diffusion, end quenching, and exciton-exciton annihilation in individual air-suspended carbon nanotubes. *Physical Review B*, 91(12), 2015.

[133] Christoph J. Brabec, Gerald Zerza, Giulio Cerullo, Sandro De Silvestri, Silvia Luzzati, Jan C. Hummelen, and Serdar Sariciftci. Tracing photoinduced electron transfer process in conjugated polymer/fullerene bulk heterojunctions in real time. *Chemical Physics Letters*, 340(3-4):232–236, 2001.

[134] J. Chappell, D. G. Lidzey, P. C. Jukes, A. M. Higgins, R. L. Thompson, S. O'Connor, I. Grizzi, R. Fletcher, J. O'Brien, M. Geoghegan, and R. A. Jones. Correlating structure with fluorescence emission in phase-separated conjugated-polymer blends. *Nat Mater*, 2(9):616–21, 2003.

[135] M. Jones, C. Engtrakul, W. K. Metzger, R. J. Ellingson, A. J. Nozik, M. J. Heben, and G. Rumbles. Analysis of photoluminescence from solubilized single-walled carbon nanotubes. *Physical Review B*, 71(11), 2005.

[136] A. Hartschuh, H. N. Pedrosa, L. Novotny, and T. D. Krauss. Simultaneous fluorescence and raman scattering from single carbon nanotubes. *Science*, 301(5638):1354–1356, 2003.

[137] H. Htoon, M. J. O'Connell, P. J. Cox, S. K. Doorn, and V. I. Klimov. Low temperature emission spectra of individual single-walled carbon nanotubes: Multiplicity of subspecies within single-species nanotube ensembles. *Physical Review Letters*, 93(2), 2004.

[138] M. S. Arnold, J. E. Sharping, S. I. Stupp, P. Kumar, and M. C. Hersam. Band gap photobleaching in isolated single-walled carbon nanotubes. *Nano Letters*, 3(11):1549–1554, 2003.

[139] T. Koyama, K. Asaka, N. Hikosaka, H. Kishida, Y. Saito, and A. Nakamura. Ultrafast exciton energy transfer in bundles of single-walled carbon nanotubes. *Journal of Physical Chemistry Letters*, 2(3):127–132, 2011.

[140] J. Lefebvre and P. Finnie. Photoluminescence and Förster resonance energy transfer in elemental bundles of single-walled carbon nanotubes. *Journal of Physical Chemistry C*, 113(18):7536–7540, 2009.

[141] L. Luer, J. Crochet, T. Hertel, G. Cerullo, and G. Lanzani. Ultrafast excitation energy transfer in small semiconducting carbon nanotube aggregates. *Acs Nano*, 4(7):4265–4273, 2010.

[142] H. H. Qian, C. Georgi, N. Anderson, A. A. Green, M. C. Hersam, L. Novotny, and A. Hartschuh. Exciton energy transfer in pairs of single-walled carbon nanotubes. *Nano Letters*, 8(5):1363–1367, 2008.

[143] A. Jorio, R. Saito, J. H. Hafner, C. M. Lieber, M. Hunter, T. McClure, G. Dresselhaus, and M. S. Dresselhaus. Structural (n, m) determination of isolated single-wall carbon nanotubes by resonant raman scattering. *Physical Review Letters*, 86(6):1118–1121, 2001.

[144] J. Maultzsch, H. Telg, S. Reich, and C. Thomsen. Radial breathing mode of single-walled carbon nanotubes: Optical transition energies and chiral-index assignment. *Physical Review B*, 72(20), 2005.

[145] Feng Yang, Xiao Wang, Daqi Zhang, Juan Yang, LuoDa, Ziwei Xu, Jiake Wei, Jian-Qiang Wang, Zhi Xu, Fei Peng, Xuemei Li, Ruoming Li, Yilun Li, Meihui Li, Xuedong Bai, Feng Ding, and Yan Li. Chirality-specific growth of single-walled carbon nanotubes on solid alloy catalysts. *Nature*, 510(7506):522–524, 2014.

[146] Juan Ramon Sanchez-Valencia, Thomas Dienel, Oliver Groning, Ivan Shorubalko, Andreas Mueller, Martin Jansen, Konstantin Amsharov, Pascal Ruffieux, and Roman Fasel. Controlled synthesis of single-chirality carbon nanotubes. *Nature*, 512(7512):61–64, 2014.

[147] R. Saito, A. Jorio, A. G. Souza, G. Dresselhaus, M. S. Dresselhaus, and M. A. Pimenta. Probing phonon dispersion relations of graphite by double resonance raman scattering. *Physical Review Letters*, 88(2), 2002.

[148] M. Lazzeri, S. Piscanec, F. Mauri, A. C. Ferrari, and J. Robertson. Phonon linewidths and electron-phonon coupling in graphite and nanotubes. *Physical Review B*, 73(15), 2006.

[149] S. Piscanec, M. Lazzeri, J. Robertson, A. C. Ferrari, and F. Mauri. Optical phonons in carbon nanotubes: Kohn anomalies, Peierls distortions, and dynamic effects. *Physical Review B*, 75(3), 2007.

[150] M. E. Itkis, D. E. Perea, S. Niyogi, S. M. Rickard, M. A. Hamon, B. Zhao, and R. C. Haddon. Purity evaluation of as-prepared single-walled carbon nanotube soot by use of solution-phase near-IR spectroscopy. *Nano Letters*, 3(3):309–314, 2003.

[151] A. V. Naumov, S. Ghosh, D. A. Tsyboulski, S. M. Bachilo, and R. B. Weisman. Analyzing absorption backgrounds in single-walled carbon nanotube spectra. *ACS Nano*, 5(3):1639–1648, 2011.

[152] A. E. Siegman. *Lasers*. University Science Books, Mill Valley, Calif., 1986.

[153] R. B. Capaz, C. D. Spataru, S. Ismail-Beigi, and S. G. Louie. Diameter and chirality dependence of exciton properties in carbon nanotubes. *Physical Review B*, 74(12), 2006.

[154] R. B. Capaz, C. D. Spataru, S. Ismail-Beigi, and S. G. Louie. Excitons in carbon nanotubes: Diameter and chirality trends. *Physica Status Solidi B-Basic Solid State Physics*, 244(11):4016–4020, 2007.

[155] L. Luer, J. Crochet, S. Hoseinkhani, T. Hertel, G. Cerullo, and G. Lanzani. Ultrafast exciton and charge transfer in small aggregates of carbon nanotubes. *Ultrafast Phenomena in Semiconductors and Nanostructure Materials Xv*, 7937, 2011.

[156] H. Ajiki and T. Ando. Aharonov-Bohm effect in carbon nanotubes. *Physica B*, 201:349–352, 1994.

[157] R. L. Fork. Optical frequency filter for ultrashort pulses. *Optics Letters*, 11(10):629–631, 1986.

[158] S. Berciaud, L. Cognet, and B. Lounis. Luminescence decay and the absorption cross section of individual single-walled carbon nanotubes. *Phys Rev Lett*, 101(7):077402, 2008.

[159] G. R. Fleming, M. W. Graham, Y. Z. Ma, A. A. Green, and M. C. Hersam. Pure optical dephasing dynamics in semiconducting single-walled carbon nanotubes. *Journal of Chemical Physics*, 134(3), 2011.

[160] G. R. Fleming, M. W. Graham, Y. Z. Ma, A. A. Green, and M. C. Hersam. Exciton annihilation and dephasing dynamics in semiconducting single-walled carbon nanotubes. *Ultrafast Phenomena in Semiconductors and Nanostructure Materials Xiv*, 7600, 2010.

[161] T. Gokus, A. Hartschuh, H. Harutyunyan, M. Allegrini, F. Hennrich, M. Kappes, A. A. Green, M. C. Hersam, P. T. Araujo, and A. Jorio. Exciton decay dynamics in individual carbon nanotubes at room temperature. *Applied Physics Letters*, 92(15), 2008.

[162] L. Valkunas, M. W. Graham, J. Chmeliov, Y. Z. Ma, H. Shinohara, A. A. Green, M. C. Hersam, and G. R. Fleming. Exciton dynamics in semiconducting carbon nanotubes. *Journal of Physical Chemistry B*, 115(18):5201–5211, 2011.

[163] L. D. Ziegler, J. R. Schneck, A. G. Walsh, A. A. Green, M. C. Hersam, and A. K. Swan. Electron correlation effects on the femtosecond dephasing dynamics of E(22) excitons in (6,5) carbon nanotubes. *Journal of Physical Chemistry A*, 115(16):3917–3923, 2011.

[164] A. Jorio, A. P. Santos, H. B. Ribeiro, C. Fantini, M. Souza, J. P. M. Vieira, C. A. Furtado, J. Jiang, R. Saito, L. Balzano, D. E. Resasco, and M. A. Pimenta. Quantifying carbon-nanotube species with resonance raman scattering. *Physical Review B*, 72(7), 2005.

[165] Graham R. Fleming. *Chemical applications of ultrafast spectroscopy*. International series of monographs on chemistry.13. Oxford University Press ; Clarendon Press, New York : Oxford [Oxfordshire], 1986.

[166] H. S. Tan, I. R. Piletic, and M. D. Fayer. Polarization selective spectroscopy experiments: methodology and pitfalls. *Journal of the Optical Society of America B-Optical Physics*, 22(9):2009–2017, 2005.

[167] K. C. Chuang, A. Nish, J. Y. Hwang, G. W. Evans, and R. J. Nicholas. Experimental study of coulomb corrections and single-particle energies for single-walled carbon nanotubes using cross-polarized photoluminescence. *Physical Review B*, 78(8), 2008.

[168] M. F. Islam, D. E. Milkie, C. L. Kane, A. G. Yodh, and J. M. Kikkawa. Direct measurement of the polarized optical absorption cross section of single-wall carbon nanotubes. *Physical Review Letters*, 93(3), 2004.

[169] D. J. Bindl, M. Y. Wu, F. C. Prehn, and M. S. Arnold. Efficiently harvesting excitons from electronic type-controlled semiconducting carbon nanotube films. *Nano Lett*, 11(2):455–60, 2011.

[170] N. T. Harrison, G. R. Hayes, R. T. Phillips, and R. H. Friend. Singlet intrachain exciton generation and decay in poly(p-phenylenevinylene). *Physical Review Letters*, 77(9):1881–1884, 1996.

[171] A. Nish and R. J. Nicholas. Temperature induced restoration of fluorescence from oxidised single-walled carbon nanotubes in aqueous sodium dodecylsulfate solution. *Physical Chemistry Chemical Physics*, 8(30):3547–3551, 2006.

[172] Matthew J. Shea, Randy D. Mehlenbacher, Martin T. Zanni, and Michael S. Arnold. Experimental measurement of the binding configuration and coverage of chirality-sorting polyfluorenes on carbon nanotubes. *The Journal of Physical Chemistry Letters*, pages 3742–3749, 2014.

[173] Y. Z. Ma, L. Valkunas, S. L. Dexheimer, S. M. Bachilo, and G. R. Fleming. Femtosecond spectroscopy of optical excitations in single-walled carbon nanotubes: Evidence for exciton-exciton annihilation. *Physical Review Letters*, 94(15), 2005.

[174] Y. Murakami and J. Kono. Nonlinear photoluminescence excitation spectroscopy of carbon nanotubes: Exploring the upper density limit of one-dimensional excitons. *Physical Review Letters*, 102(3), 2009.

[175] Javier Grillo-Marxuach and Les McClaine. The Middleman, 2008.

[176] T. G. Pedersen, K. Pedersen, H. D. Cornean, and P. Duclos. Stability and signatures of biexcitons in carbon nanotubes. *Nano Letters*, 5(2):291–294, 2005.

[177] S. C. Rand. Lectures on light: Nonlinear and quantum optics using the density matrix, 2nd edition. *Lectures on Light: Nonlinear and Quantum Optics Using the Density Matrix, 2nd Edition*, pages 1–380, 2016.

[178] F. Jahnke. (personal communication), February 5, 2016.

[179] F. Jahnke. (personal communication), February 1, 2016.

[180] M. Florian. (personal communication), June 10, 2016.

[181] M. Florian. (personal communication), July 24, 2016.

[182] M. Florian. (personal communication), Sept 16, 2016.

[183] R. H. Friend, R. W. Gymer, A. B. Holmes, J. H. Burroughes, R. N. Marks, C. Taliani, D. D. C. Bradley, D. A. Dos Santos, J. L. Bredas, M. Logdlund, and W. R. Salaneck. Electroluminescence in conjugated polymers. *Nature*, 397(6715):121–128, 1999.

[184] ScienceDirect. Organic electronics. *Organic electronics*, page 1 online resource, 2000.

[185] Robert Burns. *The complete poetical works*. Poems. W. P. Nimmo, Edinburgh, 1866.

[186] H. Kataura, Y. Kumazawa, Y. Maniwa, I. Umezu, S. Suzuki, Y. Ohtsuka, and Y. Achiba. Optical properties of single-wall carbon nanotubes. *Synthetic Metals*, 103(1-3):2555–2558, 1999.

[187] A. Jorio, C. Fantini, M. A. Pimenta, R. B. Capaz, G. G. Samsonidze, G. Dresselhaus, M. S. Dresselhaus, J. Jiang, N. Kobayashi, A. Gruneis, and R. Saito. Resonance Raman spectroscopy (n,m)-dependent effects in small-diameter single-wall carbon nanotubes. *Physical Review B*, 71(7), 2005.

[188] E. B. Barros, A. Jorio, G. G. Samsonidze, R. B. Capaz, A. G. Souza, J. Mendes, G. Dresselhaus, and M. S. Dresselhaus. Review on the symmetry-related properties of carbon nanotubes. *Physics Reports-Review Section of Physics Letters*, 431(6):261–302, 2006.

[189] C. Fantini, A. Jorio, M. Souza, M. S. Strano, M. S. Dresselhaus, and M. A. Pimenta. Optical transition energies for carbon nanotubes from resonant raman spectroscopy: environment and temperature effects. *Phys Rev Lett*, 93(14):147406, 2004.

[190] F. Wang, G. Dukovic, L. E. Brus, and T. F. Heinz. Time-resolved fluorescence of carbon nanotubes and its implication for radiative lifetimes. *Physical Review Letters*, 92(17), 2004.

[191] J. Kono, G. N. Ostojic, S. Zaric, M. S. Strano, V. C. Moore, R. H. Hauge, and R. E. Smalley. Interband recombination dynamics in resonantly excited single-walled carbon nanotubes. *Physical Review Letters*, 92(11), 2004.

[192] S. G. Chou, M. F. DeCamp, J. Jiang, G. G. Samsonidze, E. B. Barros, F. Plentz, A. Jorio, M. Zheng, G. B. Onoa, E. D. Semke, A. Tokmakoff, R. Saito, G. Dresselhaus, and M. S. Dresselhaus. Phonon-assisted exciton relaxation dynamics for a (6,5)-enriched DNA-wrapped single-walled carbon nanotube sample. *Physical Review B*, 72(19), 2005.